



**CERAMIC MATRIX COMPOSITE CHARACTERIZATION UNDER A
COMBUSTION AND LOADING ENVIRONMENT**

THESIS

Andrew R. Nye, Captain, USAF

AFIT/GMS/ENY/09-M01

**DEPARTMENT OF THE AIR FORCE
AIR UNIVERSITY
*AIR FORCE INSTITUTE OF TECHNOLOGY***

Wright-Patterson Air Force Base, Ohio

APPROVED FOR PUBLIC RELEASE; DISTRIBUTION UNLIMITED

The views expressed in this thesis are those of the author and do not reflect the official policy or position of the United States Air Force, Department of Defense, or the United States Government.

AFIT/GMS/ENY/09-M01

CERAMIC MATRIX COMPOSITE CHARACTERIZATION UNDER A
COMBUSTION AND LOADING ENVIRONMENT

THESIS

Presented to the Faculty

Department of Aeronautics and Astronautics

Graduate School of Engineering and Management

Air Force Institute of Technology

Air University

Air Education and Training Command

In Partial Fulfillment of the Requirements for the

Degree of Master of Science (Materials Science)

Andrew R. Nye, BS

Captain, USAF

March 2009

APPROVED FOR PUBLIC RELEASE; DISTRIBUTION UNLIMITED.

CERAMIC MATRIX COMPOSITE CHARACTERIZATION UNDER A
COMBUSTION AND LOADING ENVIRONMENT

Andrew R. Nye, BS
Captain, USAF

Approved:

//signed//

4 March 2009

Dr. Shankar Mall (Chairman)

Date

//signed//

4 March 2009

Dr. Vinod Jain (Member)

Date

//signed//

4 March 2009

Dr. Som Soni (Member)

Date

Abstract

Lightweight materials that can withstand high temperatures and corrosive environments are constantly sought after in the aerospace industry, typically for Gas Turbine Engine (GTE) application. These materials need to retain their strength throughout the long service period they would see in the combustor and turbine components of a GTE. One material that is ideal for these types of applications is an oxide/oxide Ceramic Matrix Composite (CMC).

The fatigue behavior of the oxide/oxide CMC Nextel™ 720/Alumina (N720/A) was investigated in a unique high temperature environment. N720/A consisted of an 8-harness satin weave of Nextel™ aluminum oxide/silicon oxide fibers bound together with an alumina matrix. Past studies have encompassed fatigue and creep-rupture resistant at elevated temperatures in laboratory air or other non-combustion environment, such as steam or inert gas. The specimens used in this research were exposed to a combustion environment, which is a much more volatile and realistic environment for what this material would see in a GTE application.

The combustion environment was created using a High-Velocity Oxygen Fuel (HVOF) Gun. The flame directly impinged the CMC specimen on one side as it underwent fatigue testing, heating up that surface to approximately 1200°C. Results show that the effects of a combustion environment on the materials fatigue behavior are negligible.

Acknowledgments

I would like to express my sincere appreciation to my faculty advisor, Dr. Shankar Mall, for his guidance and support throughout the course of this thesis effort. The insight and experience was certainly appreciated. I would also like to thank John Hixenbaugh for his guidance and procurement of the materials needed to run the HVOF rig. Most importantly, I wish to thank my wife for her love and support through my thesis work.

Andrew R. Nye

Table of Contents

	Page
Abstract	iv
Acknowledgments.....	v
List of Figures	viii
List of Tables	xiii
 I. Introduction.....	 1
1.1 Propulsion Evolution	1
1.2 Ceramic Matrix Composites.....	3
1.2.1 Oxidation	4
1.2.2 Nextel™ 720/Alumina (N720/A)	5
1.3 Fatigue Loading.....	6
1.4 Combustion Environment.....	8
1.5 Objectives	9
 II. Literature Review	 10
2.1 Fatigue Testing	10
2.2 Notch Sensitivity Testing	11
2.3 Combustion Environment Testing.....	12
2.4 N720/A Behavior Overview	14
 III. Test Equipment and Experimental Procedure	 15
3.1 Material Description	15
3.1.1 Specimen Geometry.....	17
3.1.2 Thermal Emissivity.....	18
3.2 Equipment.....	20
3.2.1 Material Test Stand.....	20
3.2.2 High-Velocity Oxygen-Fuel Flame System	23
3.2.3 Safety Shutdown System	27
3.2.4 Forward-Looking Infrared System	28
3.2.5 Specimen Imaging Equipment.....	31
3.3 Test Procedure	34
3.3.1 Specimen Inspection and Processing.....	34
3.3.2 Thermal Emissivity Analysis.....	36
3.3.3 Equipment Start-up and Specimen Loading	37
3.3.4 HVOF and Temperature Measurement Start-up.....	38

	Page
3.3.5 Fatigue Tests	40
3.3.6 Ultimate and Residual Strength Tests.....	42
3.4 Test Matrix	43
IV. Results and Analysis	44
4.1 Thermal Emissivity Data	44
4.2 Specimen Temperatures in Testing	45
4.3 Thermal Strain during Testing.....	47
4.4 Monotonic Tensile Test	49
4.5 Fatigue Tests.....	50
4.5.1 Fatigue Strain Hysteresis	52
4.5.2 Secant Modulus	58
4.6 Residual Strength Test.....	60
4.7 Microstructural Analysis	61
4.7.1 Pretest and Posttest Specimen Comparison.....	62
4.7.2 Monotonic Testing Fracture Surfaces.....	64
4.7.3 Scanning Electron Microscope Efforts	66
4.8. Results Summary.....	84
V. Conclusions and Recommendations.....	85
Appendix.....	87
Bibliography	102
Vita.....	105

List of Figures

Figure	Page
1. Temperature Limits of Polymers, Metals, and Ceramic	2
2. Damage Tolerance Mechanism of CMC's	4
3. N720/A Fatigue Behavior at 1200°C	7
4. Satin Weave	15
5. CMC Manufacturing Process.....	16
6. Specimen Dimensions.....	17
7. Photo of a Prepared Specimen	18
8. Premature Failure of Earlier Specimen Geometry	18
9. Representative Emissivities of Materials	19
10. MTS Test Apparatus	21
11. MTS Grip Cooling Scheme	22
12. HVOF Thermal Spray Process.....	23
13. DJ9A HVOF Spray Gun	24
14. DJF Gas Flowmeter Unit	25
15. Whisper Room	26
16. LabVIEW Control Program Block Diagram	28
17. FLIR ThermaCAM P640 Camera.....	29
18. FLIR ThermaCAM PM695 Camera	30
19. FLIR Measurement during Testing.....	31
20. Zeiss Discovery V12 Optical Microscope	32

	Page
21. Quanta 200 SEM.....	33
22. Specimens Prepared for SEM	34
23. Emissivity Investigation Setup	36
24. Control System Display (Pretest).....	39
25. Cyclic Loading with PVC Compensation.....	41
26. Fatigue Test Program.....	42
27. Front and Rear Temperature Profiles.....	47
28. Combustion Environment Tensile Strength.....	49
29. Fatigue Stress versus Cycles	51
30. Normalized Fatigue Stress versus Cycles Comparison with Eber Data	52
31. 60 MPa Hysteresis Data.....	53
32. 94.5 MPa Hysteresis Data.....	53
33. 108 MPa Hysteresis Data.....	54
34. 121.5 MPa Hysteresis Data.....	54
35. 142 MPa Hysteresis Data.....	55
36. 150 MPa Hysteresis Data.....	55
37. Maximum Strain Increase vs. Cycles.....	56
38. Delta Strain vs. Cycles	57
39. Secant Modulus vs. Cycle.....	59
40. Normalized Secant Modulus vs. Cycle.....	59
41. Residual Strength Stress-Strain Curves	60
42. 108 MPa Specimen Pre and Post Test (Flame Side).....	62

	Page
43. 121.5 MPa Specimen Pre and Post Test (Flame Side).....	63
44. 142 MPa Specimen Pre and Post Test (Flame Side).....	63
45. Tensile Strength Specimen Fracture Surface	65
46. 142 MPa Specimen Residual Strength Fracture	66
47. Pristine Specimen Overall Interior Structure	67
48. Pristine Specimen Matrix Crack	68
49. Pristine Specimen Fiber-Matrix Interface.....	68
50. Internal Structure of Fracture Specimen	70
51. Internal Surface (Flame Side)	71
52. Internal Surface (Middle).....	71
53. Internal Surface (Rear).....	72
54. 142 MPa Fracture Surface (Rear Looking Towards Flame Side).....	73
55. 142 MPa Fracture Surface (Flame Side Looking Towards Rear).....	73
56. Flame Side 0° Fiber Bundle (Flame Side Edge at Top)	74
57. Rear Side 0° Fiber Bundle (Rear Edge at Bottom)	75
58. Front Right Edge Fracture Surface (Flame Side at Top)	76
59. Front Right Edge Box 1 90° Fiber Bundle	76
60. Front Right Edge Box 2 90° Fiber Bundle	77
61. Front Right Edge Box 2 Fibers with Matrix	77
62. Front Left Edge Fracture Surface (Flame Side at Top)	78
63. Front Left Edge 90° Fiber Bundles (Flame Side at Top).....	78
64. Front Left Edge Box 1 Fiber-Matrix Interface	79

	Page
65. Front Left Edge Box 2 Fiber-Matrix Interface	79
66. Rear Right Edge Fracture Surface (Flame Side Towards Top)	80
67. Rear Right Edge 90° Fiber Bundle	81
68. Rear Left Edge Fracture Surface (Flame Side Towards Top)	81
69. Rear Left Edge 90° Fiber Bundle	82
70. Flame Side Surface 90° Individual Fiber.....	83
71. Rear Surface 90° Individual Fiber	83
72. Stress Strain of Unexposed and Combustion Exposed CMC	87
73. Pristine Surface, 50x	87
74. Pristine Surface, 120x	88
75. Pristine Surface Fibers, 1001x	88
76. Pristine Surface Fibers, 1000x	89
77. 142 MPa Fracture Side View, 52x.....	89
78. 142 MPa Side Fracture Front Cracking, 200x	90
79. 142 MPa Side Fracture Front Cracking, 1509x	90
80. 142 MPa Side Fracture Back Fiber-Matrix, 504x.....	91
81. 142 MPa Side Fracture Back Fiber, 3000x	91
82. 142 MPa Fracture Surface, Overhead View, 32x	92
83. 142 MPa Fracture Surface, Overhead Right View, 59x	92
84. 142 MPa Fracture Surface, Front Right 90° Fiber Pullout, 1000x	93
85. 142 MPa Fracture Surface, Front Right Fiber-Matrix, 500x	93
86. 142 MPa Fracture Surface, Front Right Fiber-Matrix, 2000x	94

	Page
87. 142 MPa Fracture Surface, Front Center, 120x	94
88. 142 MPa Fracture Surface, Front Center, 500x	95
89. 142 MPa Fracture Surface, Middle Center, 490x	95
90. 142 MPa Fracture Surface, Middle Center Fiber Pullout, 500x	96
91. 142 MPa Fracture Surface, Middle Center Fiber Pullout, 2000x	96
92. 142 MPa Fracture Surface, Rear Left, 120x	97
93. 142 MPa Fracture Surface, Rear Left Fiber Pullout, 500x	97
94. 142 MPa Fracture Surface, Rear Left Fiber Pullout, 1007x	98
95. 142 MPa Fracture Surface, Rear Right Aft Looking Forward, 51x.....	98
96. 142 MPa Fracture Surface, Middle Left Fiber Pullout, 500x	99
97. 142 MPa Fracture Surface, Rear Left Aft Looking Forward, 60x.....	99
98. 142 MPa Fracture Surface, Rear Left Fiber Pullout, 120x	100
99. 142 MPa Fracture Surface, Rear Left Fiber Pullout, 500x	100
100. 142 MPa Fracture Surface, Rear Left Fiber Pullout, 1000x	101

List of Tables

Table	Page
1. Nextel™ 720 Fiber Properties	5
2. Alumina Properties	6
3. Panel #4569-2 Properties	17
4. Thermocouple Locations and Safety Limits	27
5. Pressure and Flow Parameters	39
6. Test Matrix Under the Combustion Environment	43
7. Emissivity Values versus Temperature.....	44
8. Flame Side Area Temperature Data.....	46
9. Rear Area Temperature Data	46
10. Spot Temperature Data	46
11. Thermal Strain and Expansion of N720/A in a Combustion Environment	48
12. Tensile Strength Data.....	50
13. Fatigue Test Summary	51
14. Residual Strength Testing Results	61

CERAMIC MATRIX COMPOSITE CHARACTERIZATION UNDER A COMBUSTION AND LOADING ENVIRONMENT

I. Introduction

Since the inception of powered flight, there has been great focus on advancing the aircraft system; making it faster; fly higher; increasing its range, fuel economy, safety, and reliability [10:xv]. A critical part of the aircraft is the propulsion system, which is typically a gas turbine engine (GTE) in current military and commercial applications. Demands are continually being made on this system, specifically for greater thrust and fuel efficiency, which tie in directly to the aforementioned aircraft system advancements.

1.1 Propulsion Evolution

The simplest way to increase thrust and efficiency is by increasing combustion temperatures, thereby increasing the turbine inlet temperature. Because of this fact, turbine inlet temperatures have risen from a max of 850°C in 1945 to a max of 1750°C today [11:107]. However, increasing these temperatures has a detrimental effect on the combustor and turbine components. Increased combustion temperatures require increasing cooling to prevent the components from melting or exhibiting high-temperature plastic creep [11:281, 372]. Cooling is accomplished with air pulled off of the compressor stages, which ultimately reduces the efficiency of the compressor and reduces the amount of air available for combustion.

Modern GTE combustor and turbine materials consist of Nickel Superalloys. Modern single crystal superalloys used for turbine blades have a max operating temperature of 1100°C, which is well below maximum turbine inlet temperatures [11:288]. To be able to withstand this extreme temperature environment, turbine and combustor components have complex cooling schemes and ceramic-based thermal barrier coatings to keep the base metal temperatures down.

A newer turbine engine material option is ceramic matrix composites (CMC's). These materials can withstand much higher temperatures while still retaining their strength. This is shown in Figure 1, which gives serviceable temperature limits of polymers, metals, and ceramics.

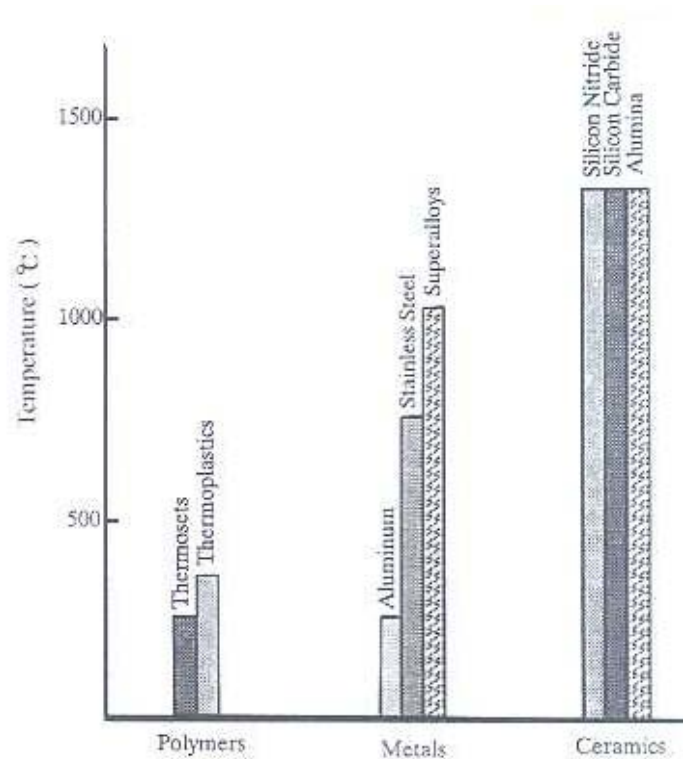


Figure 1. Temperature Limits of Polymers, Metals, and Ceramic [3:5]

1.2 Ceramic Matrix Composites

Advancements in processing technologies have allowed us to manufacture high quality ceramic materials, consisting of pure oxides, nitrides, or carbides of silicon, aluminum, titanium, and zirconium. Ceramics are desirable because of their high strength; high temperature, chemical, and wear resistance; and low density. However, ceramics in their monolithic form react poorly under tensile loading, being very brittle in mechanical or thermal loading, and having a low fracture toughness [3:2-4].

Ceramic Matrix Composites are able to utilize the advantages and greatly reduce the undesirable characteristics of monolithic ceramic materials. This is accomplished by reinforcing a ceramic matrix with ceramic fibers, whiskers, or particles. The reinforcements create an energy dissipation path for cracking in the ceramic matrix, increasing the ceramic composites toughness and giving the material a damage-tolerant behavior. This energy dissipation behavior is exhibited in the form of debonding at the fiber/matrix interface, or in fiber pullout when a crack is formed, which hinders further growth of the crack [3:6-7]. Increased fracture toughness subsequently gives the ceramic composite increased capability under a tensile load.

There are three methods utilized to create this energy dissipation mechanism. The first method, commonly used on Silicon Carbide (SiC) and Carbon CMC's, is to coat the fibers to create a weak interface between the matrix and fibers [24]. Examples of matrix coatings are Monazite (LaPO_4), Scheelite (CaWO_4), and Hibonite ($\text{CaAl}_{12}\text{O}_{19}$) [12]. The second method is to use a porous matrix material. This requires that the fibers and matrix be phase compatible because they will be contacting. The third method is to use a fiber

coating that will oxidize after the CMC manufacturing process, leaving a small interface gap between the fibers and matrix [24]. Figure 2 shows CMC energy dissipation behavior and the methods used.

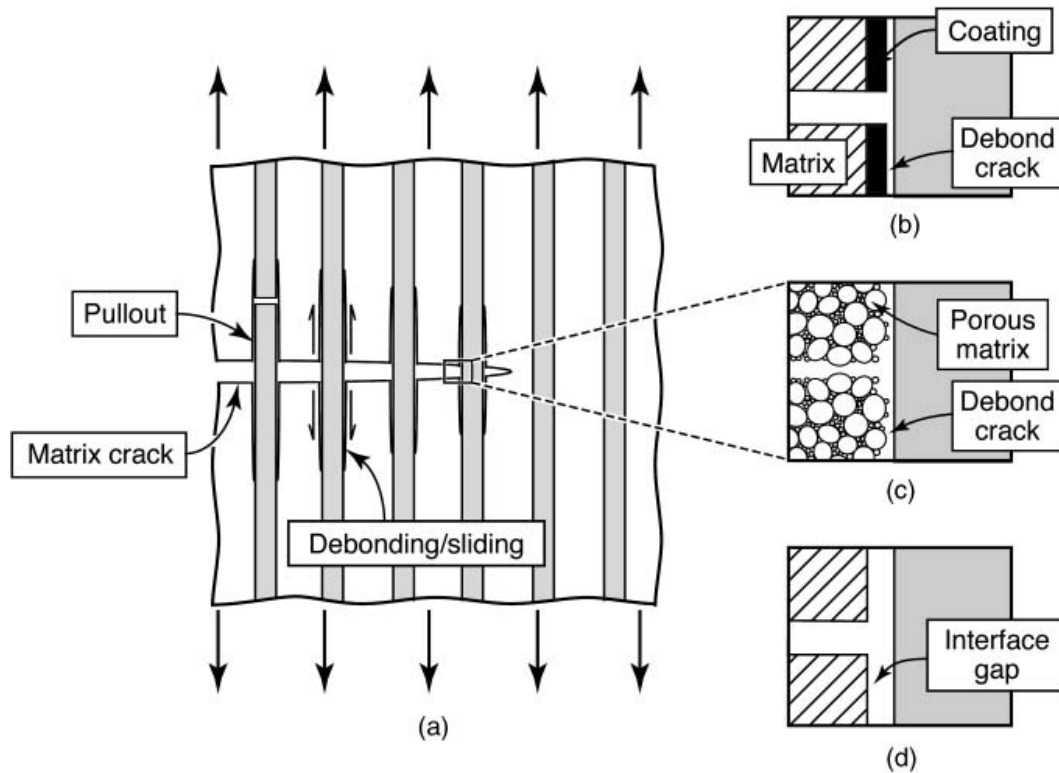


Figure 2. Damage Tolerance Mechanism of CMC's [24]

1.2.1 Oxidation

The high temperature combustion environment seen in a GTE poses many challenges due to oxidation of materials within it. For SiC CMC's, the main concerns are oxidation embrittlement and the degradation of the protective SiO₂ scale in the high temperature, high pressure flow gases [12]. One method to prevent or slow this oxidation

process is to apply an environmental barrier coating to the composite. Using an oxide/oxide CMC may be more beneficial, because it is immune to further oxidation.

1.2.2 Nextel™ 720/Alumina (N720/A)

The N720/A composite used in this study is composed of Nextel™ 720 Alumina fibers produced by the 3M™ corporation combined with an all-alumina matrix used by Composite Optics, Inc. (COI). This CMC relies on the porous matrix method to control its fiber and matrix interface. Table 1 shows the fiber properties.

Table 1. Nextel™ 720 Fiber Properties [1:16]

Property	Units	Nextel™ 720
Chemical Composition	Weight %	85 Al ₂ O ₃ 15 SiO ₂
Melting Point	°C	1800
Filament Diameter	μm	10-12
Crystal Phase		α- Al ₂ O ₃ + Mullite
Density	g/cc	3.40
Filament Tensile Strength (25.4 mm gauge)	MPa	2100
Filament Tensile Modulus	GPa	260
Thermal Expansion (100-1100°C)	ppm/°C	~5.8

The all-alumina matrix used in this CMC has an improvement in sintering properties over the previous aluminosilicate (N720/AS) matrix material used by COI with Nextel™ 720 fibers. Sintering in a ceramic matrix causes densification of the matrix, reducing its ability to spread cracks across the matrix surface. Matrix sintering in turn reduces the damage tolerance of the CMC. The alumina matrix used in N720/A was

developed to remain stable at temperatures up to 1200°C [2:6]. Table 2 shows properties of alumina.

Table 2. Alumina Properties [3:13]

Density (g/cc)	Melting Point (°C)	Young's Modulus (GPa)	Coefficient of Thermal Expansion (10⁻⁶/K)	Fracture Toughness (MPa m^{1/2})
3.9	2050	380	7 – 8	2 – 4

1.3 Fatigue Loading

Low cycle fatigue (LCF) is the dominant factor affecting materials in the combustor and turbine portions of a GTE. The sources of LCF cycles include engine speed changes (adjusting throttle settings), aircraft maneuvers, and thermal transients. Thermal transients are of important note because they cause temperature gradients, which can create large stresses due to uneven expansion and contraction in the materials [11:286].

Several fatigue tests have previously been performed on N720/A in a lab furnace environment. Fatigue testing has been accomplished at room temperature, 1200°C, and 1330°C [5; 19]. At 1200 and 1330°C, fatigue testing has also been performed in a 100% steam environment [5]. In addition, Fatigue testing at 1200°C was accomplished by the manufacturer of the CMC, with the results shown in Figure 3.

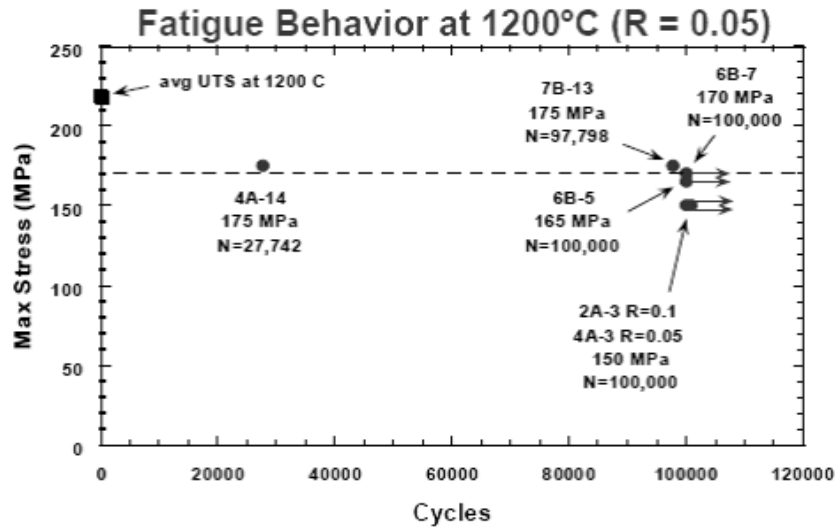


Figure 3. N720/A Fatigue Behavior at 1200°C [17]

Notch sensitivity to fatigue has also been accomplished on this CMC. Center hole and double edge notched specimens were tested at 1200°C [2; 20]. There has also been some work attempting to characterize CMC capabilities in a combustion environment. Research involved N720/A manufactured heatshields which were tested in a laboratory combustor [13; 16].

While N720/A has been tested separately in mechanical loading and combustion environments, there is still a necessity to combine the two. Monolithic ceramics are used frequently in combustors, but not as a structural component. CMC's allow the use of a ceramic structurally, but very little is known as to how they react while loaded in a combustion environment.

Combined combustion and loading testing can bridge the gap in knowledge between the two. However, this testing has not been performed in the past, because there are many technical challenges in combining the two tests that have made it undesirable to

attain. Efforts at AFIT allowed for the creation of a platform with the capability to combine these conditions. This test rig consists of a material test stand with a high-velocity flame that can contact a test specimen.

1.4 Combustion Environment

The combustion environment poses many challenges that are difficult to replicate on a typical material test specimen. Hot gasses are moving at high velocity, often exceeding Mach 1. Impingement of this high-speed gas on the material creates forces that are difficult to account for in specimen testing. Also, a non-isothermal condition is placed on the material by the temperature non-uniformity of the flame. This condition is difficult to replicate in a laboratory environment.

The presence of combustion pollutants that collide with the material at high velocities is also of concern. In the case of a gas turbine engine, these combustion pollutants would include unburned hydrocarbons, nitrogen oxides, carbon monoxide, and particulate matter such as fuel droplets [22:3]. The interaction of these compounds on a CMC with a porous matrix and their effects while the material is being fatigued is currently unknown.

1.5 Objectives

CMCs show great promise for use in high temperature aerospace applications. However, more characterization work needs to be accomplished before engineers can feel confident in using them in structural applications.

This research focuses on how N720/A reacts to a fatigue loading while being placed in a combustion environment. This enables creation of an S-N curve. Fatigue damage evaluation can also be completed. A residual strength test will also determine the amount of damage accumulated in the specimen by the combined combustion and fatigue loading.

The combustion environment consists of a single flame that impinges the middle of the specimen, heating the surface to a temperature of $1200 \pm 25^{\circ}\text{C}$. The fatigue loading is a tension-tension 1Hz sinusoidal load with a stress ratio of 0.05

$$(R = \sigma_{min}/\sigma_{max}).$$

II. Literature Review

A large amount of work has been compiled to characterize the fatigue behavior of N720/A and similar CMCs, such as N720/AS and N610/AS. This chapter focuses on previous testing of N720/A. These areas include fatigue, and notch sensitivity, and combustion environment testing.

2.1 Fatigue Testing

Steel performed fatigue testing of N720/A at room temperature and at 1200°C in a furnace. The fatigue tests were executed at 1Hz up to 100,000 cycles at maximum stresses of 60%, 70%, 80% and 90% UTS [19:Sec 3.2.2]. At room temperature, the fatigue properties degraded quickly above 70% UTS, with the 80% test only reaching 130 cycles before failure [19:Sec 4.3.1]. At 1200°C, fatigue testing was accomplished up to 90% UTS with no failure [19:Sec 4.3.2].

Steel also performed fatigue tests at 1200°C with moisture interruption. At prescribed fatigue cycles, the specimen would be removed from the test apparatus and placed in a fog chamber for 16 hours [19:Sec 3.2.3]. This testing was performed on 80% and 90% UTS fatigue specimens. Both specimens achieved 100,000 cycles [19:Sec 4.4].

Steel's run-out fatigue specimens were subjected to a residual strength test. The room temperature run-out specimens retained their tensile strength. The 1200°C specimens exhibited a 6% increase in tensile strength. The 1200°C moisture interrupted

specimens exhibited a 15% increase in tensile strength [19:Sec 4]. The testing showed that N720/A has excellent fatigue properties at high temperatures.

Eber continued the high temperature fatigue work of N720/A at 1200°C and 1330°C in air and 100% steam environments. The 1200°C specimens were fatigued up to 100,000 1Hz cycles at maximum stresses of 52%, 65%, 78%, and 88% UTS. In the air environment, the fatigue specimens all survived 100,000 fatigue cycles [5:24]. In the steam environment, failures occurred at 11,782 cycles and 202 cycles in the 78% and 88% UTS tests respectively [5:35]. The residual strength testing of the run-out specimens showed that the air specimens retained all of their strength, while the steam specimens exhibited a 10% drop in tensile strength [5:34, 45].

The 1330°C air and steam environment proved to be troublesome for the material. Fatigue tests were conducted up to 100,000 cycles at maximum stresses of 41% and 80% UTS. In both air and steam, all specimens failed in fatigue [5:24, 35]. The maximum cycles experienced were 97,000 cycles in air at 40% UTS. This work demonstrated that fatigue properties in air and steam at 1200°C are favorable. Conversely, N720/A performs very poorly in fatigue at 1330°C.

2.2 Notch Sensitivity Testing

Sullivan explored fatigue and creep behavior of center hole specimens in a 1200°C furnace. Fatigue testing was accomplished up to 500,000 1Hz cycles at maximum stresses of 79%, 84%, and 92% UTS [20:27-29]. The 79% UTS specimen achieved fatigue run-out, the 84% failed at 300,000 cycles, and the 92% failed at 8 cycles [20:42].

No residual strength testing was accomplished on the run-out specimen. This work showed that the material is sensitive in fatigue to center holes above 84% UTS.

Barth Boyer did fatigue and creep testing double edge notched specimens at 1200°C. His fatigue testing was up to 500,000 1Hz cycles at maximum stresses of 70%, 78%, 79%, and 81% UTS [2:28-29, 31]. The 70% UTS specimen achieved run-out, and the 78% and 79% specimens reached 196,000 and 129,000 cycles respectively. The 81% UTS fatigue specimen failed immediately [2:44]. Residual strength testing was not completed on the run-out specimen. Double edge notch sensitivity to fatigue is similar to that of the center notch when the maximum fatigue stress approaches 80% UTS.

2.3 Combustion Environment Testing

Some work has attempted to characterize N720/A capabilities in a combustion environment. Research has focused primarily on the survivability of N720/A in an advanced ultra-compact combustor that has been developed for future gas turbine engines. Panels were manufactured as a combustor heatshield and environmentally tested in this rig.

Parthasarathy et al. from the Air Force Research Labs conducted modeling and rig testing on N720/A and on N720 with an aluminosilicate (AS) matrix. Thermo-mechanical analysis on a finite-element model of the heatshield was done based on the material properties and computational fluid dynamic calculations. The modeling was used to determine service stresses, creep strain, and residual stresses from combustor cool-down. It was observed in the modeling that in-plane temperature gradients would

have the greatest effect on the material stresses during service. This was found to be especially prevalent in the $\pm 45^\circ$ direction, where the stresses could rise above the material limit [16].

In the experimental rig testing, both the N720/A and N720/AS panels were run in the combustor for ten hours. Temperatures at hot spots in the combustor reached 1200 – 1250°C during the rig testing. The N720/AS heatshield exhibited cracking in a location along the $\pm 45^\circ$ direction as the model predicted. The N720/A heatshield did not have any cracking, showing that it can be used in a combustion environment [16].

Mattoni et al. from the University of California, Santa Barbara also conducted combustion rig testing with N720/A. Two heatshields made of the material were run in an ultra-compact combustor for one to two hour intervals. The highest temperature seen by the heatshields were 1200 – 1225°C, localized around the fuel nozzles. The first heatshield was exposed for 20 hours, and the second heatshield was exposed for 86 hours. It was noted that there was delamination cracking emanating from the inner radius in both heatshields after rig exposure [13].

Tensile and Iosipescu specimens were machined from the heatshields in a $0^\circ/90^\circ$ orientation. Tensile testing revealed that the material exhibited a 10-20% decrease in tensile strength. However, the material exhibited a 15% increase in shear strength during the Iosipescu testing. It is thought that this behavior is a result of matrix sintering, which increased the fiber-matrix bond strength [13].

2.4 N720/A Behavior Overview

The previous testing of N720/A has shown that the material displays excellent fatigue behavior at 1200°C. The combustor rig exposure has also shown that N720/A can perform reliably with minimal degradation. However, the author is not aware of any study of N720/A under a combined mechanical and combustion environment test; which is the focus of this study.

III. Test Equipment and Experimental Procedure

This chapter presents the equipment and experimental procedures used in this research. The N720/A material background will be discussed, along with specimen preparation. The testing apparatus and the operating procedure will be reviewed.

3.1 Material Description

The N720/A CMC is manufactured by Composite Optics, Incorporated, now a division of ATK Space Systems. The manufacturing is accomplished using a sol-gel process. The Nextel™ 720 fibers are first woven into a fabric, in this case a satin weave. Figure 4 shows an example of a satin weave.

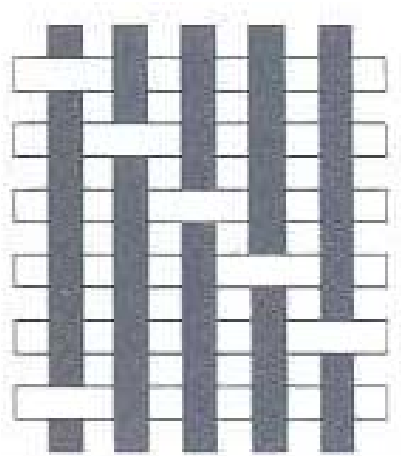


Figure 4. Satin Weave [3:51]

The fabric plies are immersed in a liquid slurry consisting of alumina and an organic binder. The fabric plies are laid up on tooling, and then the component is then cured in a vacuum bag at a low temperature. This curing process causes the alumina to bind into a gel, which then forms a porous matrix as it dries. The final step in manufacturing is to sinter the CMC at 1000 - 1200°C in order to preserve the performance of the fibers [15]. Figure 5 shows the CMC manufacturing process.

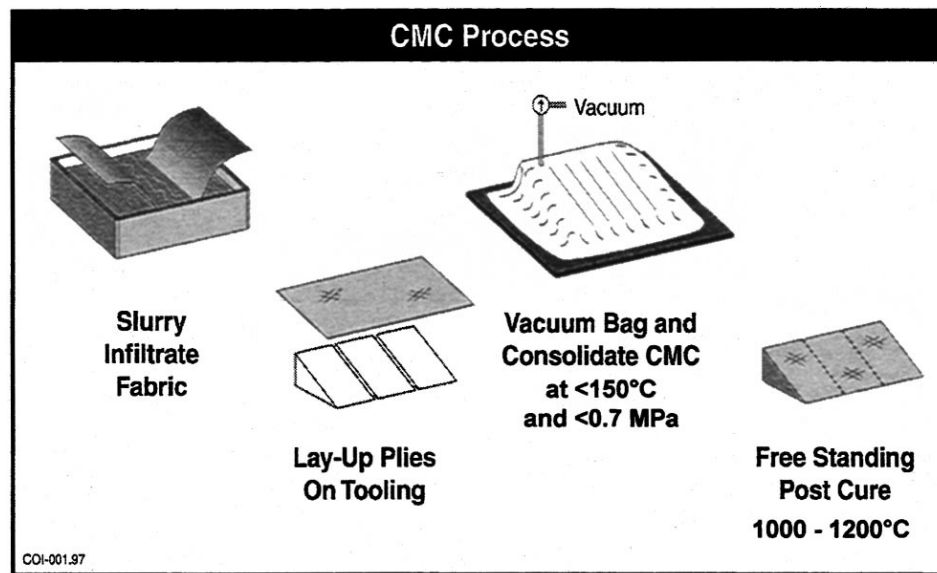


Figure 5. CMC Manufacturing Process [8]

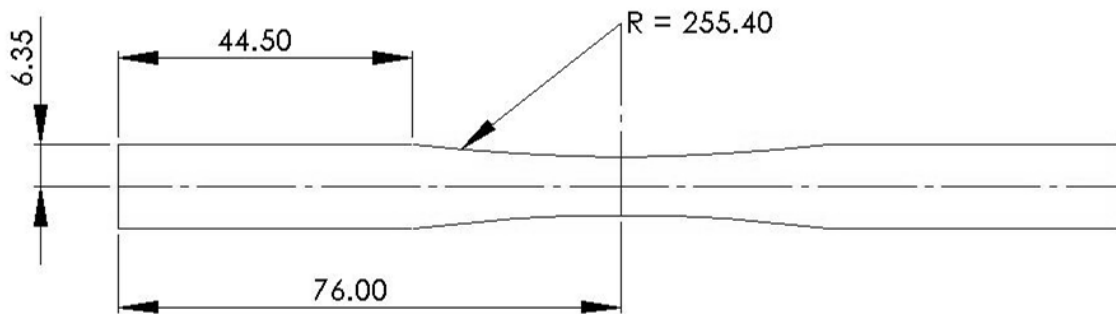
The N720/A panel obtained for this test was also used in previous AFIT thesis work by Boyer. It is a 12 in x 12 in panel consisting of an eight harness satin weave with a $[0^{\circ}/90^{\circ}]$ fiber orientation. The panel number is 4569-2. The panel properties obtained by Boyer are in Table 3.

Table 3. Panel #4569-2 Properties [2:15]

Thickness (mm)	Fabric Volume %	Matrix Volume %	Porosity %	Density (g/cc)
2.70	46.4	29.9	23.7	2.77

3.1.1 Specimen Geometry

The specimens were cut from the panel using a water jet. The panel was covered with a plexiglass sheet to provide a clean edge on the specimen from the water jet. After cutting, the specimens were dried in an oven at 90°C for three hours. The specimens were cut to a length of 152 mm and a width of 12.70 mm. A dog bone section was cut with a gage length of 63 mm and a minimum width of 8.80 mm. Figure 6 shows the specimen dimensions, and Figure 7 shows a picture of a prepared specimen.



Note: Not to Scale
Dimensions in millimeters

Figure 6. Specimen Dimensions

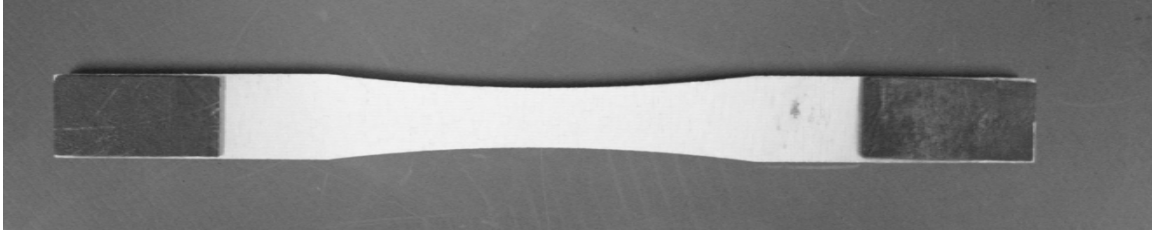


Figure 7. Photo of a Prepared Specimen

A large radius dog bone instead of a straight edge dog bone section was used because previous experience showed premature failure at the upper edge of the straight edge dog bone radius. Figure 8 shows an example of a straight edge dog bone specimen failure.

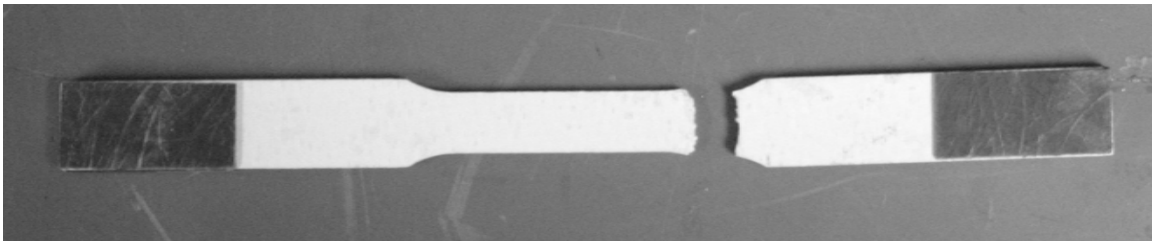


Figure 8. Premature Failure of Earlier Specimen Geometry

3.1.2 Thermal Emissivity

The temperature of the specimens in the combustion environment needed to be monitored throughout testing. The combustion environment is too harsh for a thermocouple to be positioned properly and remain on the specimen throughout the testing, so a Forward Looking Infrared (FLIR) system was used. The thermal emissivity

of the material was then needed to accurately determine the temperature the specimen was undergoing during the testing.

Thermal emissivity is defined as the ratio of a target surface's radiance to that of a "blackbody" at the same temperature. A blackbody is defined as an object that absorbs all of the radiant energy impinging on it and reflects none. The value of thermal emissivity ranges from zero to 1.0, where an object with an emissivity of 1.0 would be considered a blackbody [9:156-158]. Figure 9 shows representative emissivities of typical objects.

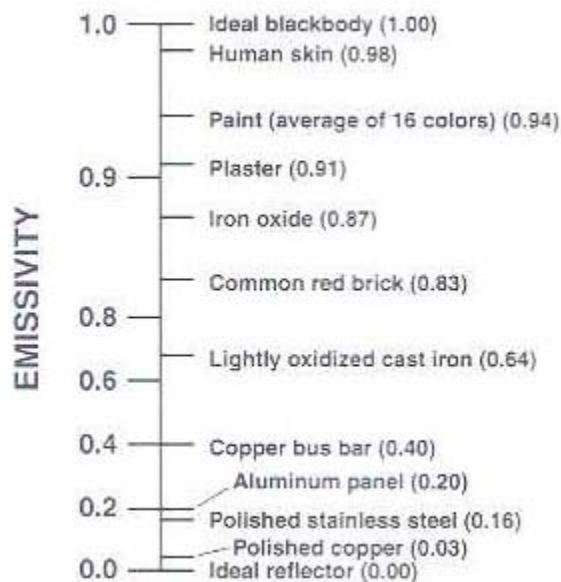


Figure 9. Representative Emissivities of Materials [7:62]

3.2 Equipment

The test equipment for this thesis work includes a Material Test Stand (MTS); a High-Velocity Oxygen Fuel (HVOF) flame system; Forward-Looking Infrared (FLIR) imaging system; and optical and scanning electron microscope (SEM) imaging devices.

3.2.1 Material Test Stand

The fatigue testing was conducted on a vertically actuated, servo-hydraulic MTS 858 Table Top System test stand. This machine is rated to a max force of 25 kN, but in testing it never exceeded 4 kN due to the small cross-sectional area of the specimens. The MTS machine is controlled through a computer workstation with a MTS TestStar™ II's digital controller and MTS *Multi-Purpose Testware* software. The digital controller provides an interface for signal generation and data acquisition, and the Testware provides a user interface to input testing instructions to the controller. Figure 10 shows the MTS test apparatus.

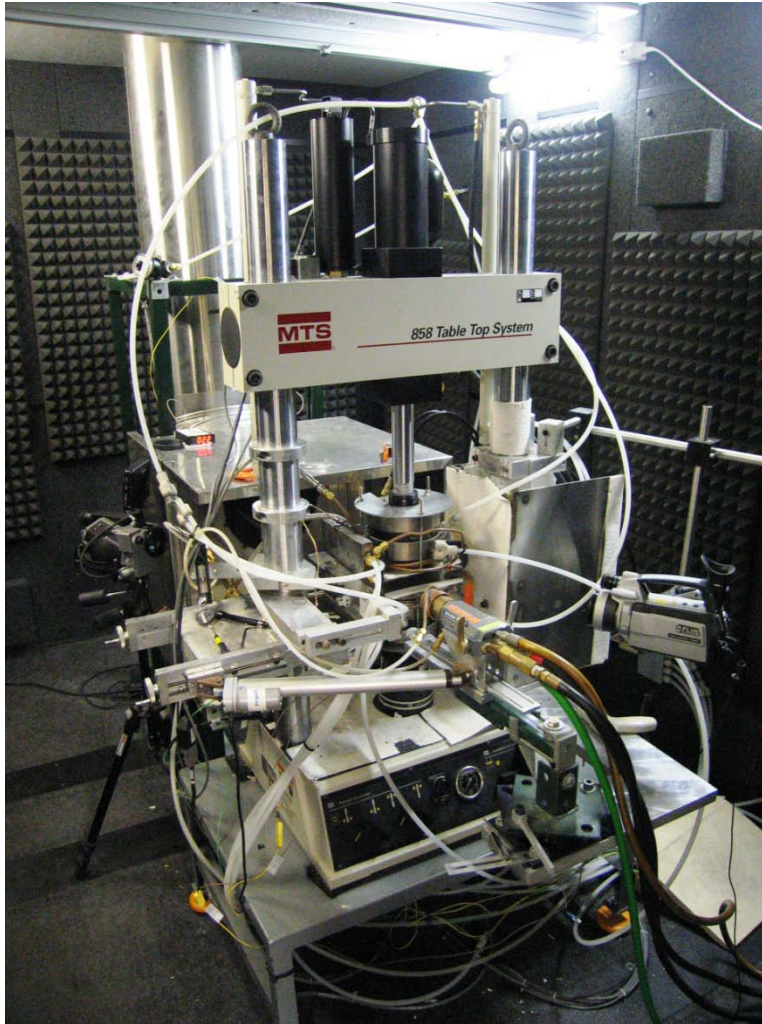


Figure 10. MTS Test Apparatus

The specimens were gripped with a pair of MTS 647 hydraulic wedge grips. The grip pressure used was 12 MPa. Using a flame to heat the specimen created a unique problem in keeping the grips cool, since there was no enclosure to help contain the heat of the flame solely on the specimen. In order to keep the grips cool, a multiple-layer insulating/cooling approach was needed. This first layer was copper coils held onto the grip surface by a steel plate bolted onto the grips. These copper coils flow 16°C deionized cooling water which is supplied by a NESLAB RTE 7 chiller. On the steel

plates, BUSTER M-35 ceramic plates were sandwiched between steel sheets which were clamped onto the steel plate. In addition, the wedge grips were cooled by lab air which was fed into them at 50 psi. The outer surfaces of the grips were also cooled with 15 psi lab air. The maximum temperature seen at the wedge grips with this scheme was 130°C, which is well below the 177°C temperature limit of the grips. Figure 11 shows the cooling scheme used on the grips.



Figure 11. MTS Grip Cooling Scheme

Load and grip displacement data were collected in the fatigue tests. This data was collected by a Model 359 Transducer, which is a linear variable displacement transducer (LVDT). The LVDT reads the displacement of the upper grip and outputs it as a function of voltage. The grip displacement data was used in place of an extensometer. This was

done because the high-speed flame could create undesirable forces on the extensometer, which could cause erroneous strain data.

3.2.2 High-Velocity Oxygen-Fuel Flame System

The combustion environment was created using a Sulzer Metco Diamond Jet (DJ) High-Velocity Oxygen Fuel (HVOF) spray gun system. The model used was the DJ9A, which has an air-cooled nozzle. These spray guns are typically used for thermal spraying applications throughout industry. The HVOF thermal spraying process uses oxygen and fuel gas (in this case propane) to produce a high velocity gas stream in the nozzle. The gas stream that is ignited creates a flame with a velocity of Mach 1 when using an air-cooled nozzle. This flame then melts the powder that is injected into it, which in turn creates a dense, tightly bonded coating on the material it is being used on [4:32-33]. To assist in the cooling of the nozzle, chilled water was fed to it by copper tubing coiled around it. Figure 12 shows a diagram of the air-cooled HVOF thermal spray process.

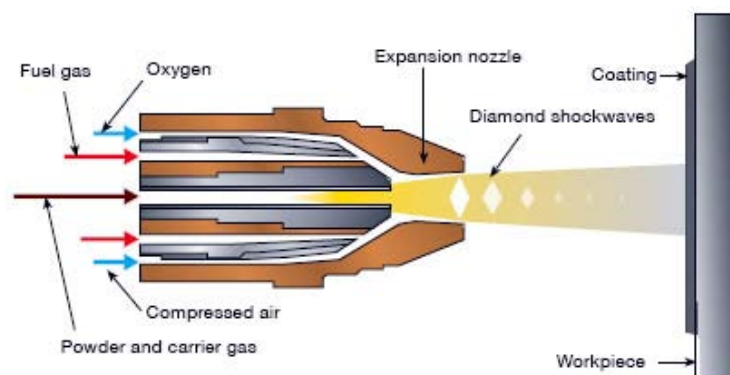


Figure 12. HVOF Thermal Spray Process [18]

The spray gun is mounted onto the MTS machine and is affixed to a rail system to allow it to be adjusted in the left-right and front-back directions. Figure 13 shows the DJ gun mounted in the rig.



Figure 13. DJ9A HVOF Spray Gun

To control the flame, a DJF Diamond Jet Gas Flowmeter unit was used. The flowmeter unit consists of three rotameters: one for oxygen flow; one for propane gas flow; and one for air flow. These three rotameters allow the user to accurately control the amount of each gas being fed to the spray gun to control its flame. Figure 14 shows the DJF gas flowmeter unit.



Figure 14. DJF Gas Flowmeter Unit

The propane and oxygen tanks are located in a tank farm outside of the laboratory building. There are three 120 Gal. liquid propane tanks and two oxygen tanks. The liquid propane needs to be gaseous for the HVOF system, and this is accomplished using a Zimmer LPG vaporizer. The oxygen tanks can supply up to 350 psi of gaseous oxygen and are controlled by a pressure manifold that takes oxygen from one tank at a time while testing. The manifold will only switch to the “secondary” tank when the oxygen pressure from the primary tank gets down to 90psi.

Having a spray gun that creates a Mach 1 flame creates a noise hazard. For the HVOF gun, the max noise level it can produce is 140 dB [4:13]. Because this gun needs to be run for extended periods of time for fatigue testing, it was necessary to contain the sound. To do this, a WhisperRoom SE2000 series sound room was used to contain the MTS machine and DJ spray gun. The room was modified to include an exhaust duct to remove the flames gas byproducts and heat from the room. An HFC-227ea fire suppression system was also added to the room in the event of a fire in the room. Figure 15 shows the Whisper Room.



Figure 15. Whisper Room

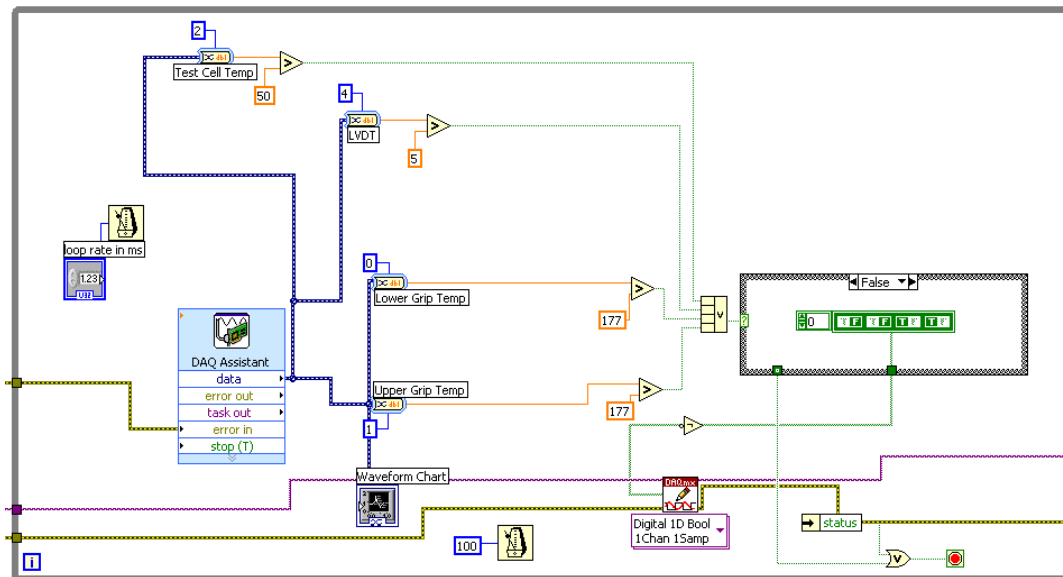
3.2.3 Safety Shutdown System

Using a high-speed, high temperature flame coating sprayer in a capacity other than its intended manufacturing purpose poses multiple risks. In order to mitigate these risks, an emergency shutdown program was put in place. This shutdown program was managed using National Instruments LabVIEW 8.2 software.

The program takes in inputs from a National Instruments data acquisition board, and uses limits set in the LabVIEW program to control electro-pneumatic pressure transducers that supply compressed air to pressure-operated valves on the oxygen and propane gas lines. The inputs used are thermocouples placed in the rig and the LVDT voltage. If the temperature from any of the thermocouples exceeds a set limit in the LabVIEW program; or if the LVDT voltage exceeds a certain value (which indicates a failure of the specimen), the air pressure being supplied to the valves would be shut off, which would extinguish the flame. Thermocouples were placed in the locations listed in Table 4, which also shows the shutdown limits used. Figure 16 shows the LabVIEW program limits in the form of a block diagram.

Table 4. Thermocouple Locations and Safety Limits

Thermocouple Location	Temperature Max Limit (°C)
Lower Grip	177
Upper Grip	177
Test Cell	50
Exhaust Duct (Outside Room)	For Reference Only
Exhaust Duct Inlet	For Reference Only
Gas Temp (aft of MTS machine before exhaust inlet)	For Reference Only



Another safety feature is a manual emergency button that will shut off power to the pressure transducers. In the event that the exhaust duct fans fail, an airflow-operated switch on the duct will also shut off power to the pressure transducers.

3.2.4 Forward-Looking Infrared System

The temperature of the specimen was recorded using a FLIR system. For the front of the specimen, which is where the flame impinged the specimen, a FLIR ThermaCAM P640 camera was used. A FLIR ThermaCAM PM695 camera was used to record the temperature at the backside of the specimen.

The ThermaCAM P640 has a 640x480 pixel infrared detector, with a $\pm 2\%$ accuracy and the ability to measure temperatures from -40 to 2000°C . The detector also has a spectral range of 7.5 to $13\text{ }\mu\text{m}$, with a minimum focus distance of 0.3m . The thermal sensitivity of the camera is 55mK at 30°C [6]. Figure 17 shows the camera mounted on the test stand.



Figure 17. FLIR ThermaCAM P640 Camera

The ThermaCAM PM695 camera is an older model with the same accuracy, temperature measurement range, and spectral range as the P640. However, it has a 320×240 pixel detector with a minimum focus distance of 0.5m . The thermal sensitivity is $< 0.08^{\circ}\text{C}$ @ 30°C , which is less than the P640 [21:56]. It is for these reasons that this camera was used to measure the temperatures at the back side of the specimen. Figure 18 shows this cameras placement in the room.



Figure 18. FLIR ThermaCAM PM695 Camera

For maximum accuracy in the temperature measurement, it is important to record the ambient temperature and humidity in the area where the FLIR cameras are located. These are adjustable settings in the cameras, and allow you to get the most accurate temperature readings. A Springfield Instruments Temperature and Humidity Monitor was used within the Whisper Room to accomplish this.

To measure the temperature at an area of interest in the viewing range of the camera, there are spot and area measurement modes. The spot measurement mode measures the temperature in a small location of the users' choice. The area measurement can be either a circle or a box, and will measure the maximum, minimum, and average temperature in the designated area.

For the front FLIR camera, the spot, circle, and box area measurements were all used. The spot measurement was placed in the region where the center of the flame was believed to be located. The circular measurement was placed at the center of the

specimen where the flame was impinging the specimen, with its diameter being the width of the specimen. The box measurement was placed at the upper end of the specimen, starting just above the circular measurement and ending where the specimen was no longer exposed. Figure 19 shows the measurement areas during a test.



Figure 19. FLIR Measurement during Testing

3.2.5 Specimen Imaging Equipment

All specimens were viewed with a low magnification optical microscope to see if there were any dominant specimen flaws before and after fatigue testing and fracture.

This was performed using a Zeiss Discovery V12 microscope with an attached Zeiss Axiocam HRC. Figure 20 shows the optical microscope

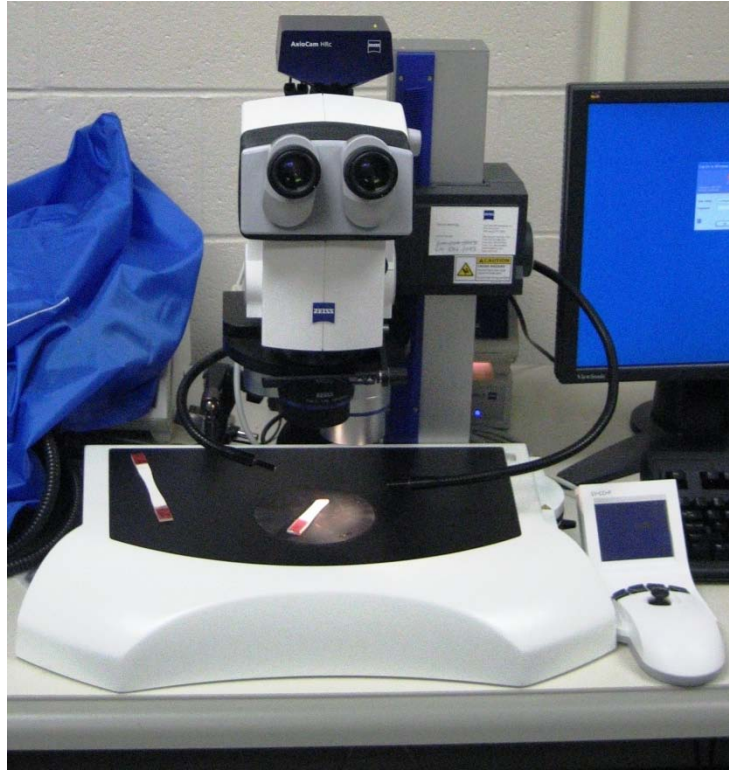


Figure 20. Zeiss Discovery V12 Optical Microscope

For the higher magnification viewing of the fracture surfaces, a Quanta 200 SEM was used. The SEM emits primary electrons which excites secondary electrons off of the specimen. The raster scanning of these electrons creates an optical image which is used to characterize the material. The N720/A material is nonconductive, which causes issues in SEM imaging because the primary electrons will strike the surface and build up, which distorts the image. To give the primary electrons a path, it is necessary to coat the specimen with a thin layer of conductive material. The specimens used for this study

were coated with gold for SEM imaging. This gold coating was applied using a SPI-Module 11428 coater. Figure 21 shows the SEM setup.



Figure 21. Quanta 200 SEM

The initial specimen preparation for SEM imaging involved cut the specimen to a size appropriate for use in the SEM chamber. This was accomplished using an MTI EC400 CNC saw with a diamond impregnated blade. The specimens were then mounted on aluminum tabs using silver paste. These were placed in an SPI-Module 11428 Sputter Coater to have a gold coating applied on their surface. Multiple layers were applied until the entire specimen was thoroughly coated. To ensure the specimens would have a

consistent ground, a bead of silver paste was applied where the specimen was attached to the tab. Figure 22 shows the specimens prepared for SEM characterization.

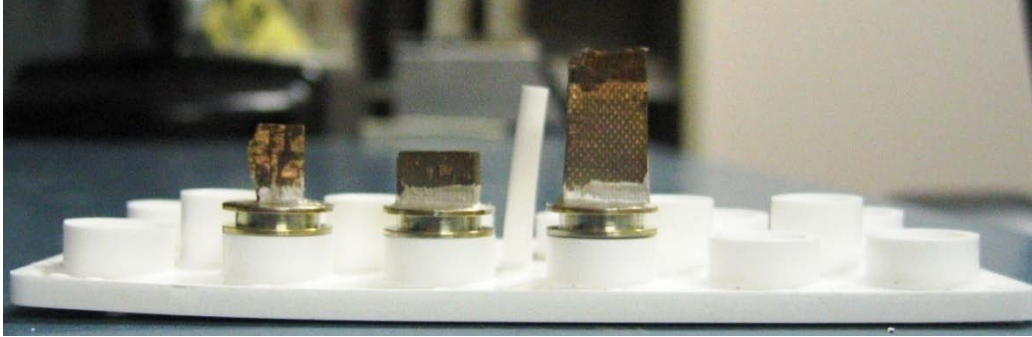


Figure 22. Specimens Prepared for SEM

3.3 Test Procedure

This section describes the specific procedures used during testing of the material. Microsoft Excel and MATLAB were used to document and analyze the data collected.

3.3.1 Specimen Inspection and Processing

The specimens were first inspected after fabrication for any major flaws such as edge damage or roughness from the water cutting process. The cross-sectional area of the specimens was measured across the width and thickness at the thinnest region of the dogbone. The cross-sectional area was then calculated using the equation

$$A = w * t \quad (1)$$

Where w is the width and t is the thickness of the specimen. To calculate the stress at the cross-sectional area, the following equation was used:

$$\sigma = \frac{P}{A} \quad (2)$$

Where P is the axial load placed on the specimen. The gage length of the dogbone was also measured and recorded in order to calculate the strain on the specimen. The calculation of strain was performed in the processing of the data using the equation

$$\varepsilon = \frac{\Delta L}{L} \quad (3)$$

Where L is the gage length of the specimen and ΔL is the change in length of the specimen while undergoing testing. The LVDT provided the displacement data that was used to calculate this change in length.

To prevent the grips on the MTS machine from damaging the specimen, it is necessary to place tabs on the ends of the specimen where they will be gripped. These tabs are fabricated from a glass fabric/epoxy material. These tabs were affixed to the ends of the specimen using an M-Bond adhesive. Two to three drops of the adhesive were applied to the surface of the specimen, the tabs were placed and pressure was applied to them for approximately one minute to ensure a good bond between the tab and the specimen.

3.3.2 Thermal Emissivity Analysis

The investigation of the thermal emissivity took place in a MTS furnace. A thermocouple was placed on the specimen, and fixed into the furnace at the appropriate distance and viewing angle (0.3 m away and 30° angle) that the FLIR camera would see in the HVOF rig. Figure 23 shows the setup used to determine the emissivity.



Figure 23. Emissivity Investigation Setup

The specimen was heated at 400°C intervals from 400°C to 1200°C. A 15 minute temperature soak at each temperature interval ensured an even surface temperature. After the soak, the FLIR thermal emissivity parameter was adjusted until the FLIR temperature matched the thermocouple temperature. The investigation results are discussed in Chapter 4.

3.3.3 Equipment Start-up and Specimen Loading

Before a test was started, the MTS hydraulic power unit was turned on and allowed to warm up. The *Multi-Purpose Testware* (MPT) would be loaded onto the workstation, along with the LabVIEW control system software. The MTS procedure would be loaded into the MPT, and would be adjusted based on what stress range the specimen would be undergoing. The specimen file name, acquisition rate, and data file destination in the workstation were also chosen.

Once the hydraulic system was warmed up, the test specimen would be placed within the grips. The grips would be placed in the open position, and the upper grip would be displacement controlled and moved to allow for space for the specimen to be placed between the grips. The specimen was placed in the upper grip first and the left edge of specimen (looking from the front of the MTS machine) was placed so it touched the alignment tool on the grip. The alignment tooling is used to align the upper and lower ends of the specimen in the grips to ensure that the specimen is perfectly vertical. The upper grip is then closed, and the verification that the specimen end tabs were completely gripped was performed using a small mirror and a flashlight. The upper grip was then slowly lowered under displacement control until the lower end tabs of the specimen were within the lower grips. Once the placement in the lower grips was verified, the upper grip would be opened, and the left edge of the specimen would be butted against the alignment tool on the upper and lower grips. This was done carefully to limit the amount of vertical movement of the specimen while was free between the grips. The upper grip was then closed, and while setting the MTS stand into force command and zeroing the

force, the lower grip would be closed. This was done to prevent the specimen from being unintentionally damaged from being compressed. A final verification of the gripping of the tabs using the mirror and flashlight was then performed. This verification with a mirror and flashlight is necessary because the grip cooling scheme makes the grips visible only from a hole in the steel plates, making it very difficult to see how much of the specimen end is in the grip. Once the placement of the specimen in the grips was satisfactory, the ceramic plates would be arranged around the specimen and clamped down with a steel plate to keep them from moving during testing.

3.3.4 HVOF and Temperature Measurement Start-up

The Zimmer LPG vaporizer uses heat to gasify the liquid propane, so this is turned on first to allow it to warm up. The NESLAB chiller is turned on to ensure the grips and the HVOF spray gun nozzle will be at 16°C at the start of testing. The air supply valves controlling the lines that go to the inside and outside of the grips are turned on and set to 50 psi and 15 psi respectively. The FLIR cameras are turned on, and the ambient temperature and humidity settings are adjusted to the measured values in the whisper room. The two exhaust fans are turned on, and the LabVIEW control system is turned on to start displaying temperature data and to open the oxygen and propane pressure valves. Figure 24 shows the control system display.

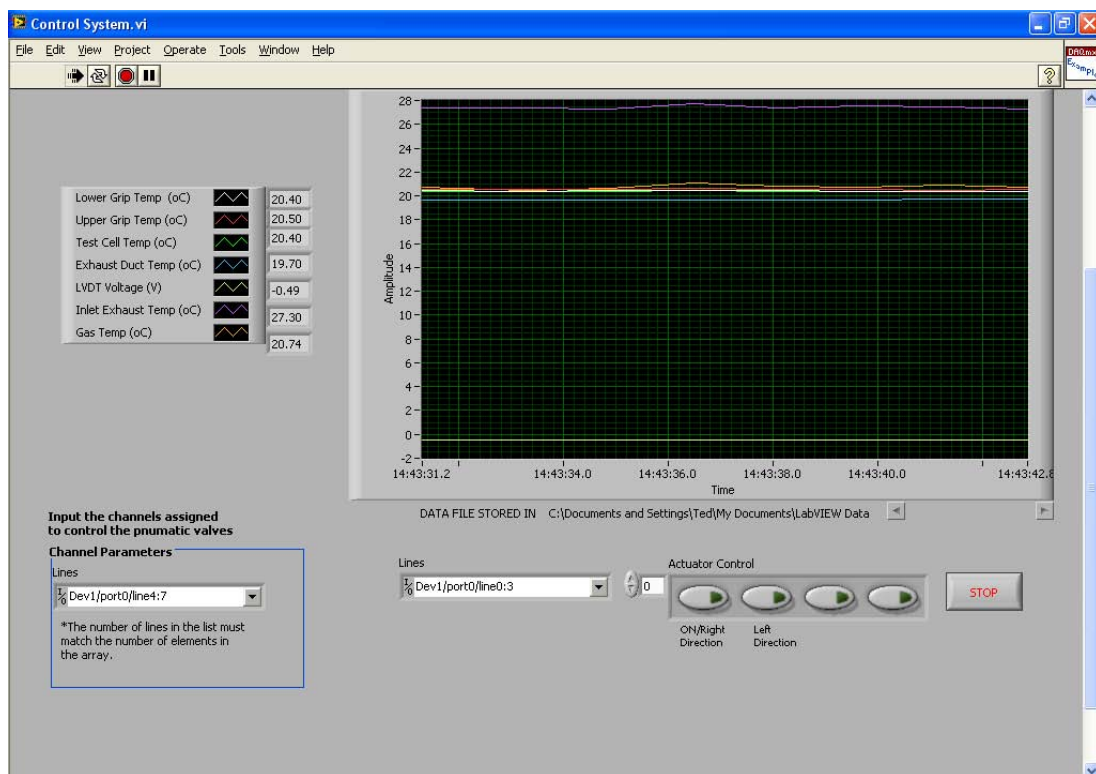


Figure 24. Control System Display (Pretest)

Once the LPG vaporizer has been warmed up, the propane and oxygen tanks are all opened. The spray gun valve is opened, and the flow and pressure is adjusted on the each of the flowmeters to a set parameter. Table 5 shows the flow and pressure parameters used for each gas during testing. The flow was measured in standard cubic feet per hour (SCFH) and the line pressure was measured in psi. These flow and pressure parameters were developed by the developer of this test rig.

Table 5. Pressure and Flow Parameters

Gas	Flow (SCFH)	Pressure (psi)
Propane	52 ± 1	20
Oxygen	217 ± 3	45
Air	368 ± 5	30

After the pressures and flows are set for each gas, the spray gun valve is shut off. The spray gun is also adjusted so it is pointing to the left of the specimen using the two rail adjustment knobs. This is done to ensure the initial flame has an obstacle-free space to start and stabilize. When the flame has started and stabilized, the flow parameters are rechecked and adjusted as necessary on the flowmeters.

After the flame is stable and the flow parameters are set, the spray gun is carefully moved towards the specimen. As the spray gun is being moved the temperature of the specimen is being watched using the FLIR camera viewfinder. Once the desired average temperature in the circle measurement area reached approximately 1200°C, testing could begin. Once fatigue testing began, both FLIR cameras were programmed to obtain thermal images at ten minute intervals.

3.3.5 Fatigue Tests

Six specimens were loaded under a tension-tension fatigue test regime under the combustion environment. The fatigue loading was applied using a sinusoidal wave at 1Hz with a stress ratio of 0.05. Peak/Valley Compensation (PVC) was used during the testing to ensure the applied force loads matched the commanded force loads. Figure 25 shows the fatigue loading with PVC compensation.

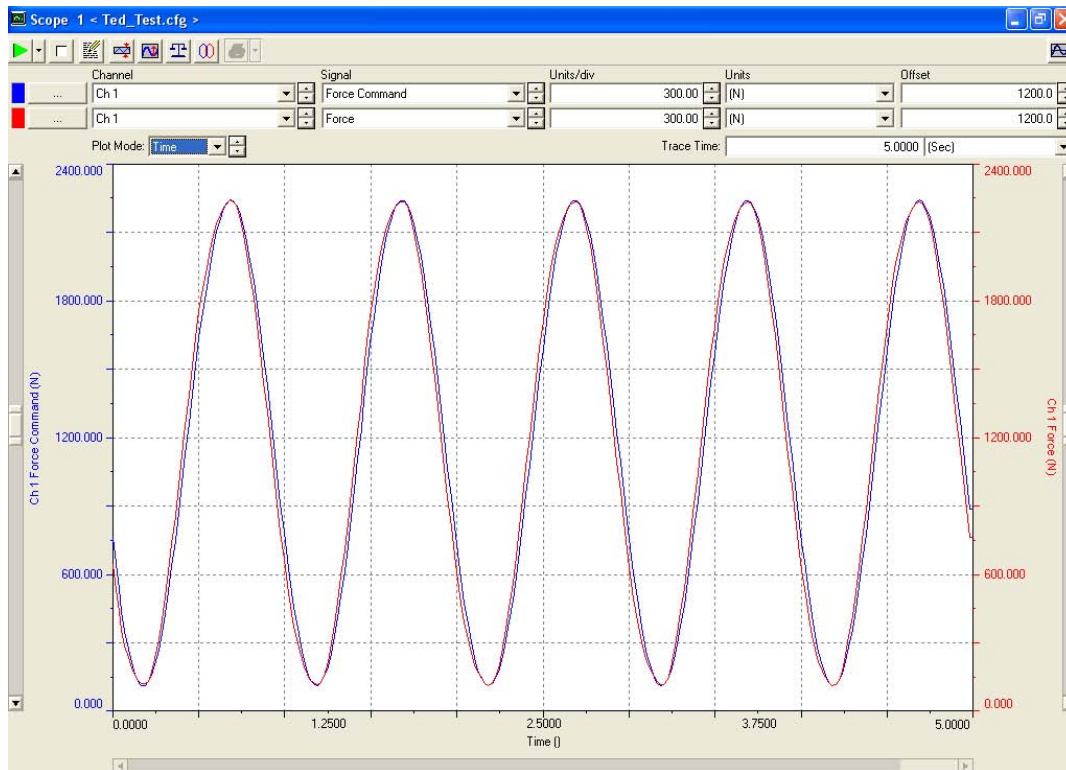
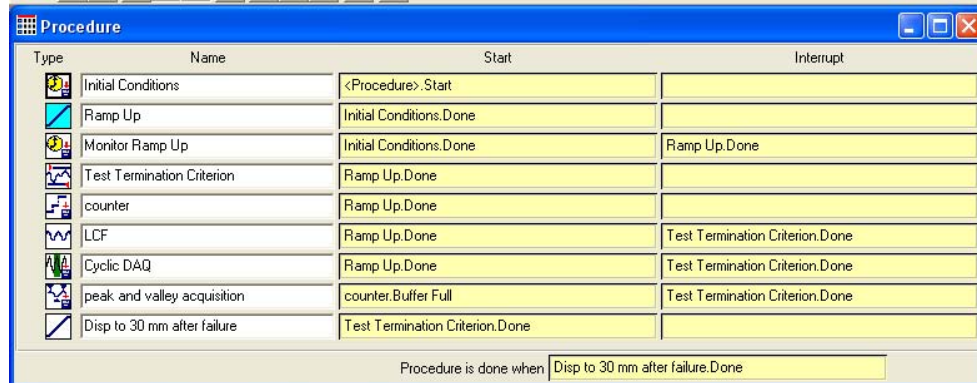


Figure 25. Cyclic Loading with PVC Compensation

The MTS machine exhibited a slow force compensation response at the start of fatigue testing. When fatigue loading began, the maximum and minimum force applied would be above and below the respective force command. The pattern would typically continue through the first 50 cycles of fatigue testing before applying the prescribed cyclic load. Even with frequent tuning of the control software, this issue affected all fatigue testing performed.

During the fatigue testing, the following data was recorded: time/date; test run-time; maximum and minimum force; displacement, and cycle count. Hysteresis and peak and valley data collection modes were used. The peak and valley data collection gathered the maximum and minimum force and displacement data throughout the testing.

It also recorded the force ramp-up data before the fatigue testing began. The hysteresis data was collected on log cycles (i.e. 1, 2, 5, 10, 20, 50, ...). Both were recorded at a rate of 1024 Hz. The fatigue run-out was at 90,000 cycles, which is 25 hours. Figure 26 depicts the fatigue test program.



Type	Name	Start	Interrupt
Initial Conditions		<Procedure>.Start	
Ramp Up		Initial Conditions.Done	
Monitor Ramp Up		Initial Conditions.Done	Ramp Up.Done
Test Termination Criterion		Ramp Up.Done	
counter		Ramp Up.Done	
LCF		Ramp Up.Done	Test Termination Criterion.Done
Cyclic DAQ		Ramp Up.Done	Test Termination Criterion.Done
peak and valley acquisition		counter.Buffer Full	Test Termination Criterion.Done
Disp to 30 mm after failure		Test Termination Criterion.Done	

Procedure is done when: Disp to 30 mm after failure.Done

Figure 26. Fatigue Test Program

3.3.6 Ultimate and Residual Strength Tests

It was necessary to provide a baseline ultimate stress in the combustion rig to perform the fatigue testing. A specimen was placed in the rig and the flame was applied, heating the center of the specimen to $\sim 1211^{\circ}\text{C}$. The specimen was monotonically tested under force control at a rate of 20 N/sec. The force and displacement data were recorded at 100Hz until failure of the specimen.

Upon fatigue test completion, select specimens were monotonically tested at room temperature to determine the retained strength of the material. The testing was performed on an MTS 810 test stand. Load data was collected via a MTS 661 Force Transducer. An MTS 63.26E-30 extensometer was used to collect the strain data. The extensometer

was placed directly on the specimen and held on with rubber bands. The monotonic testing used a displacement control rate of 0.5 mm/sec. The load and strain data were collected at 100Hz until specimen failure.

3.4 Test Matrix

Table 6 shows the test matrix used for the fatigue testing in this study. All of the specimens in this study were made of N720/A and used a dogbone configuration.

Table 6. Test Matrix Under the Combustion Environment

Specimen #	Loading Type	Max Stress (MPa)	% UTS
UTS	Tensile	167	100
3	Fatigue	60	36
5	Fatigue	94.5	57
6	Fatigue	108	65
7	Fatigue	121.5	73
8	Fatigue	142	85
10	Fatigue	150	90

IV. Results and Analysis

This chapter presents the results and analysis of the fatigue testing of the CMC in the combustion environment. The data will be compared to previous fatigue data performed on N720/A under the laboratory and 100% steam environment. Microstructural characterization of the fracture and fatigue surfaces of the material will also be presented.

4.1 Thermal Emissivity Data

In order to accurately measure the temperature of the specimen using the FLIR system, the thermal emissivity needed to be determined. Table 7 shows the thermal emissivity data for each test temperature in the furnace.

Table 7. Emissivity Values versus Temperature

Temperature (°C)	Thermal Emissivity
400	0.89
800	0.91
1200	0.93
1250	0.93

The emissivity below 1200°C varies between 0.89 and 0.91. Above 1200°C, the thermal emissivity is determined to be 0.93. This emissivity value is further validated by a NASA paper that looked at the emissivity of N720/A at 1124°C. In their research, spectrometer data was recorded versus a range of wavenumbers for the material. Over

the spectral range of the FLIR camera, the average value of the NASA data at 1124°C was 0.93, with a standard deviation of 0.084 over 37 data points [14].

4.2 Specimen Temperatures in Testing

Using a flame to heat the specimen created temperature variations during testing. Flames are inherently unstable, and thus are difficult to work with when you are attempting to create a steady temperature on a surface. It was necessary to take temperature recordings every ten minutes to be able to get an overall observation of the specimen temperatures during the 25 hour test. Chapter 3.2.4 describes where the measurements were taken during testing, and it is at these locations where the temperature data was analyzed. The primary focus zones for the temperature analysis were the circular area on the front surface, the box area on the rear surface, and the center spots on both the front and rear. All of these were in the central region of the specimen. Average temperatures during testing were calculated for each location, and the maximum temperatures seen on the front surface were also recorded. The average temperature on the flame side surface was taken over a 38mm² circular region. The maximum temperature is useful in determining if sintering of the matrix occurred. Table 8 to Table 10 show the temperatures during each 25 hour fatigue test.

Table 8. Flame Side Area Temperature Data

Specimen Number	Area Max (°C)	Area Average (°C)	Standard Deviation
#3	1282	1201	13
#5	1302	1193	95
#6	1281	1193	94
#7	1289	1198	113
#8	1268	1203	6
#10	1267	1205	5

Table 9. Rear Area Temperature Data

Specimen Number	Area Average (°C)	Standard Deviation
#3	697	98
#5	723	46
#6	No Rear Data	N/A
#7	No Rear Data	N/A
#8	653	27
#10	696	76

Table 10. Spot Temperature Data

Specimen Number	Flame Side Spot (°C)	Rear Spot (°C)	Temperature Difference (°C)
#3	1228	782	446
#5	1230	830	401
#6	1234	No Data	N/A
#7	1238	No Data	N/A
#8	1244	684	560
#10	1245	760	485

As seen in Table 9, the average temperature where the flame hit the specimen was ~1200°C. However, the max temperature seen on the surface from the flame was as high as 1300°C, which is where mullite formation can occur in the matrix [16].

A temperature profile over the gage length of a specimen in the rig was also analyzed. The profile allowed for an expanded view of the temperatures seen while

being exposed to the flame. Temperature data was collected from the front and rear thermal images of specimen #8 at one instance in testing. Figure 27 shows the temperature profiles over an approximated distance from the center of the specimen. Rear profile data was not obtainable for the entire gage length because there was equipment that obstructed viewing of the top and bottom portions of the specimen.

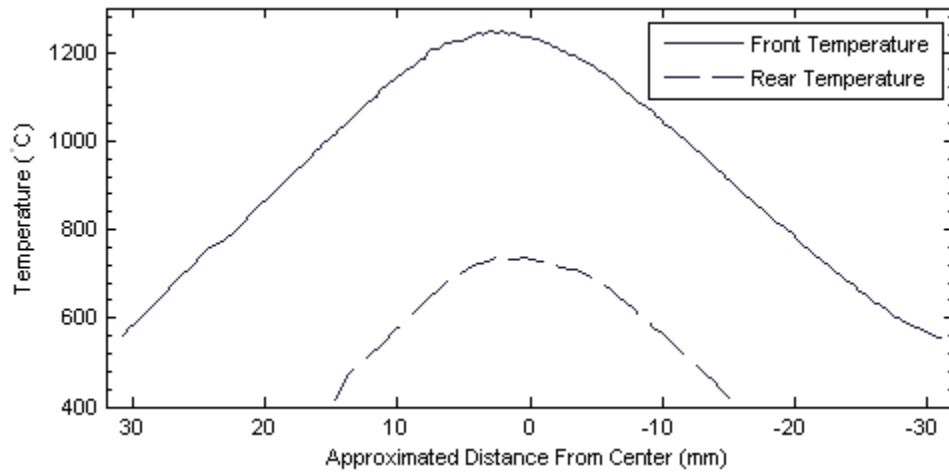


Figure 27. Front and Rear Temperature Profiles

The temperature falls in a linear fashion beyond the region where the flame is applied. The difference between the front and rear surface temperatures also stays constant, in this case approximately 500°C.

4.3 Thermal Strain during Testing

The thermal strain was calculated using the LVDT displacement data while there was no load placed on the specimen. The displacement was recorded in ambient

temperature conditions and after the specimen was heated to approximately 1200°C by the flame. The thermal strain was then used to calculate the coefficient of thermal expansion for the specimen. The coefficient of thermal expansion is calculated using the equation

$$\alpha_t = \frac{\varepsilon_t}{\Delta T} \quad (4)$$

Where ε_t is the thermal strain and ΔT is the difference between ambient and specimen temperature. Table 11 shows the thermal strain and coefficient of thermal expansion for each test specimen.

Table 11. Thermal Strain and Expansion of N720/A in a Combustion Environment

Specimen Number	Temperature when Strain Recorded (°C)	Thermal Strain %	α_t (10⁻⁶/°C)
UTS	1212	0.3421	2.88
3	1208	0.3464	2.92
5	1208	0.3886	3.28
6	1213	0.3558	2.99
7	1209	0.3601	3.04
8	1219	0.3585	3.00
10	1221	0.3726	3.11
	Average	0.3606	3.03
	Std. Dev.	0.0158	0.13

Because the specimen was not in an isothermal environment, the thermal strain and coefficient of thermal expansion is lower than the published value of 6×10⁻⁶/°C from COI [17]. To get a better approximation of the thermal expansion, the temperature

profile data shown in Figure 27 was averaged and used. For an average specimen temperature of 700°C, the thermal expansion coefficient was calculated at $5.30 \times 10^{-6}/^{\circ}\text{C}$, which is close to the published value. For alumina, the coefficient of thermal expansion is constant from 100 - 1100°C, so this calculation is appropriate for the material [3:264].

4.4 Monotonic Tensile Test

To provide a baseline stress to accomplish fatigue testing, the tensile strength of the material needed to be determined in the combustion environment. The stress at failure was compared to tensile strength data from Sullivan, Eber/Harlan, and COI. Figure 28 shows the stress-strain curve. Table 12 shows the previous tensile strength data in 1200°C air and the tensile strength in the combustion environment.

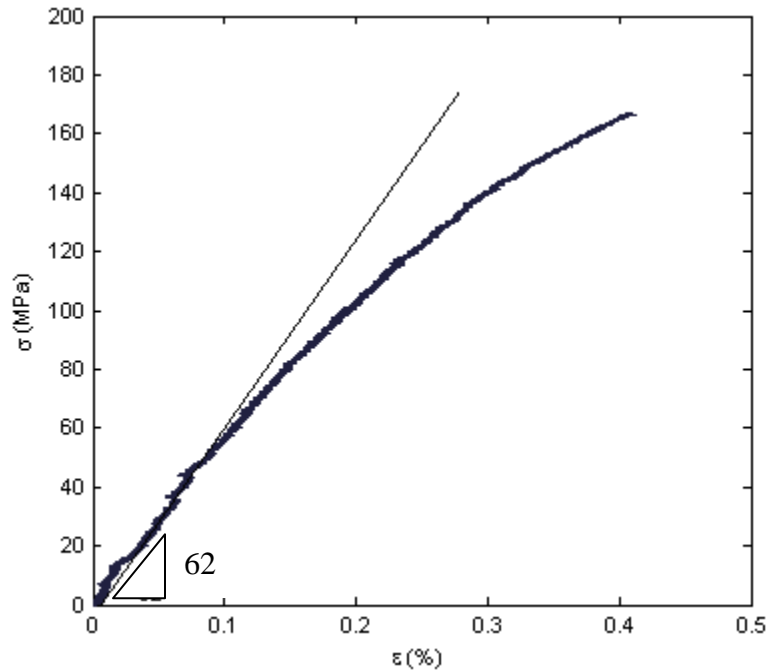


Figure 28. Combustion Environment Tensile Strength

Table 12. Tensile Strength Data

Source	Temperature °C	Elastic Modulus (GPa)	Ultimate Tensile Strength (MPa)	Failure Strain %
Sullivan ⁽¹⁾	1200	85	200.2	.35
Eber ⁽²⁾	1200	74.7	192.2	.38
COI ⁽³⁾	1200	69	224	.44
Average	1200	76.2	205.5	.390
Mattoni ⁽⁴⁾	1200-1250	62	145	.28
Combustion	1211	62	166.8	.41

NOTE: (1) Ref [20:31]; (2) Ref [5:20]; (3) Ref [17]; (4) Ref[13]

This data shows that the tensile strength of the material in a combustion environment decreased by 19%. This tensile strength decrease coincides closely with the loss in tensile strength observed by Mattoni et al. after exposure to the combustion environment for 86 hours [13]. For the fatigue testing in the combustion environment, the ultimate strength referred to is 166.8 MPa.

4.5 Fatigue Tests

Six dog bone specimens were tested under a tension-tension fatigue load while being impinged by a flame which locally heated the specimen to approximately 1200°C. The fatigue loading was applied in a 1Hz sine wave with a stress ratio of 0.05. The fatigue testing lasted 25 hours for a total of 90,000 cycles. Table 13 shows the summary of all of the fatigue testing. The % UTS in the table is normalized to the 166.8 MPa tensile strength that was determined in the combustion environment tensile test. Figure 29 shows the fatigue stress versus cycle curve for the N720/A specimens in the combustion environment.

Table 13. Fatigue Test Summary

Specimen Number	Fatigue Stress (MPa)	Fatigue Stress (% UTS)	Cycles to Failure	Failure Location
3	60	36	>90,000	Run-out
5	94.5	57	>90,000	Run-out
6	108	65	>90,000	Run-out
7	121.5	73	>90,000	Run-out
8	142	85	>90,000	Run-out
10	150	90	>90,000	Run-out

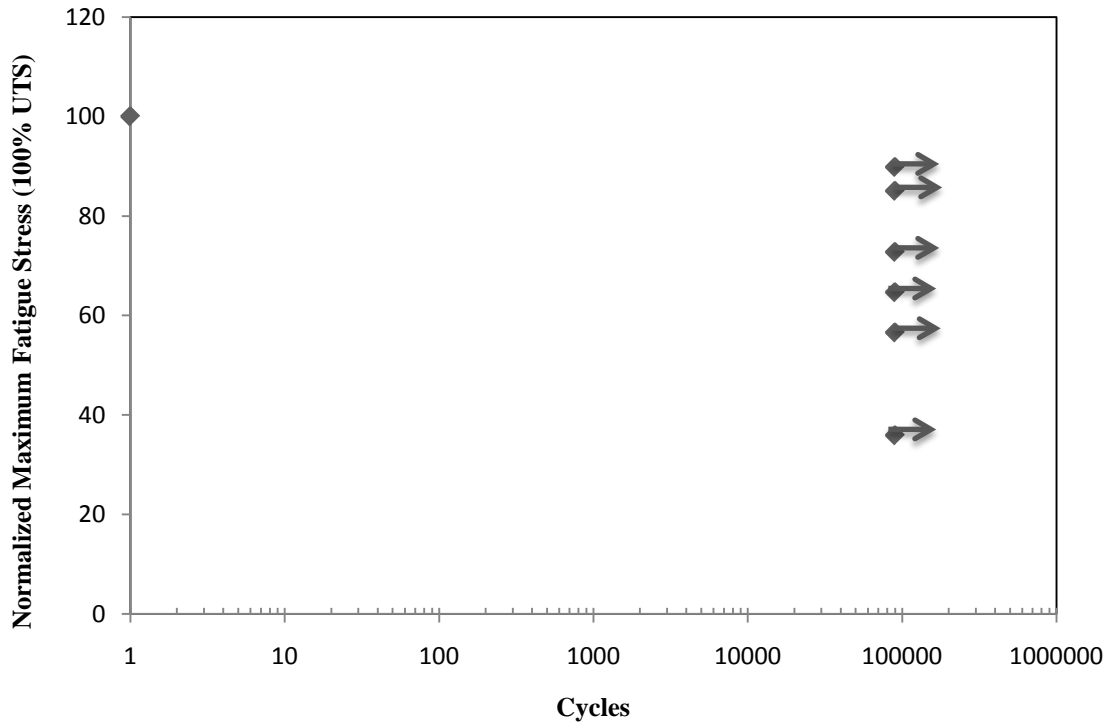


Figure 29. Fatigue Stress versus Cycles

This fatigue data correlates closely to the work done by Eber [5]. Figure 30 shows the combustion environment fatigue stress versus cycle curve compared to Eber's fatigue data. It appears from this data that N720/A exhibits a "go/no-go" behavior in fatigue at 1200°C, where the specimen will either fail very early in fatigue or not at all.

Figure 30 shows that the combustion environment fatigue behavior is similar to the laboratory air fatigue behavior at 1200°C.

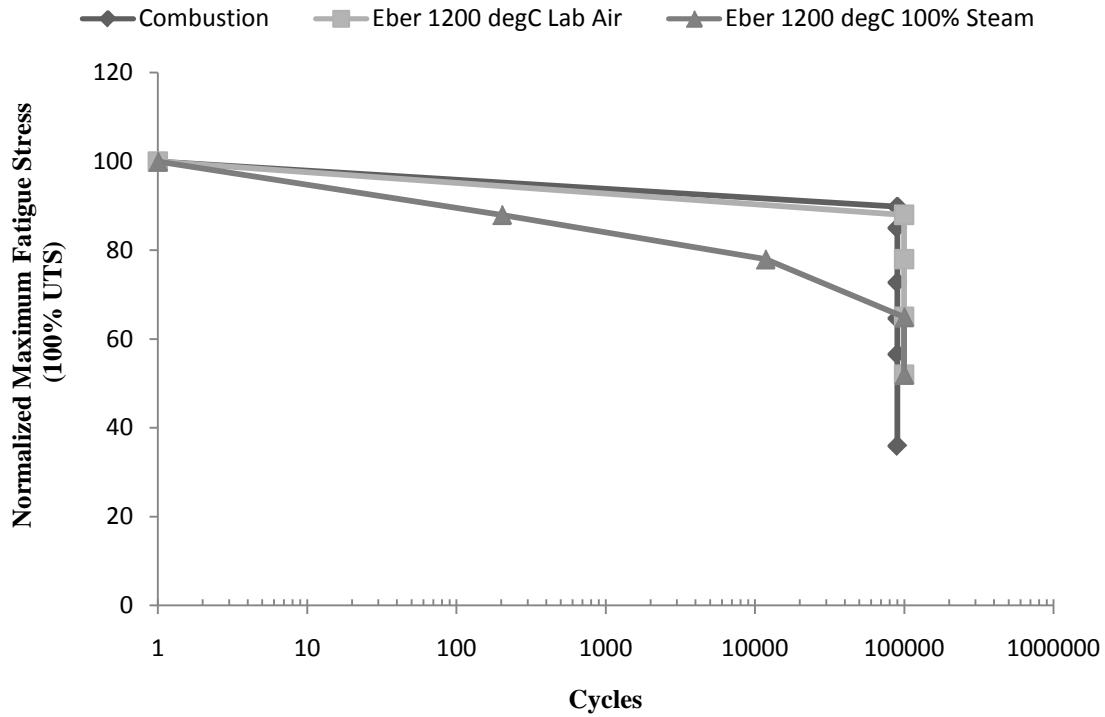


Figure 30. Normalized Fatigue Stress versus Cycles Comparison with Eber Data

4.5.1 Fatigue Strain Hysteresis

Strain hysteresis data was recorded by the throughout the fatigue testing. The area in the hysteresis loop is an indicator of the strain energy present in the material.

Figure 31 to Figure 36 show the hysteresis loops for each fatigue specimen.

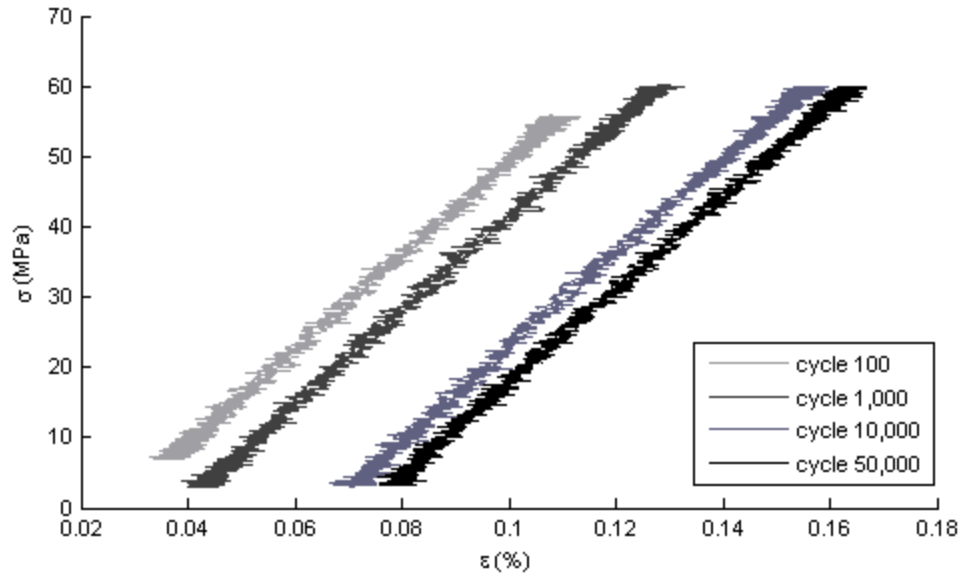


Figure 31. 60 MPa Hysteresis Data

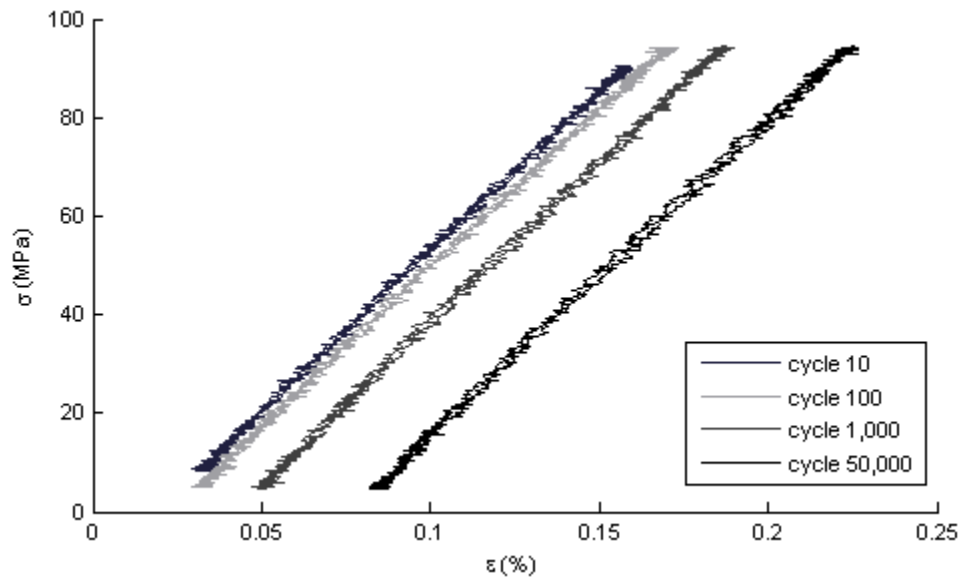


Figure 32. 94.5 MPa Hysteresis Data

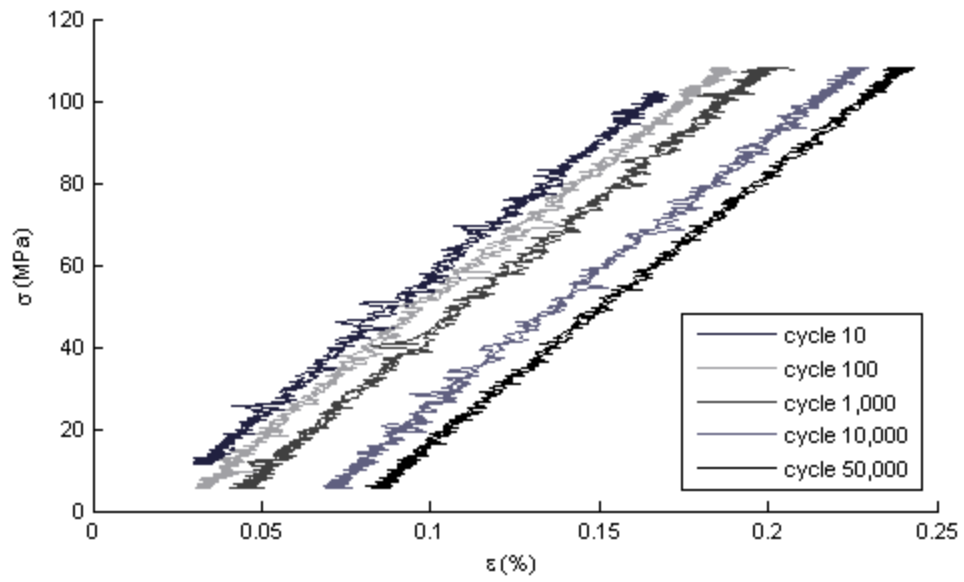


Figure 33. 108 MPa Hysteresis Data

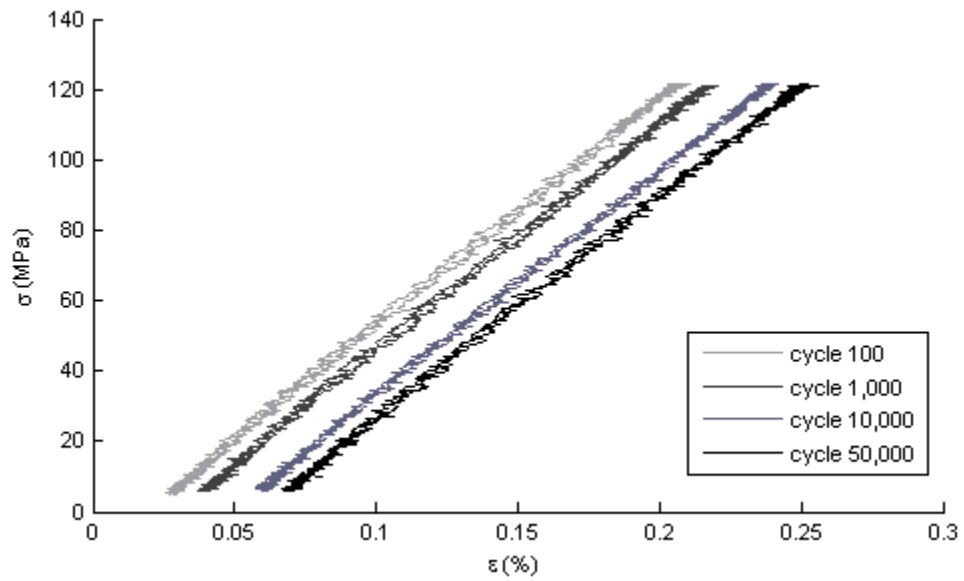


Figure 34. 121.5 MPa Hysteresis Data

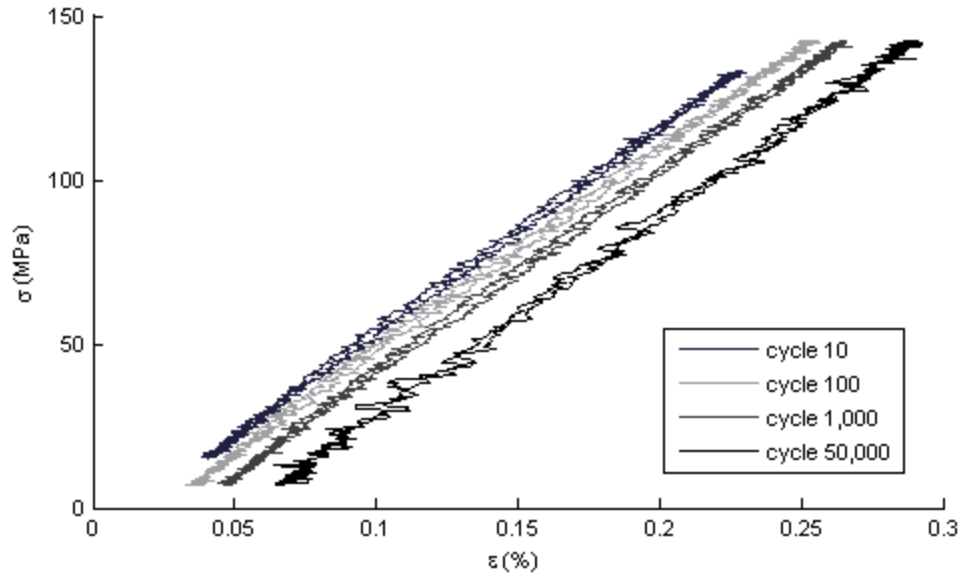


Figure 35. 142 MPa Hysteresis Data

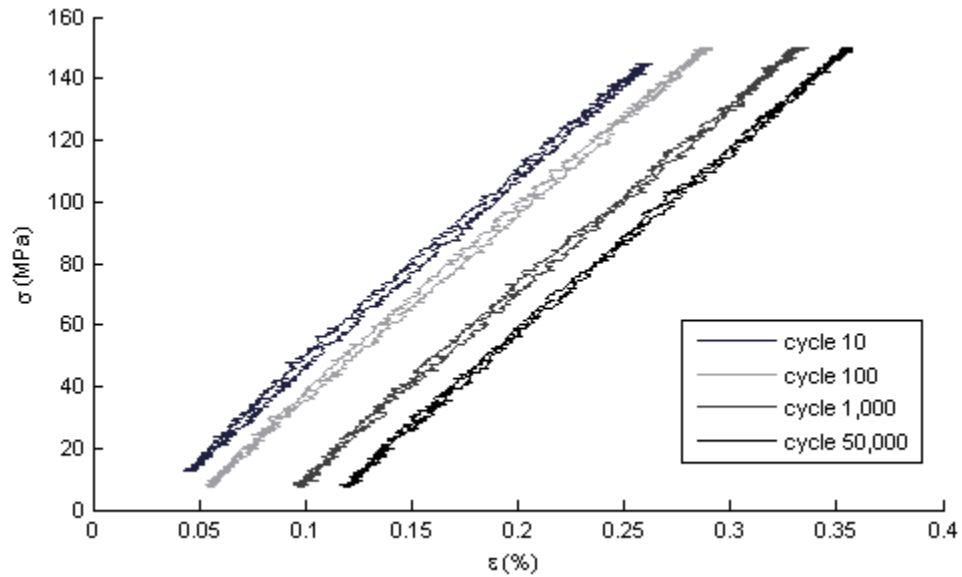


Figure 36. 150 MPa Hysteresis Data

All of the hysteresis figures show a linear elastic response throughout fatigue life. Each cycle exhibits a very small area, indicating that the fatigue cycles cause only a small amount of damage to the material. Creep over the fatigue test regime is the most likely

cause of the damage since maximum strain was increasing with cycles over its life.

Another way to view the increasing strain over time during fatigue testing is to look at the maximum strain for each recorded cycle.

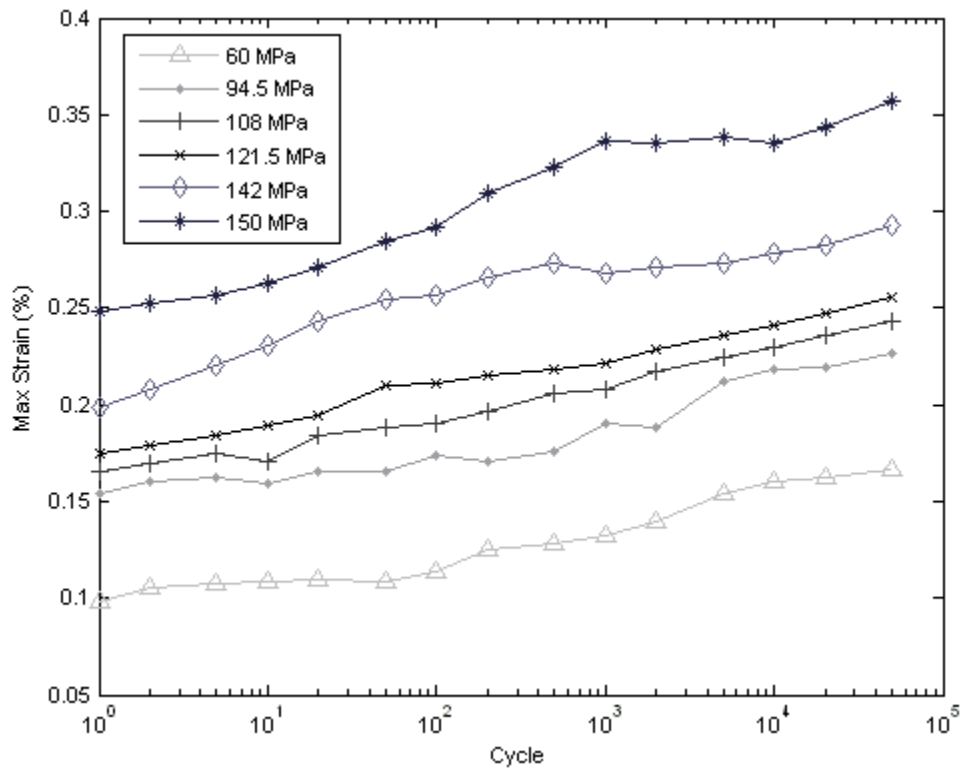


Figure 37. Maximum Strain Increase vs. Cycles

Figure 37 shows the maximum strain from each hysteresis cycle plotted versus the logarithmic cycles. Each specimen shows the increase in strain as the fatigue test progresses, and the slope of each line appears to be similar. The major digressions in the data can be explained by errors in the LVDT output, which can sometimes be inconsistent; or by possible slipping of the specimen in the grips.

The difference in the maximum and minimum strains, or strain range is then calculated over time. The slope of this strain range is an indicator of the fatigue damage accumulated by a specimen. Figure 38 shows the strain range for each fatigue specimen versus the logarithmic cycles.

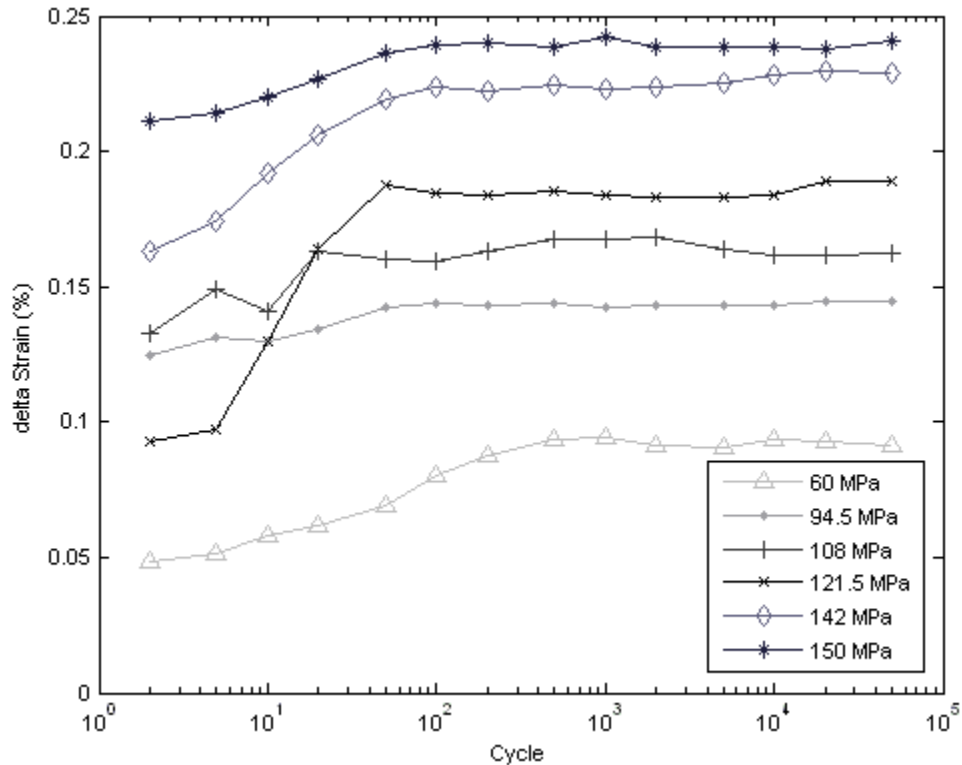


Figure 38. Delta Strain vs. Cycles

As the fatigue test continues, the strain range increases, illustrating some fatigue damage accumulation. Note for most specimens that the greatest change in strain range is early in the fatigue testing. The slow load control response of the MTS test apparatus may be the cause of this, especially for the large discrepancy in the 121.5 MPa data.

After cycle #50, the increase in strain range becomes much smaller. This suggests that there is little fatigue damage accumulation in the material.

4.5.2 Secant Modulus

The damage seen by a specimen in fatigue loading can also be characterized by the change in the elastic response over time. This is easily accomplished for this material because it exhibited a linear elastic response in fatigue hysteresis. The modulus can be calculated by taking the maximum and minimum stress and strain points as follows:

$$S = \frac{\sigma_{max} - \sigma_{min}}{\varepsilon_{max} - \varepsilon_{min}} \quad (5)$$

Figure 39 shows the secant modulus for each fatigue test plotted against the logarithmic fatigue cycles. The initial secant modulus for each fatigue specimen ranges from 58 to 64 GPa.

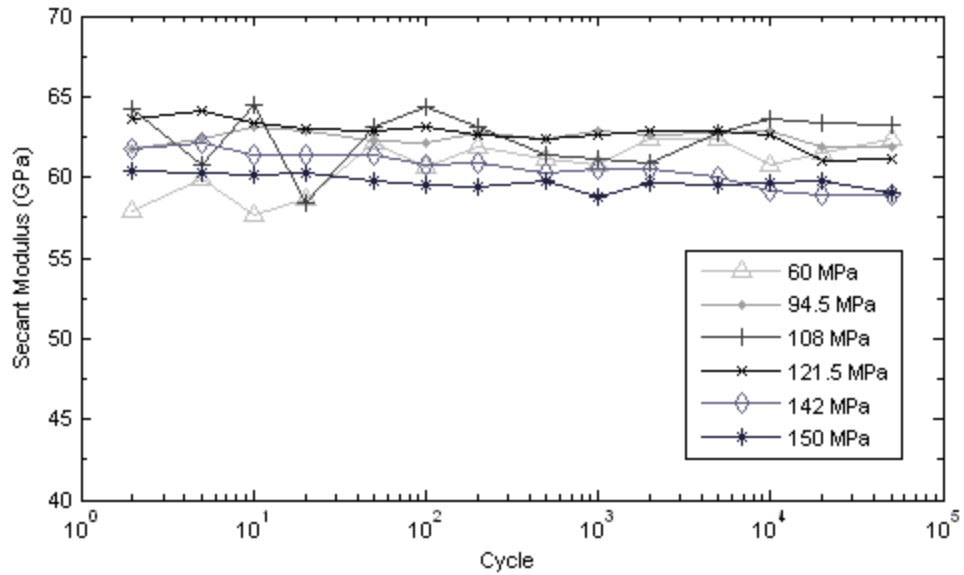


Figure 39. Secant Modulus vs. Cycle

The secant modulus can be normalized by dividing the modulus values by the modulus of the first cycle (S_0). This illustrates the change in modulus over time. Figure 40 shows the normalized modulus for all of the fatigue tests versus the logarithmic of the cycles.

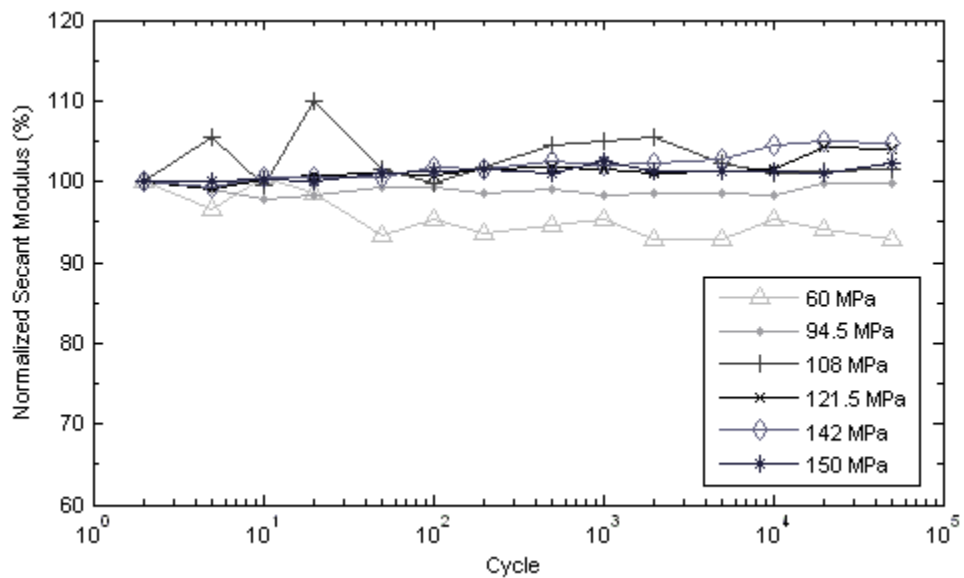


Figure 40. Normalized Secant Modulus vs. Cycle

The secant modulus changes very little over the course of the fatigue test, staying within 10 percent of the modulus of the initial cycle. The maximum increase is 4.8% in the 142 MPa specimen, while the maximum decrease is 7.3% in the 60 MPa specimen. The minimal change in the modulus of the specimens further substantiates that there is little fatigue damage accumulation exhibited in the specimens tested in the combustion environment.

4.6 Residual Strength Test

To see what retained strength is present in the material after fatigue testing, the 142 MPa and 150 MPa specimens were monotonically tensile tested. Figure 41 shows the stress-strain curves of the residual strength testing.

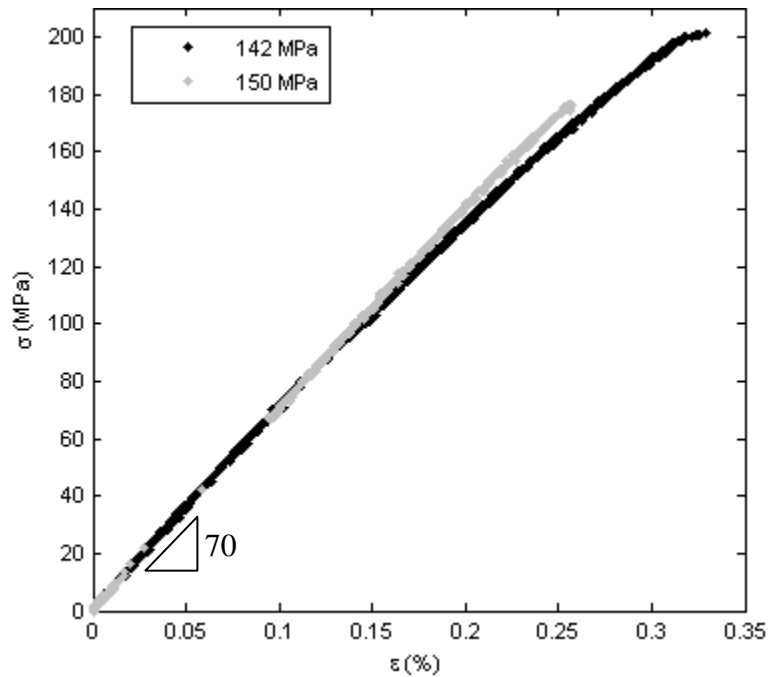


Figure 41. Residual Strength Stress-Strain Curves

The 150 MPa fatigue specimen failed at the grips during residual strength testing. The grip pressure used was initially too high, and the specimen subsequently broke within just outside of the tabbed area. Table 14 shows the results of the residual strength testing.

Table 14. Residual Strength Testing Results

Specimen Number	Fatigue Stress (MPa)	Elastic Modulus (GPa)	Ultimate Tensile Strength (MPa)	Failure Strain %
8	142	70.3	201	.33
10	150	70.7	176	.26

Compared to the tensile test data in Table 12, the fatigue testing caused a 7.5% decrease in the elastic modulus, well within the standard deviation of the tabulated modulus values for N720/A. A negligible decrease in retained tensile strength is also noted. The fatigue regime while in the combustion environment appears to have caused little material property degradation.

4.7 Microstructural Analysis

At the conclusion of the fatigue and tensile tests, all of the specimens were examined using the optical microscope. The optical microscope was used to view the overall area of the specimen exposed to the flame to determine if there was any damage to the material. The SEM was used to view the fiber-matrix interface and the fracture surface. The reference to the front of a specimen signifies the flame exposed side, which was kept constant throughout the testing.

4.7.1 Pretest and Posttest Specimen Comparison

Figure 42 to Figure 44 show the dogbone surface before and after the fatigue testing for specimens 6 – 8; with the pretest photos on the left and, the posttest photos on the right. The blurred spots on the pretest specimens are from un-removed adhesive that held the protective Plexiglas plate on the panel. Matrix cracks on some of the specimens have been circled for reference and comparison.

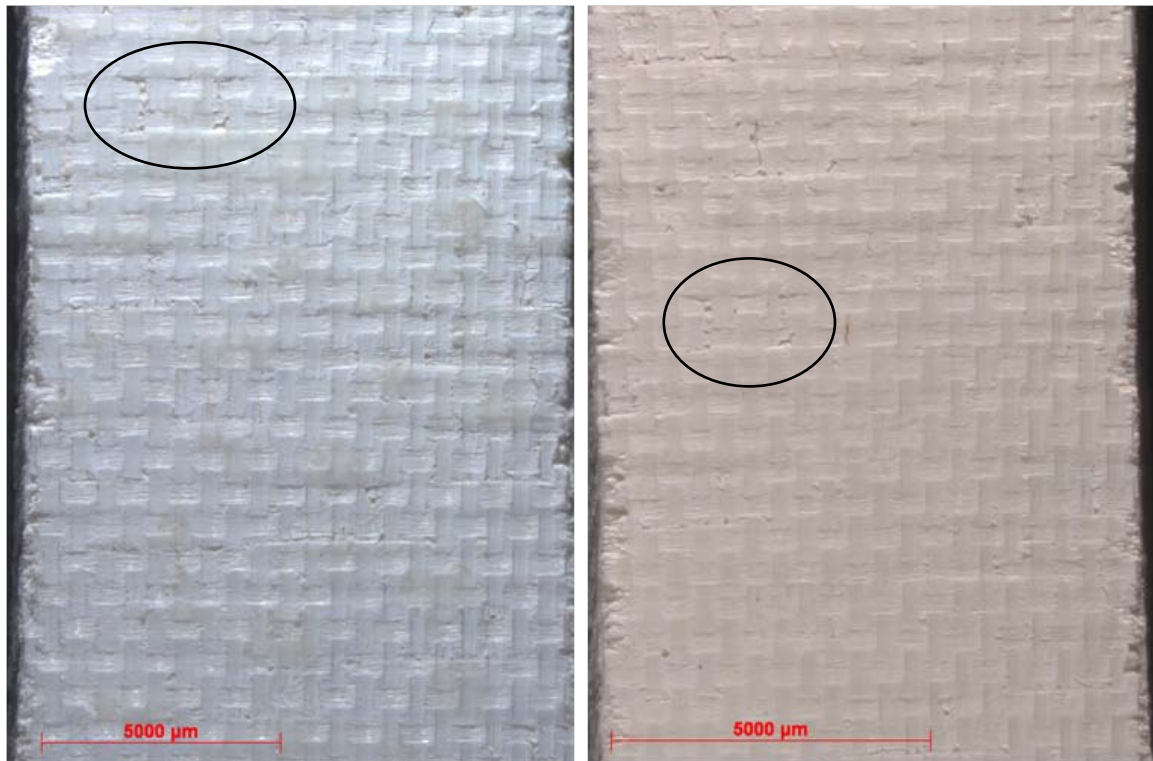


Figure 42. 108 MPa Specimen Pre and Post Test (Flame Side)

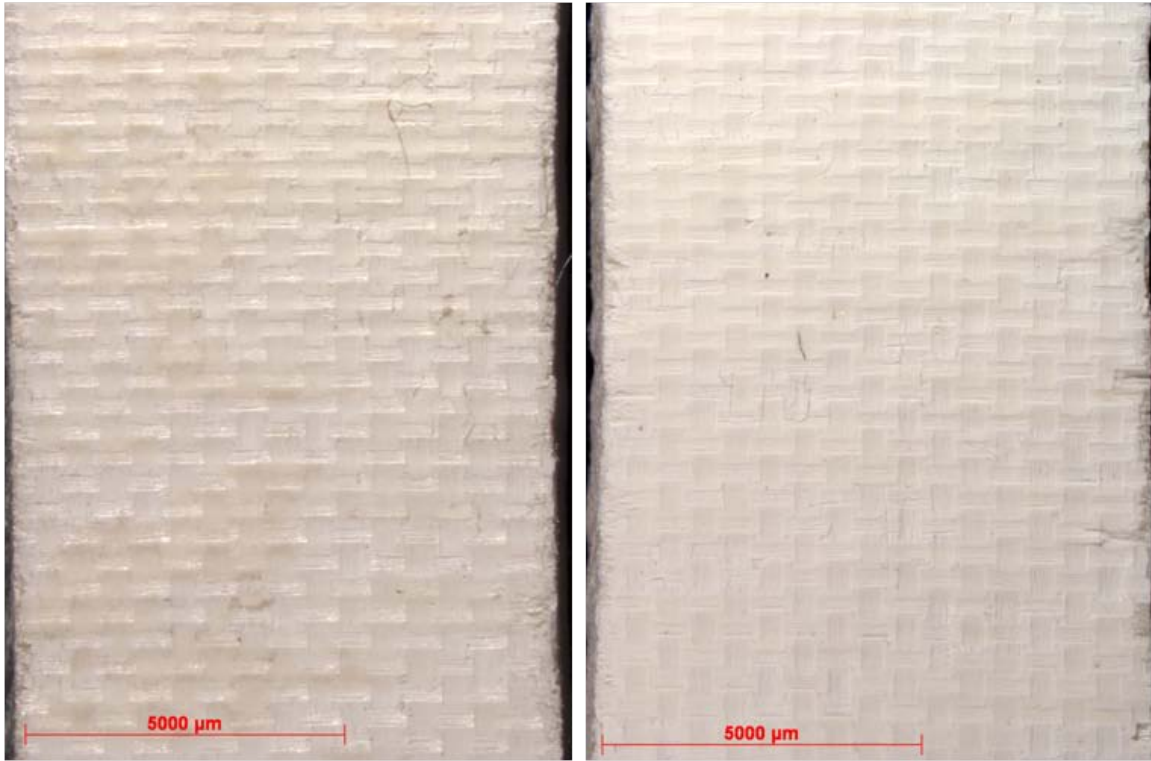


Figure 43. 121.5 MPa Specimen Pre and Post Test (Flame Side)

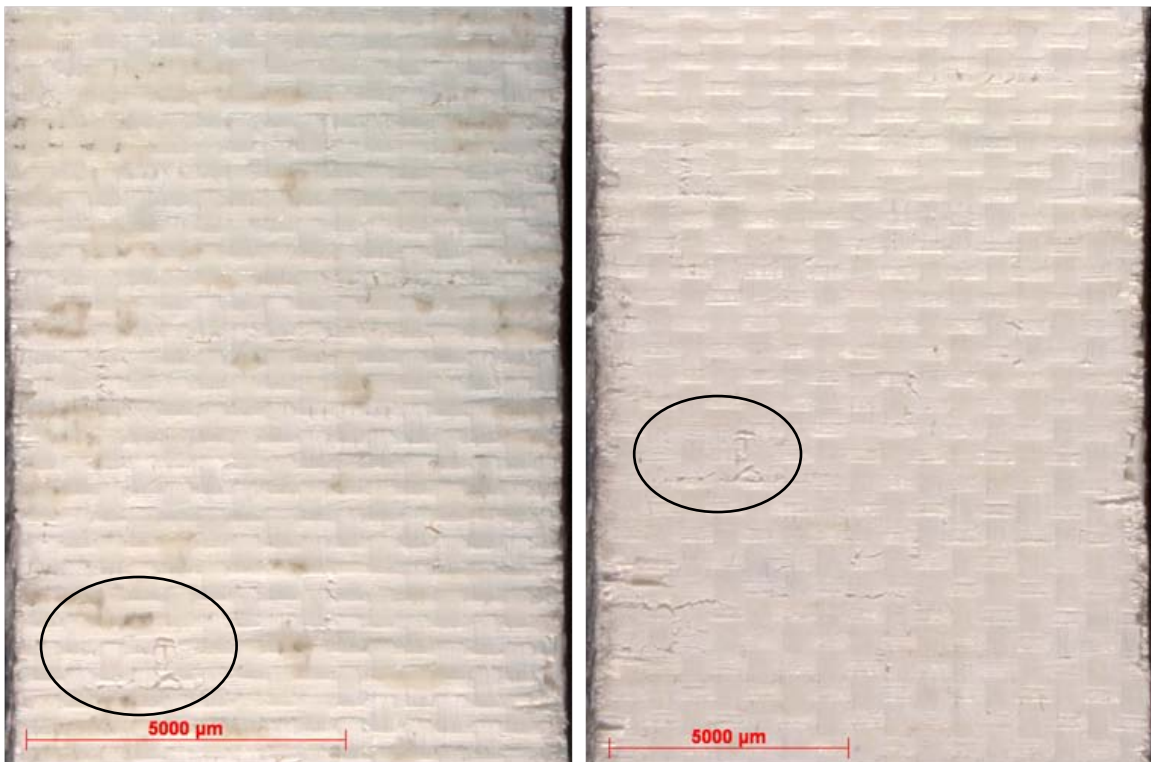
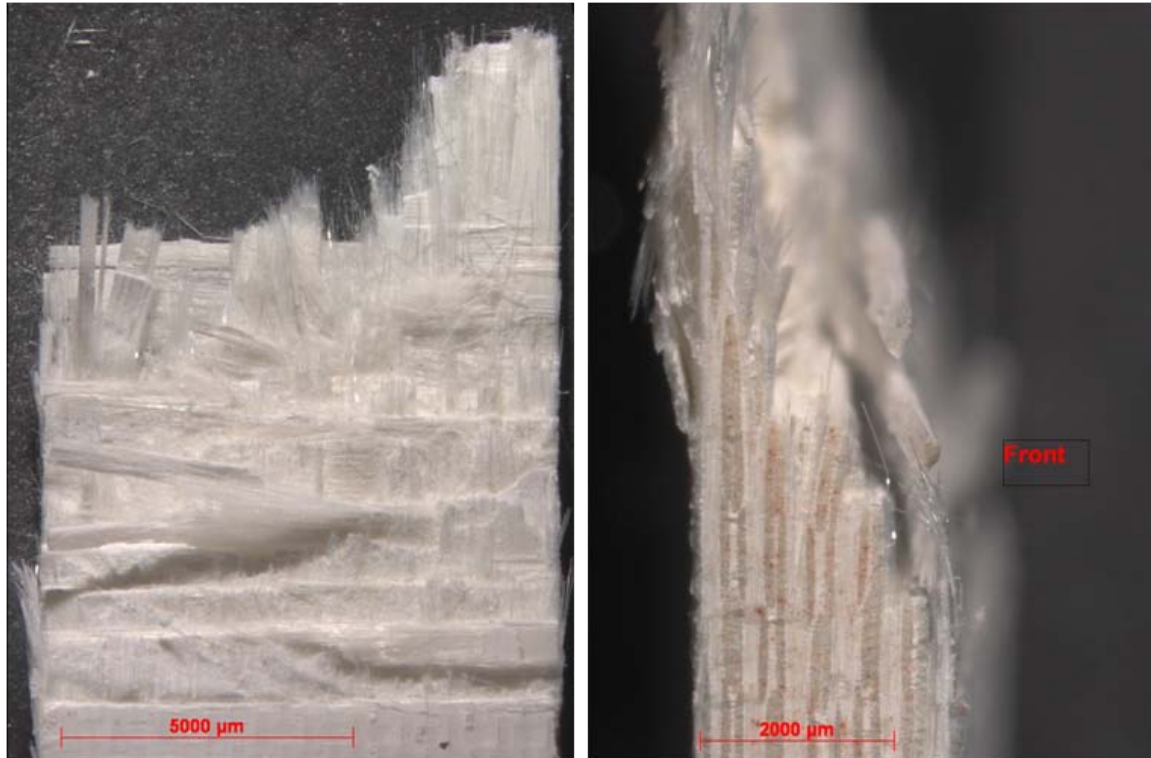


Figure 44. 142 MPa Specimen Pre and Post Test (Flame Side)

The pretest and posttest photos reveal that the matrix cracks originally present in the material do not expand as the specimens are subjected to the fatigue and combustion. There is also no appreciable marking on the specimens to suggest that they were exposed to a flame.

4.7.2 Monotonic Testing Fracture Surfaces

Figure 45 shows the front view of the tensile strength test specimen fracture surface. The specimen was only inspected with the optical microscope. Before the specimen could be removed after the test, the power to the MTS computer was cut off. This caused the crosshead to come back down onto the other half of the specimen, damaging the fracture surface. Fortunately, the general profile of the fracture surface was maintained.



**Figure 45. Tensile Strength Specimen Fracture Surface
(Flame side labeled as “Front”)**

The fracture of the specimen exposed to the combustion environment while monotonically tested follows a unique path compared to previous tensile tests. Through the thickness of the specimen, the fracture goes in a diagonal fashion. This suggests that the thermal gradient of the flame on the specimen may play a part in its failure mechanism.

Figure 46 shows the front and side view of the residual strength test fracture surface on the 142 MPa specimen. The fracture surface follows a similar pattern to the tensile specimen fracture.

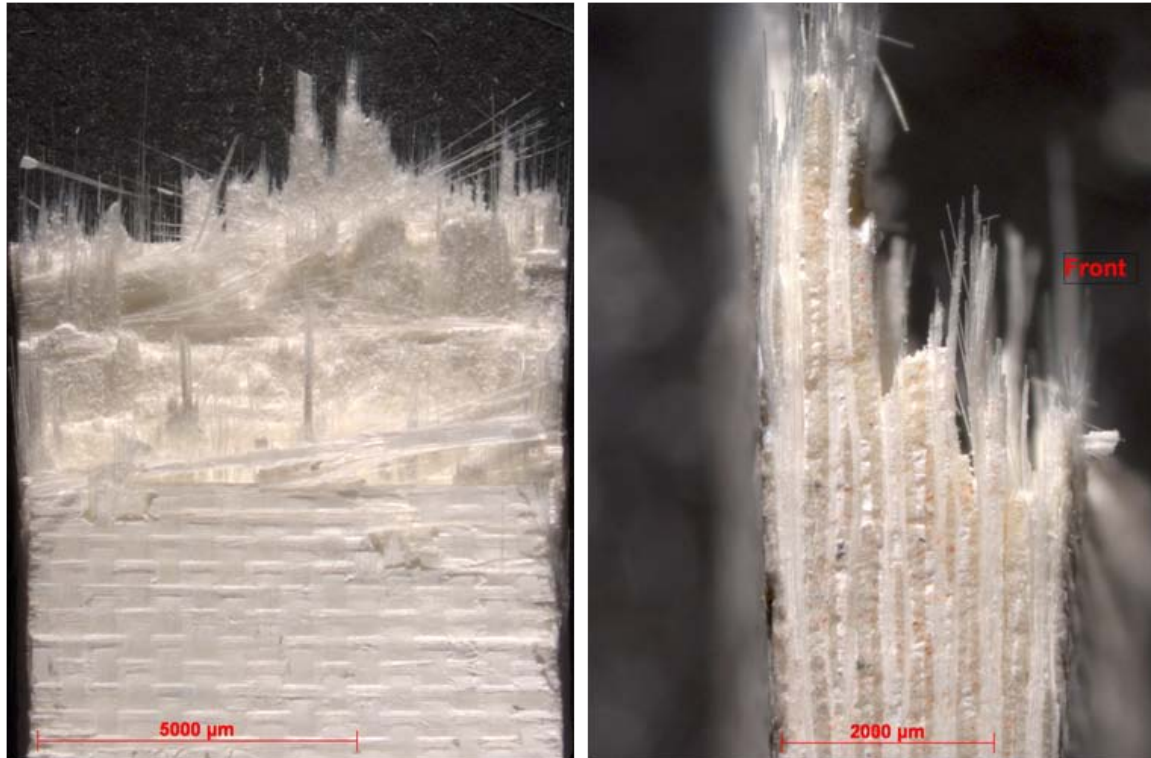


**Figure 46. 142 MPa Specimen Residual Strength Fracture
(Flame Side Labeled as “Front”)**

4.7.3 Scanning Electron Microscope Efforts

SEM work was completed on a three pieces of material. The first piece was a portion of leftover panel after specimens were cut from it. The second and third pieces were from the 142 MPa specimen. One focused on the fracture surface, and the other focused on the effects of the combustion environment on the internal structure of the specimen.

Figure 47 to Figure 49 show the internal structure of the pristine sample. The surface was slightly polished with fine-grit sandpaper after cutting. Boxes outline areas of interest that were subsequently focused on.



Figure 47. Pristine Specimen Overall Interior Structure

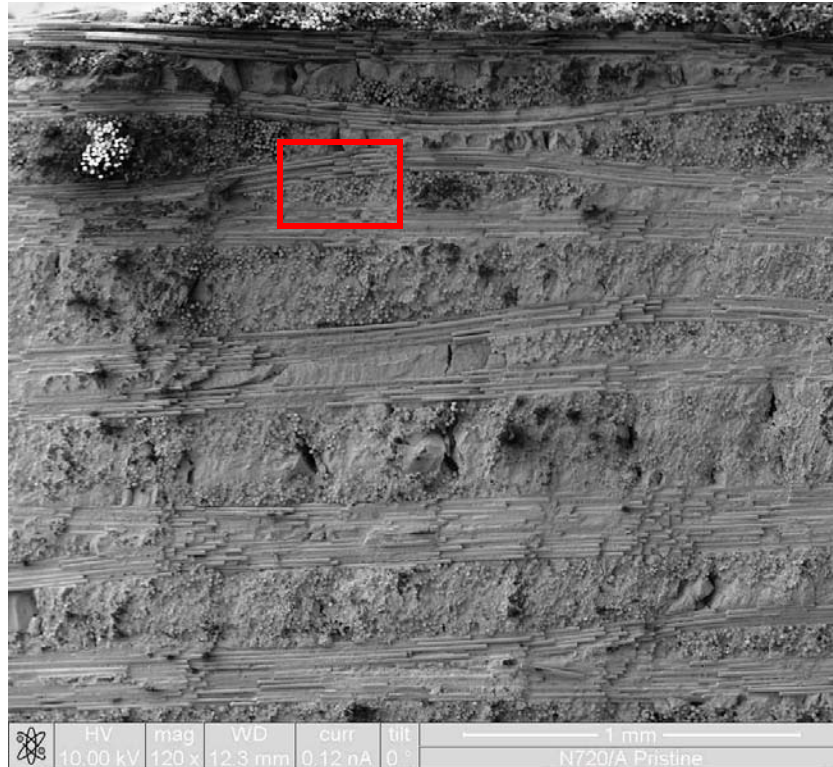


Figure 48. Pristine Specimen Matrix Crack

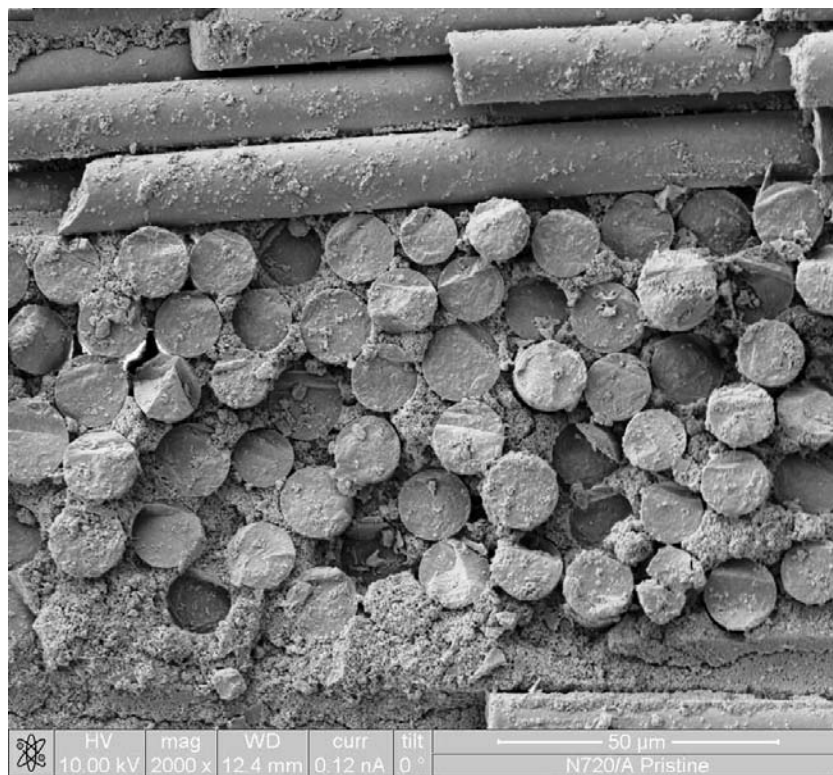
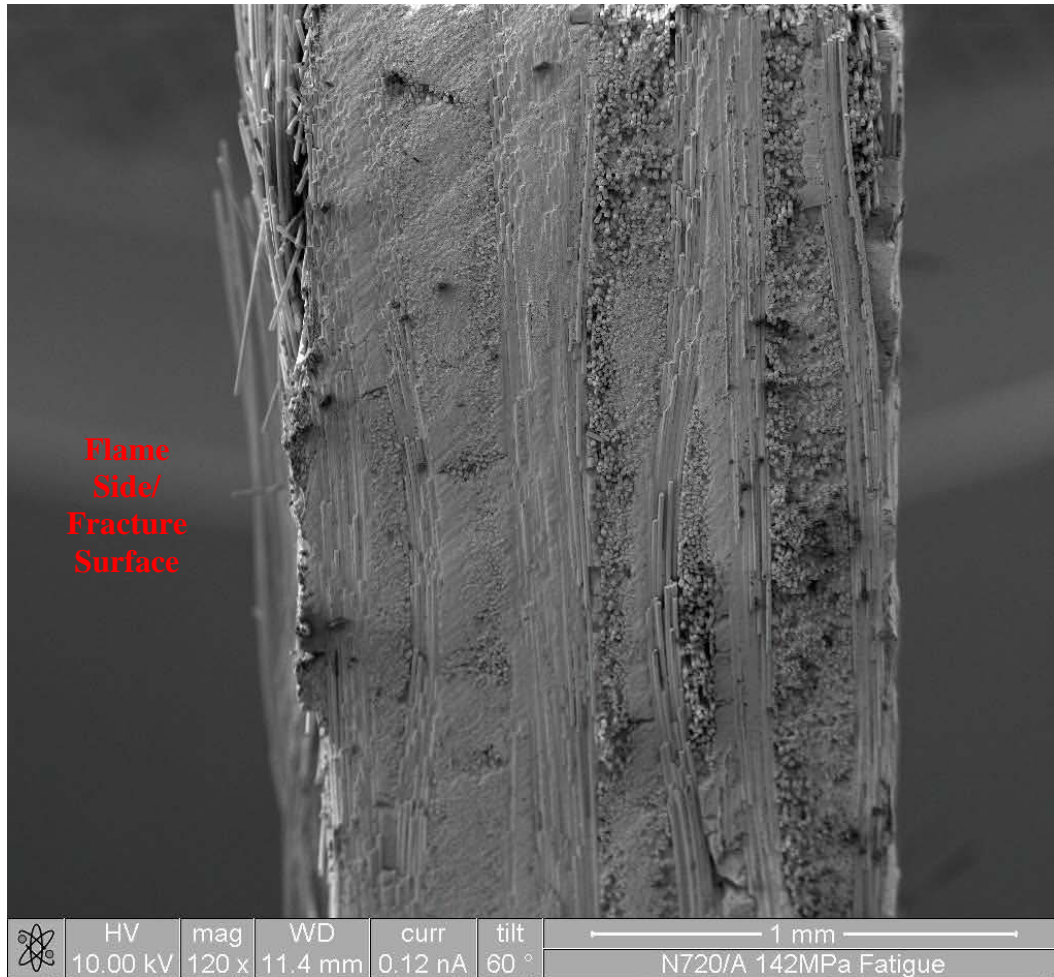


Figure 49. Pristine Specimen Fiber-Matrix Interface

There is matrix cracking through the interior of the composite. Figure 49 shows the fiber and matrix interface. The porous matrix interface is apparent in lower portion of the figure. Some residual matrix residue is also noticeable on the fibers in the upper region of the figure.

The upper segment of the 142 MPa specimen was used to study the internal structure of the fiber-matrix interface after the combustion testing. The specimen was cut as close as possible to the end of the fracture surface, and the cut area was lightly sanded. Figure 50 shows the overall view of the internal area of the specimen.



**Figure 50. Internal Structure of Fracture Specimen
(Flame Side at Left)**

At first glance, it appears that the fiber-matrix interface is smoother at the front of the specimen, and gets rougher as you go aft (left to right in figure). Higher magnification photos were taken approximately 1 mm down from the side edge of the specimen (top of Figure 50). The regions of interest were in the flame side, middle, and rear areas (going from left to right in Figure 50) of the specimen. Figure 51 to Figure 53 show the fiber-matrix interface in these regions. The flame side is towards the left side of the micrographs.

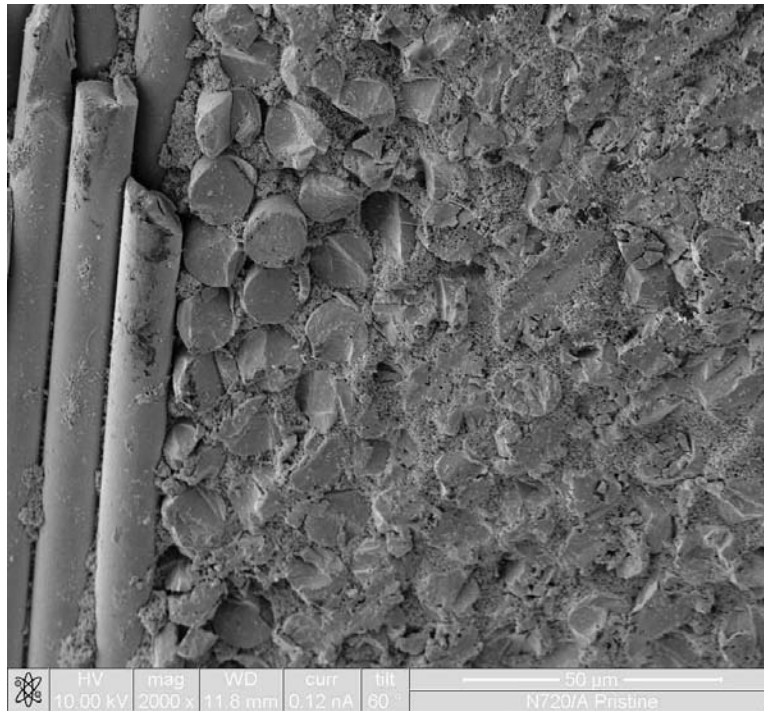


Figure 51. Internal Surface (Flame Side)

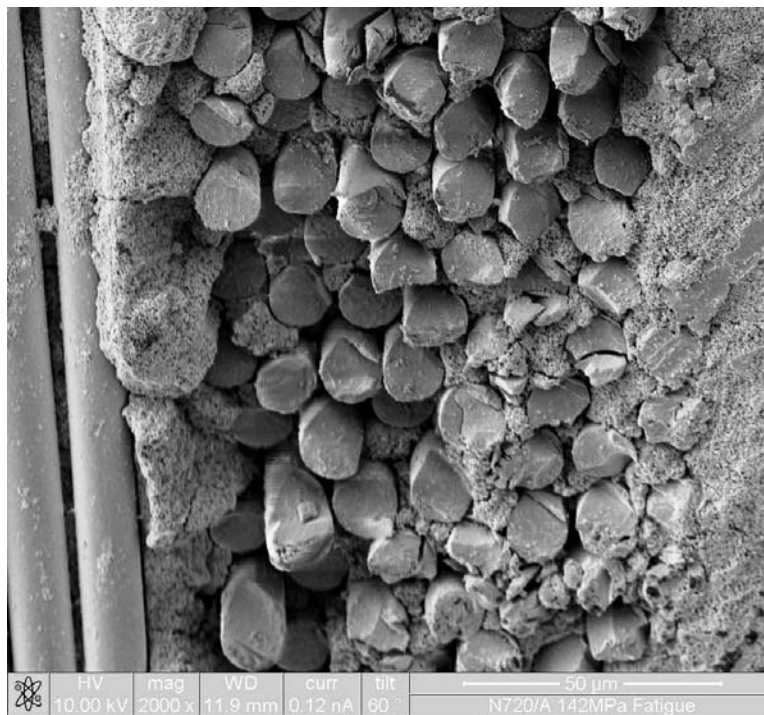


Figure 52. Internal Surface (Middle)

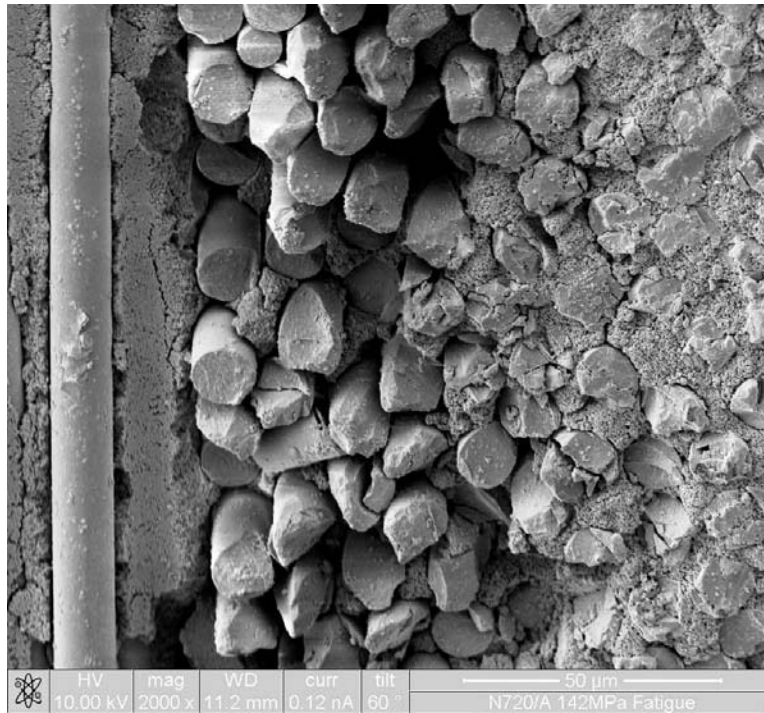


Figure 53. Internal Surface (Rear)

From the higher magnification micrographs, it appears that the matrix porosity is the same in the front as it is in the rear of the specimen. No densification of the matrix is apparent due to the combustion environment. Comparing these micrographs to the pristine specimens at the same 2000x magnification in Figure 49, the matrix porosity and appearance look similar.

The bottom portion of the 142 MPa specimen was used to study the fracture surface. Figure 54 and Figure 55 show the SEM images of the total fracture surface.

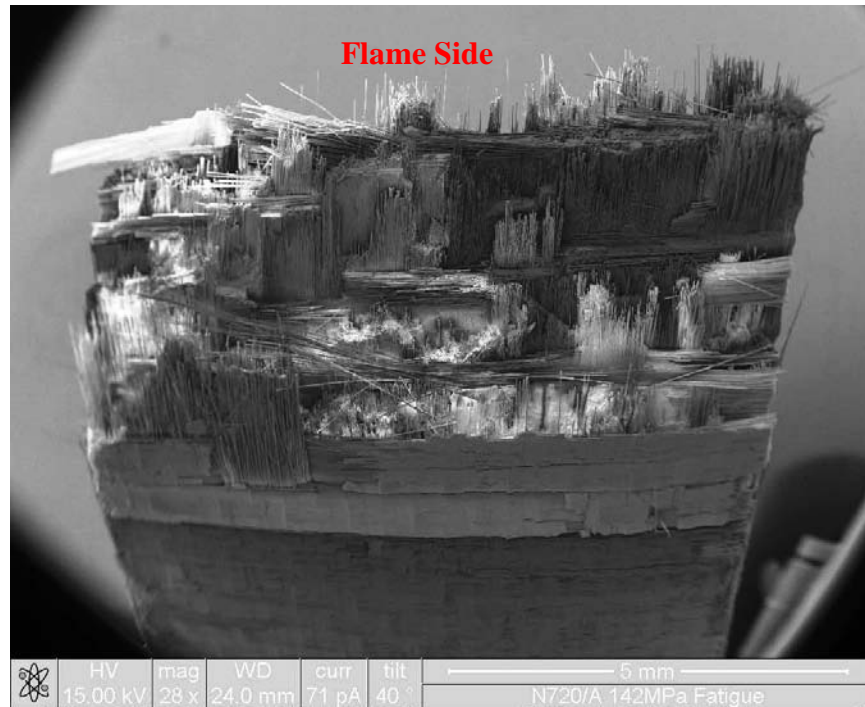


Figure 54. 142 MPa Fracture Surface (Rear Looking Towards Flame Side)

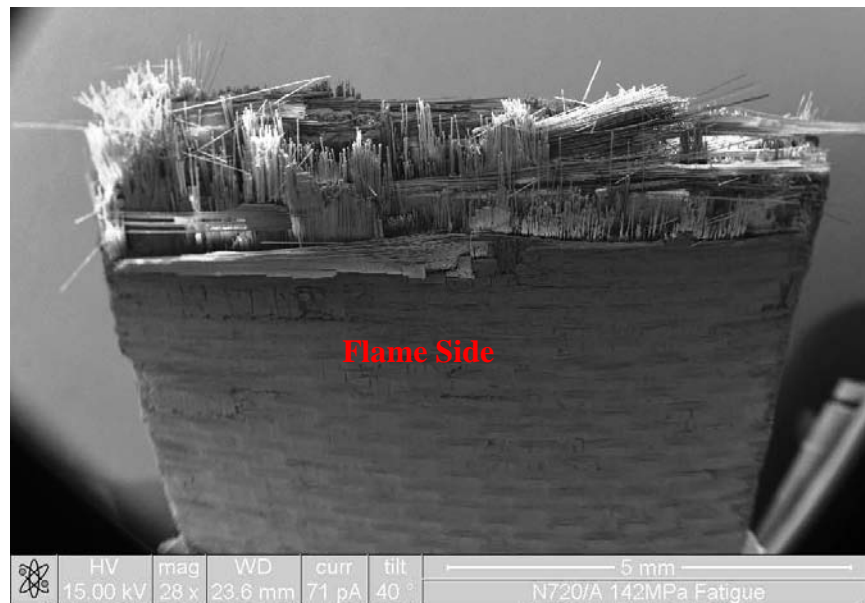


Figure 55. 142 MPa Fracture Surface (Flame Side Looking Towards Rear)

Fracture surface imaging was focused in two general areas; the front (flame side) and rear. This was to aid in distinguishing any differences within the fiber-matrix

interface due to the combustion environment. A comparison of the fiber-matrix interface on 0° fibers bundles at the edges of the specimen was performed. Figure 56 and Figure 57 show these fiber bundles at the fracture surface edges.

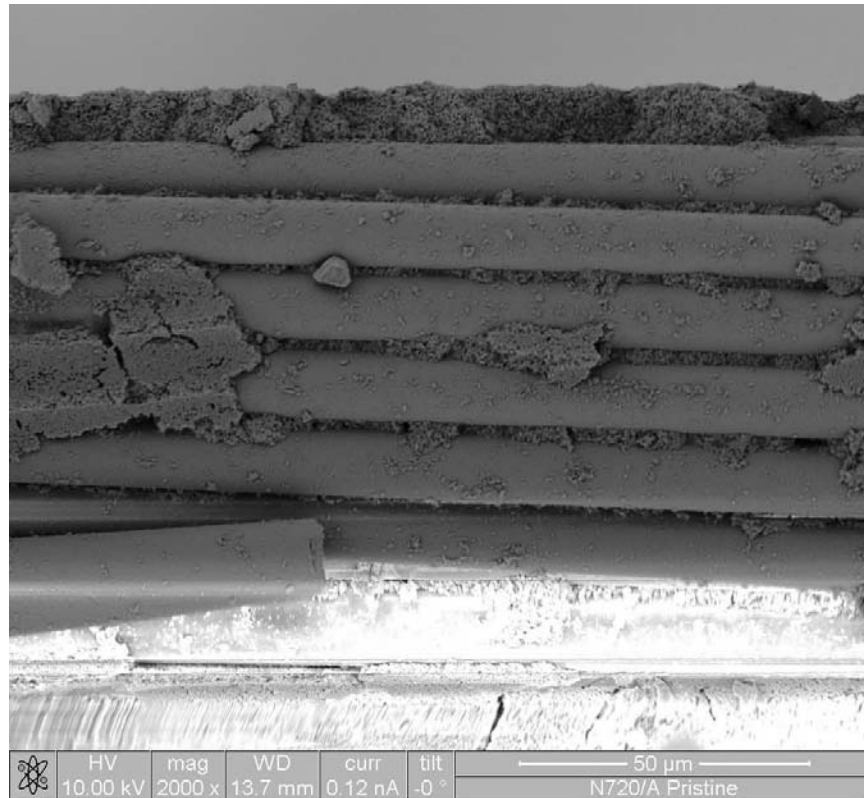


Figure 56. Flame Side 0° Fiber Bundle (Flame Side Edge at Top)

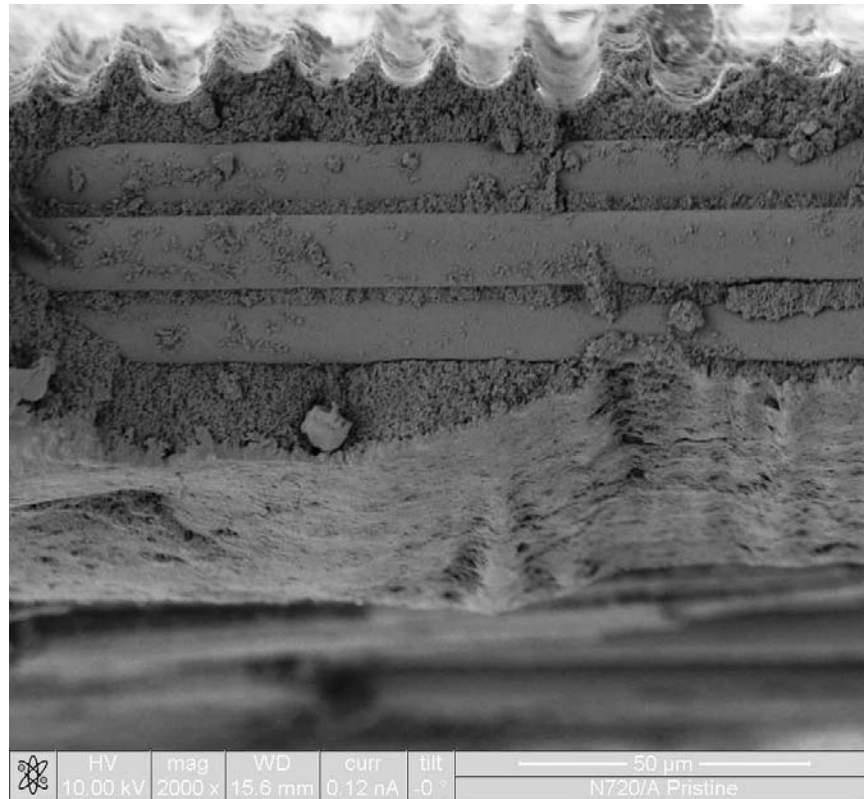


Figure 57. Rear Side 0° Fiber Bundle (Rear Edge at Bottom)

The matrix porosity and interface between the fibers looks similar on both the flame side and rear fracture surfaces of the specimen. This shows that the specimen fracture on the edges in the 0° fiber direction was similar, and the combustion environment did not affect the interface. Figure 58 to Figure 65 show the front fracture surface details.



Figure 58. Front Right Edge Fracture Surface (Flame Side at Top)

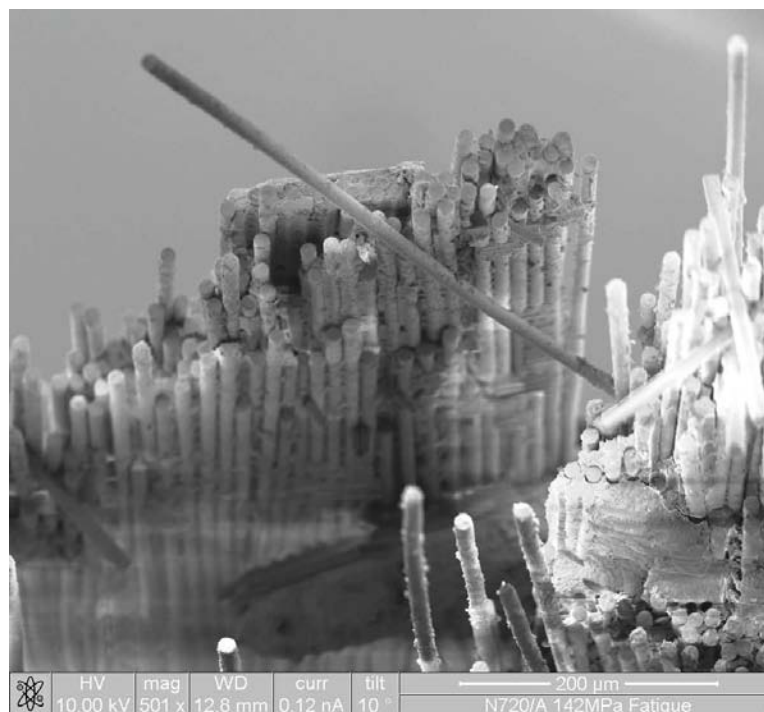


Figure 59. Front Right Edge Box 1 90° Fiber Bundle

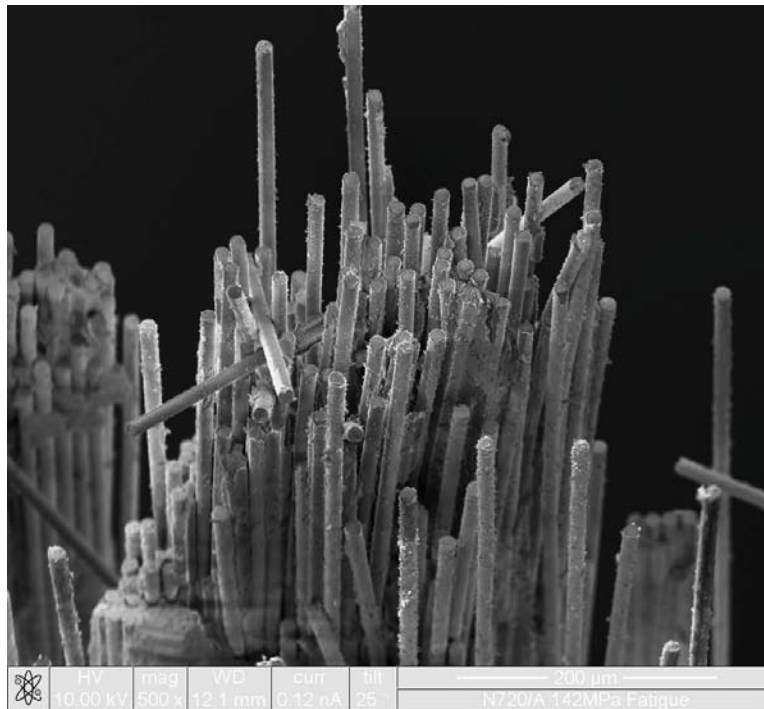


Figure 60. Front Right Edge Box 2 90° Fiber Bundle

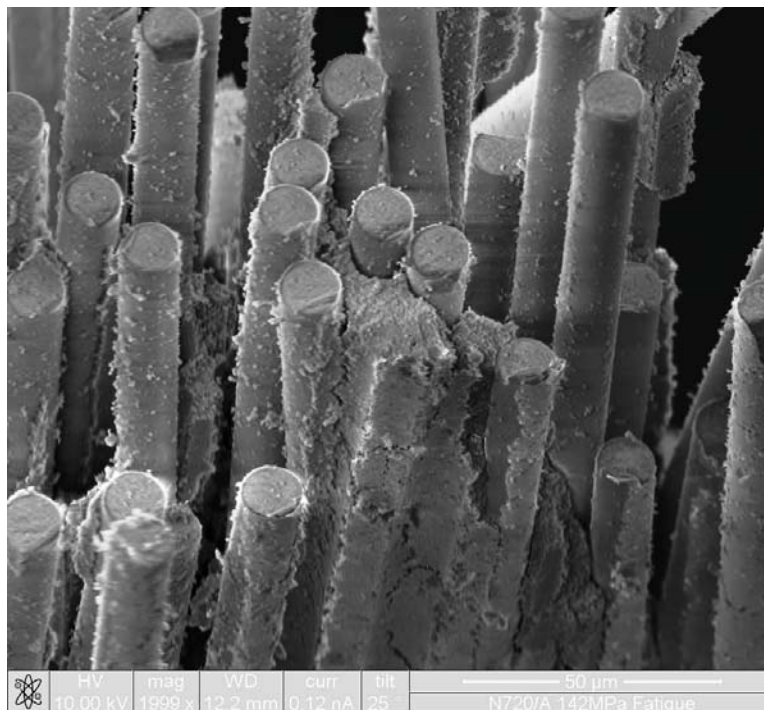


Figure 61. Front Right Edge Box 2 Fibers with Matrix



Figure 62. Front Left Edge Fracture Surface (Flame Side at Top)

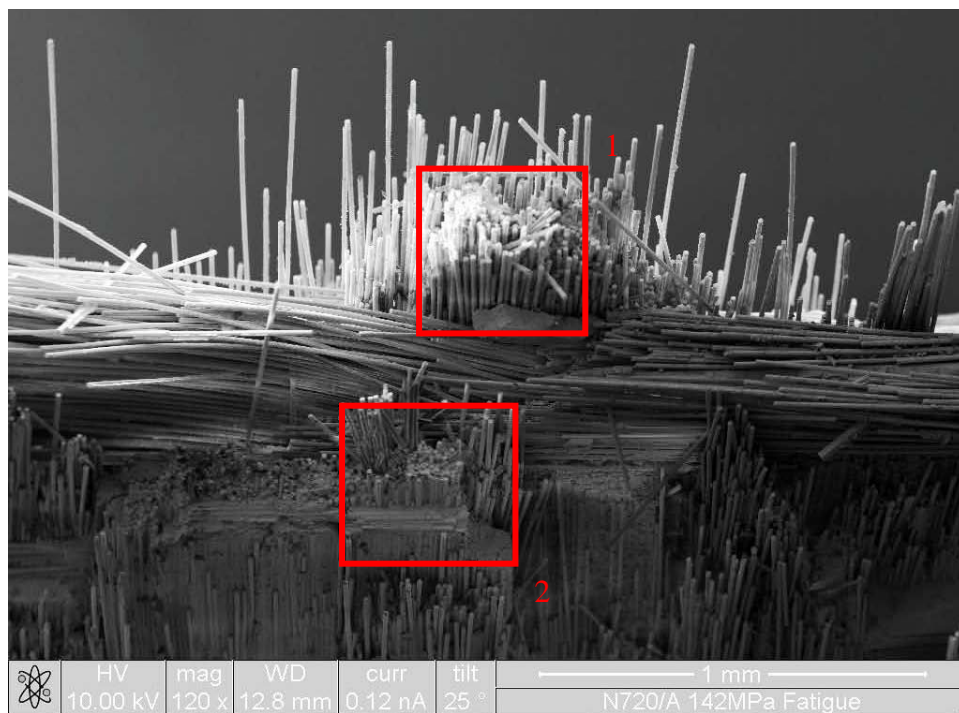


Figure 63. Front Left Edge 90° Fiber Bundles (Flame Side at Top)

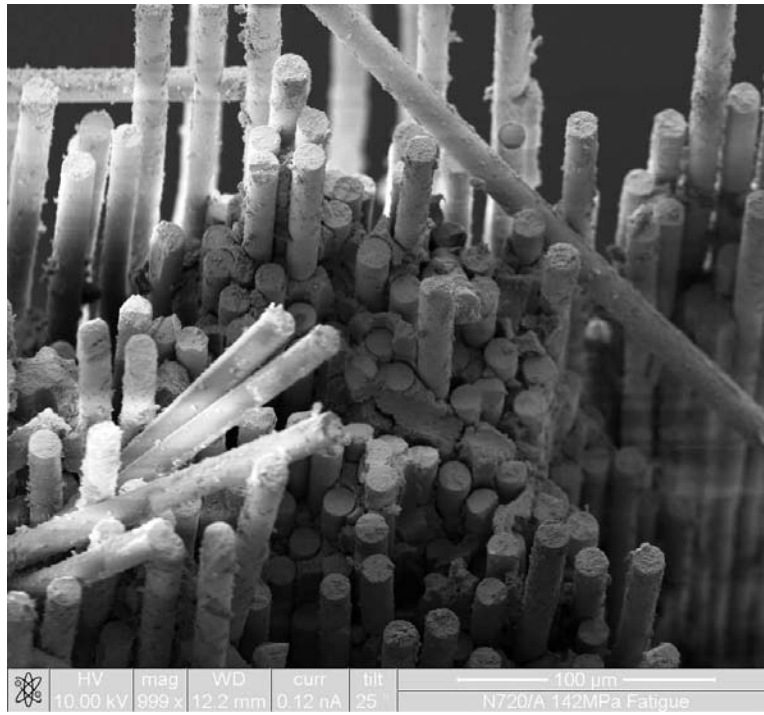


Figure 64. Front Left Edge Box 1 Fiber-Matrix Interface

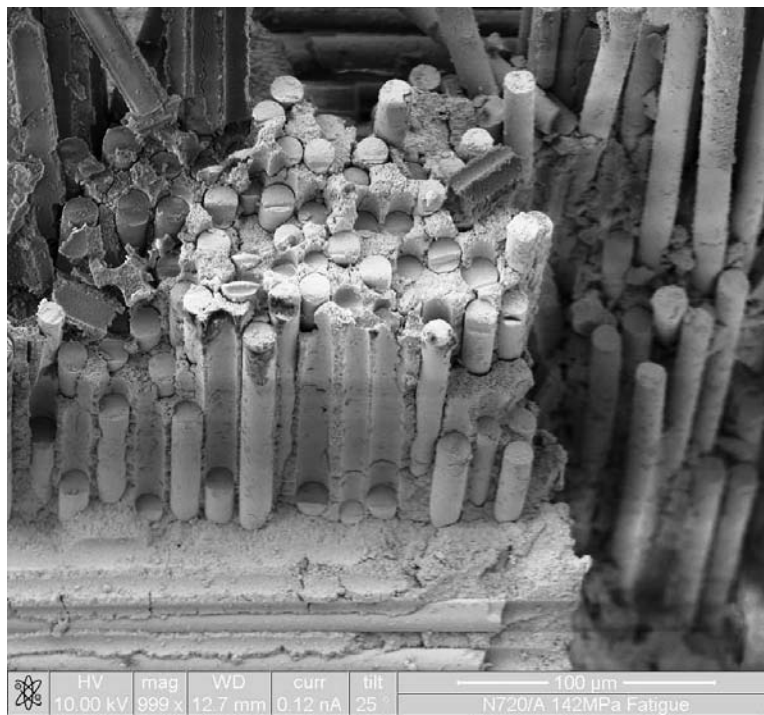


Figure 65. Front Left Edge Box 2 Fiber-Matrix Interface

With the exception of the fiber bundle shown in Figure 59, there is a great deal of fiber pullout along the front edge of the fracture surface. There is also little matrix present between these pullout fiber bundles. Towards the center of the fracture surface, the fiber pullout seems to lessen and the fracture of the fiber bundles is more abrupt. Figure 66 to Figure 69 show the rear fracture surface details.



Figure 66. Rear Right Edge Fracture Surface (Flame Side Towards Top)



Figure 67. Rear Right Edge 90° Fiber Bundle



Figure 68. Rear Left Edge Fracture Surface (Flame Side Towards Top)

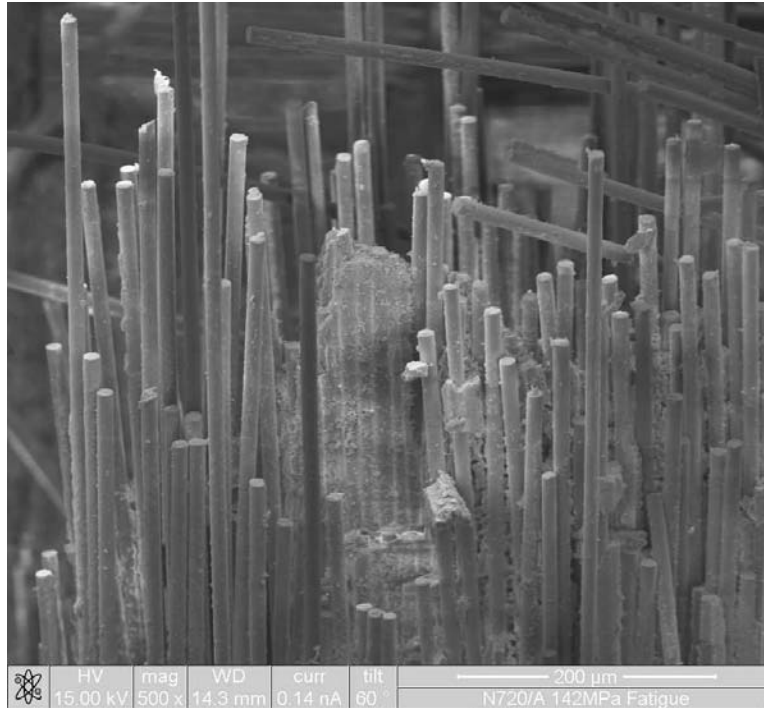


Figure 69. Rear Left Edge 90° Fiber Bundle

The fracture surface on the rear of the specimen follows the same pattern as the front. There are long fiber pullout regions at the rear face, and they get more abrupt towards the center of the fracture.

Single 90° fibers from both the front and rear of the fracture surface were also looked at. This allowed for a comparison of matrix density on the individual fibers. Figure 70 and Figure 71 show the selected fibers.

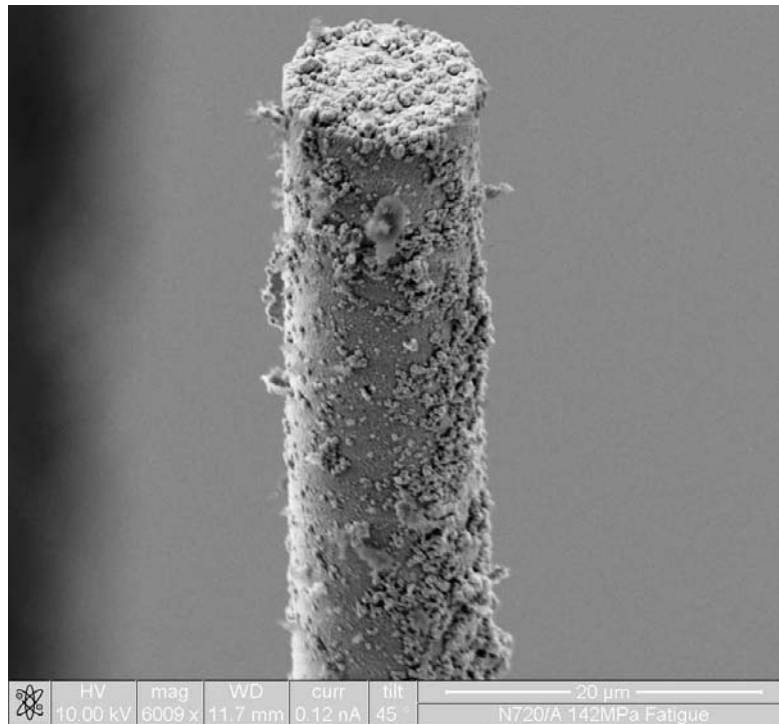


Figure 70. Flame Side Surface 90° Individual Fiber

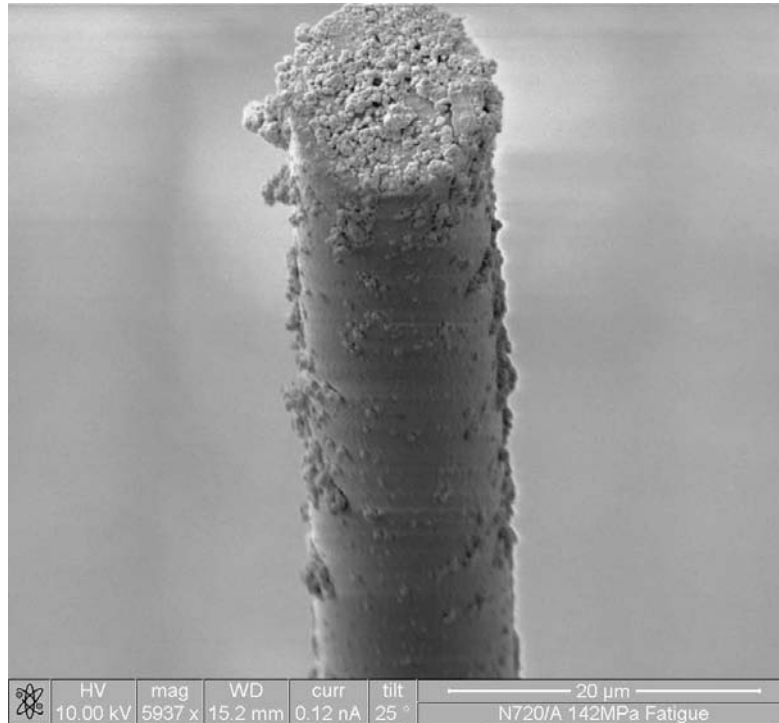


Figure 71. Rear Surface 90° Individual Fiber

A greater amount of matrix material is present on the front fiber. This may be due to the densification of the matrix from the elevated temperatures of the flame.

Comparing the fracture surface details to the SEM micrographs produced by Steel and Eber, there are some similarities. The fiber pullout bundles with minimal matrix are present throughout the thickness of the specimen. There are also regions with abrupt fiber bundle failure within the matrix. The only difference noted is the fracture shape. Their fracture surfaces were nearly flat or symmetrical through the thickness, while the combustion specimens had a diagonally shaped fracture surface.

4.8. Results Summary

Fatigue behavior of N720/A in the combustion environment is very similar to that in the high temperature furnace. The material exhibited a “go/no-go” failure condition such as what was seen in earlier high-temperature fatigue tests. All of the fatigue test specimens survived the 25 hour fatigue test under the combustion environment.

Exposure to the combustion environment while monotonically loading the material caused a 19% decrease in strength relative to previous tensile strength data. The residual strength test on the 85% UTS specimen revealed no loss in tensile strength outside of the combustion environment relative to previous tensile strength data.

The fracture surface from combustion exposure was the only noticeable difference in the testing of this material. The diagonal shape through the thickness of the specimen suggests that there is some interaction of the combustion gasses with fiber-matrix interface.

V. Conclusions and Recommendations

Under a continuous high-velocity flame, the Nextel 720/Alumina ceramic matrix composite performed exceptionally well. The high-velocity propane-oxygen flame heated the mid-section of the specimens to approximately 1200°C. After 25 hours of exposure, the material showed no surface degradation from the combustion environment.

A monotonic test in the combustion environment showed a tensile strength of 167 MPa with an elastic modulus of 62 GPa. This 19% decrease in tensile strength and modulus relative to previous tensile strength data in laboratory air may indicate sensitivity to the temperature gradient present from the non-isothermal flame environment. The forces exerted from the flame itself may also be a factor in the decrease in tensile strength. Prior combustor rig testing of the same material further validates the material property decreases.

Tension-tension fatigue loading in the combustion environment showed good fatigue resistance of N720/A. All of the fatigue specimens exceeded 90,000 cycles at 1Hz with a stress ratio of 5% when the maximum fatigue stress was kept below 150 MPa, or 90% UTS. Strain accumulation over fatigue testing was minimal. The maximum strain seen in the 90% UTS fatigue test was 0.357%, below the monotonic test failure strain of 0.41%. Small changes in the delta of the cycle strain and the very small change in elastic modulus through the fatigue testing further validates this materials excellent fatigue resistance. Residual strength testing of a fatigue specimen at room temperature also revealed a retained strength of 201 MPa. This represents little degradation of the

material properties from the fatigue/combustion test. Micrographs of pristine and combustion tested specimens revealed no differences in the fiber-matrix interface. Matrix porosity through the combustion specimen thickness appeared the same, showing that the combustion environment did not damage the interface. The appearance of the combustion tested fracture surface was similar to furnace testing experience. Fiber pullouts were prevalent through the specimen, suggesting no decrease in porosity of the matrix from the combustion heating. However, the shape of the fracture surface in the combustion testing was different than in furnace testing. Through the thickness of the combustion specimens, the fracture propagated in a diagonal fashion, versus the relatively flat fracture surface seen in previous furnace tested specimens. This suggests that the flame causes localized strengthening at the material surface. This strengthening causes the failure of the CMC to occur just outside of where the flame hits the specimen. Since the specimen dogbone shape was a gradual radius, the rest of the fracture of the specimen occurs in a diagonal fashion at the smallest net section area.

This testing demonstrated that Nextel 720/Alumina can perform reliably under a fatigue load in the combustion environment. Future test efforts could include longer fatigue testing in the combustion environment, especially given that fatigue testing in a furnace was performed up to 500,000 cycles. Longer combustion excursions could reveal more information on how the material reacts to the environment. Creep testing and notch sensitivity testing can also be performed in this combustion test platform. Comparing these tests to previous 1200°C furnace work would create good database of N720/A material properties in the combustion environment.

Appendix

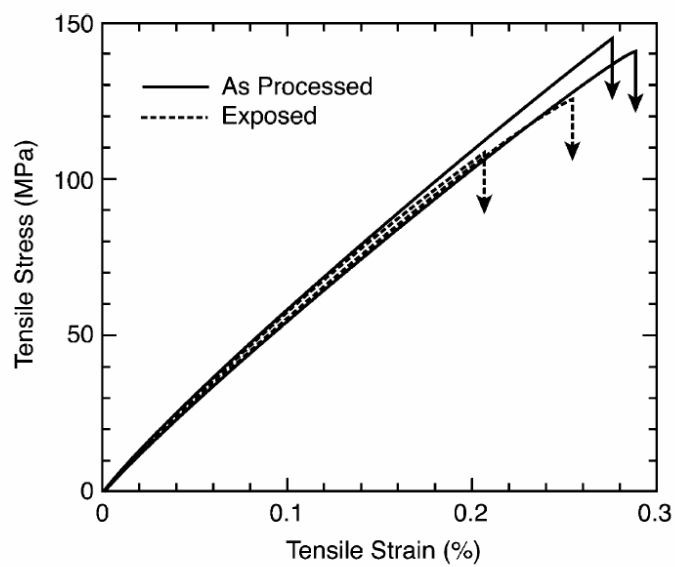


Figure 72. Stress Strain of Unexposed and Combustion Exposed CMC [13]

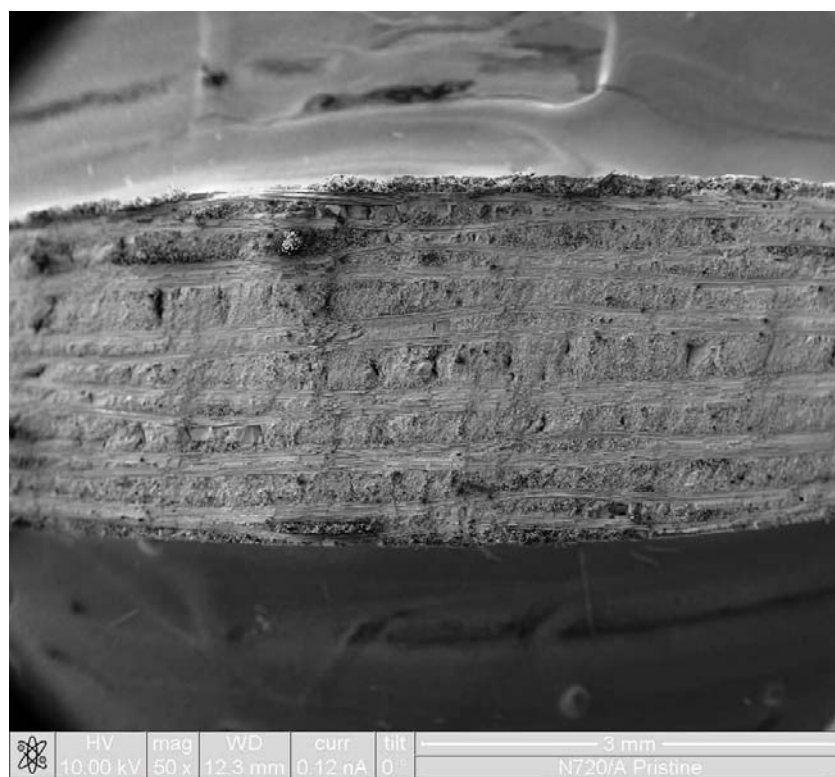


Figure 73. Pristine Surface, 50x

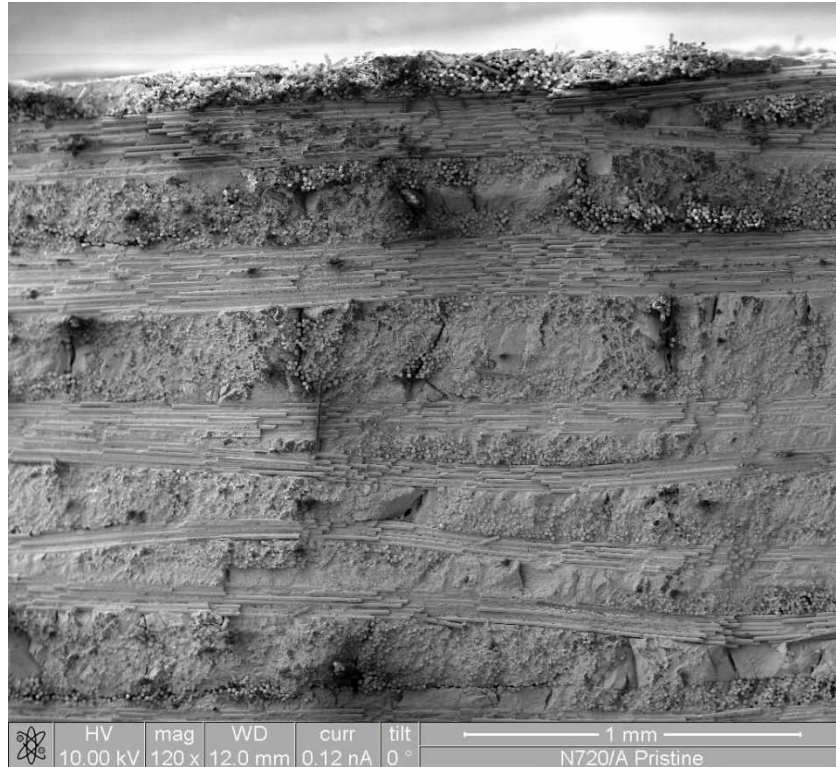


Figure 74. Pristine Surface, 120x

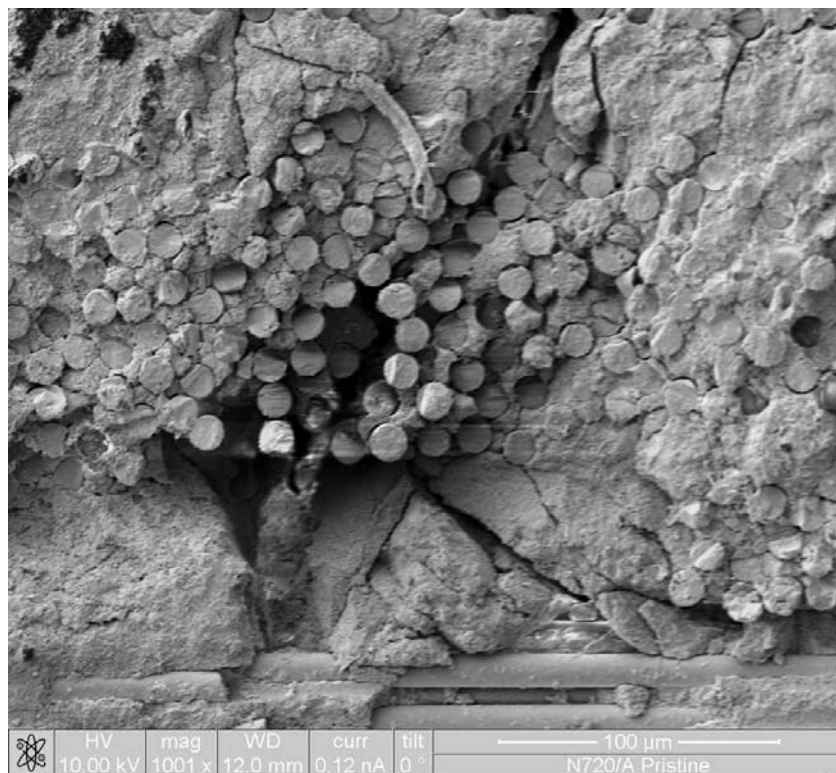


Figure 75. Pristine Surface Fibers, 1001x

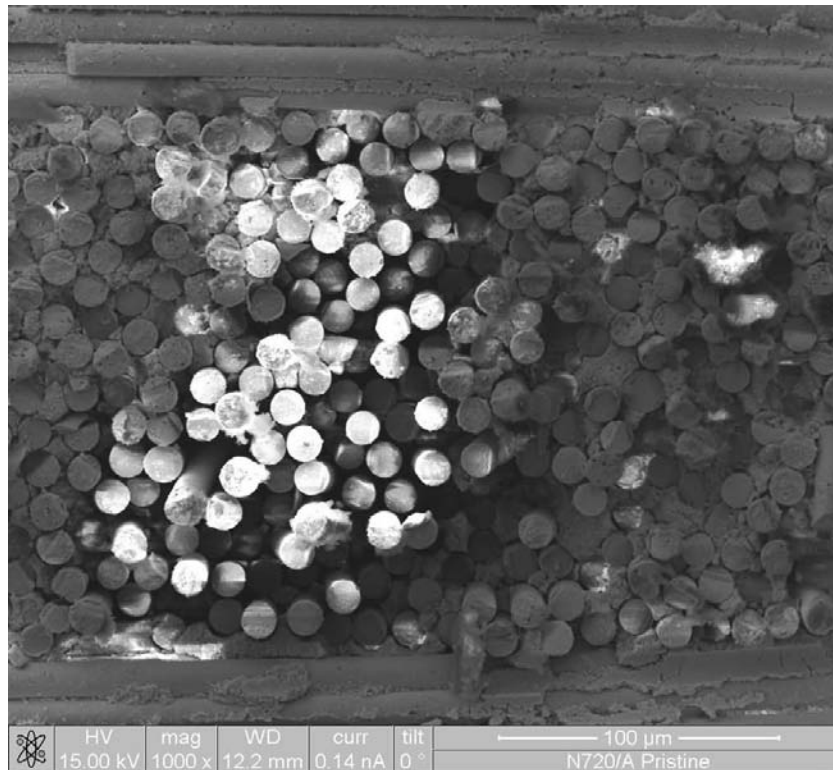


Figure 76. Pristine Surface Fibers, 1000x

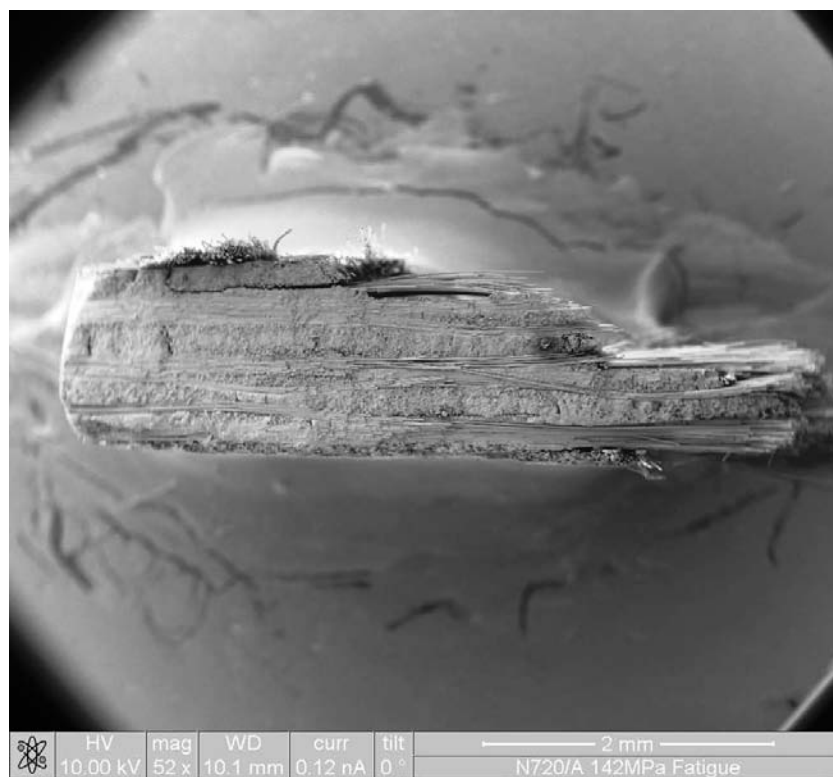


Figure 77. 142 MPa Fracture Side View, 52x

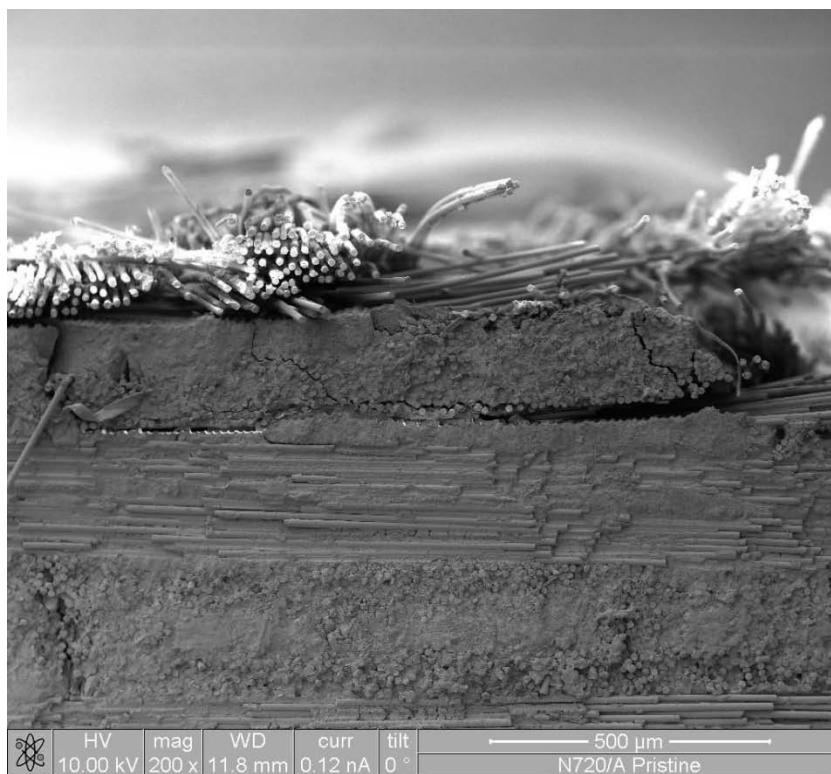


Figure 78. 142 MPa Side Fracture Front Cracking, 200x

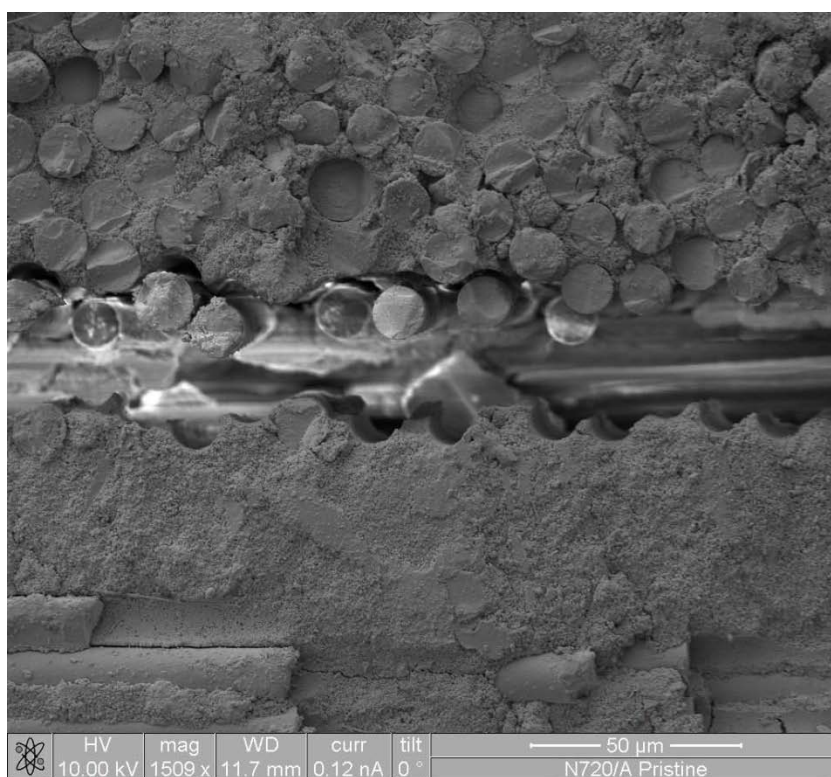


Figure 79. 142 MPa Side Fracture Front Cracking, 1509x

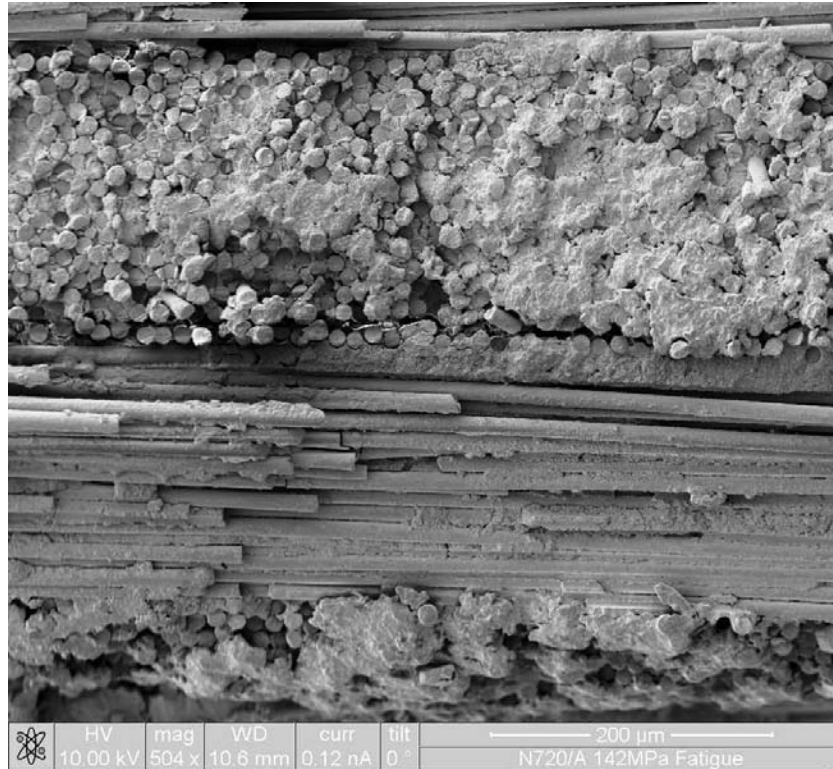


Figure 80. 142 MPa Side Fracture Back Fiber-Matrix, 504x

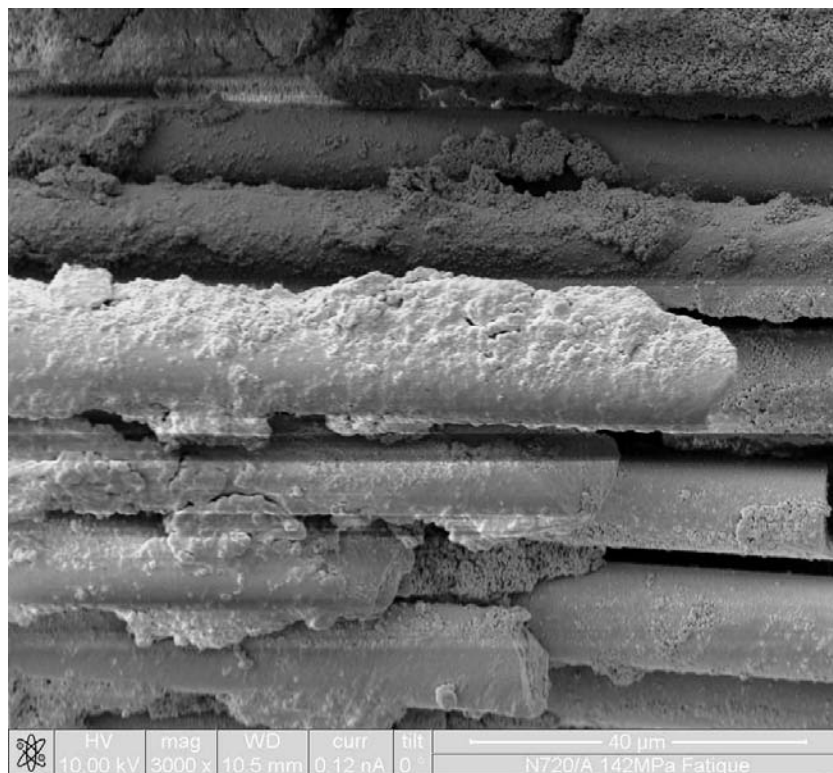


Figure 81. 142 MPa Side Fracture Back Fiber, 3000x

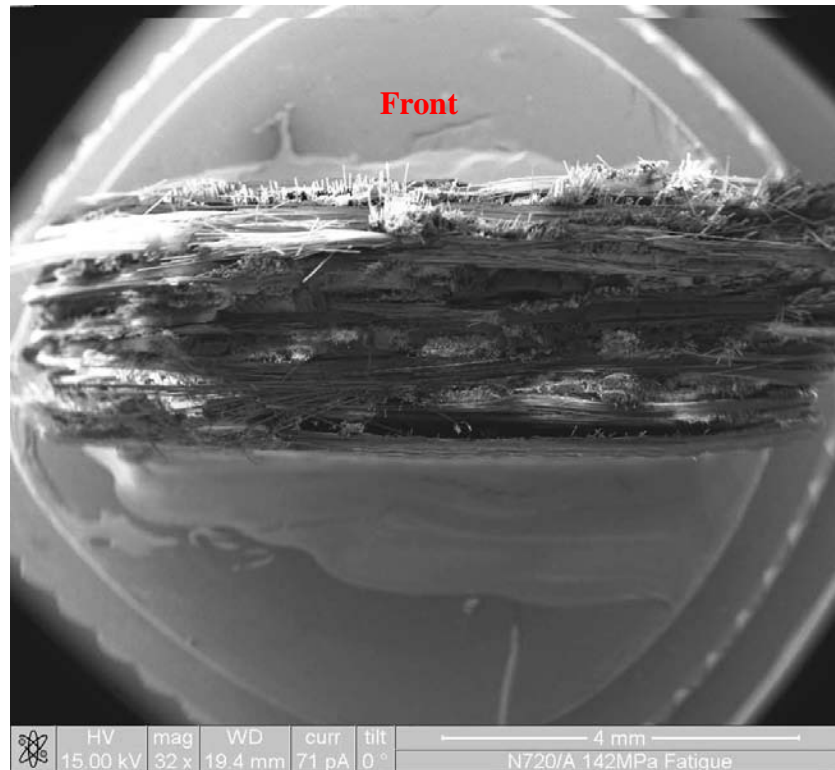


Figure 82. 142 MPa Fracture Surface, Overhead View, 32x

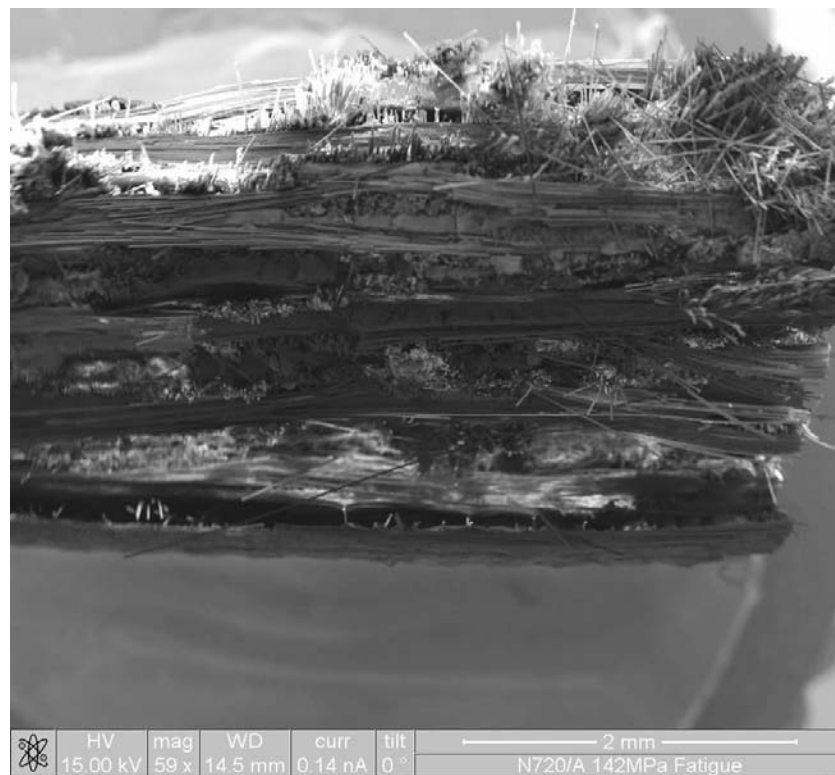


Figure 83. 142 MPa Fracture Surface, Overhead Right View, 59x

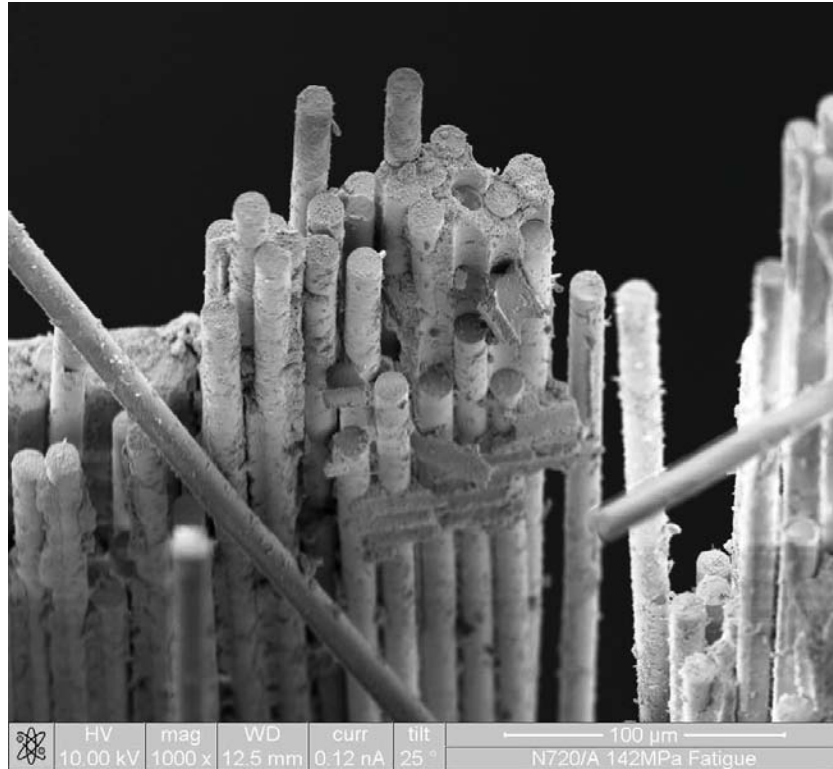


Figure 84. 142 MPa Fracture Surface, Front Right 90° Fiber Pullout, 1000x



Figure 85. 142 MPa Fracture Surface, Front Right Fiber-Matrix, 500x

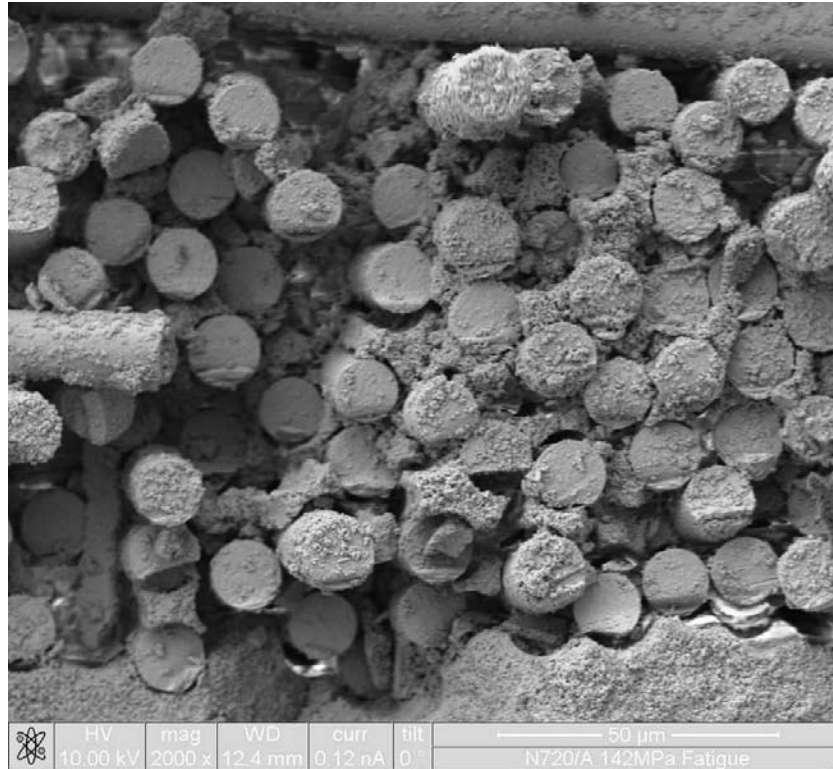


Figure 86. 142 MPa Fracture Surface, Front Right Fiber-Matrix, 2000x

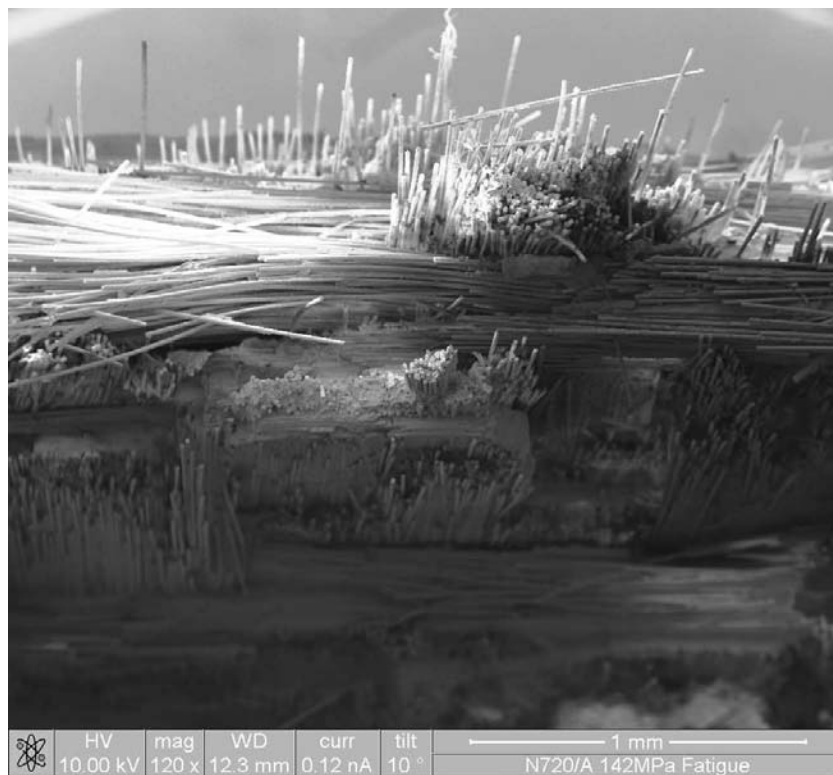


Figure 87. 142 MPa Fracture Surface, Front Center, 120x

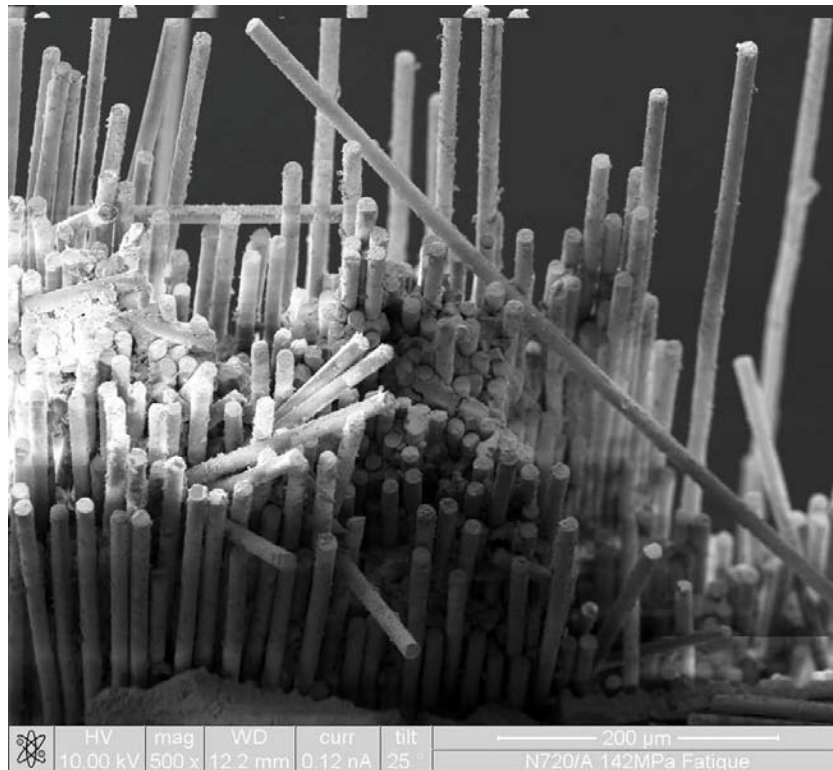


Figure 88. 142 MPa Fracture Surface, Front Center, 500x



Figure 89. 142 MPa Fracture Surface, Middle Center, 490x

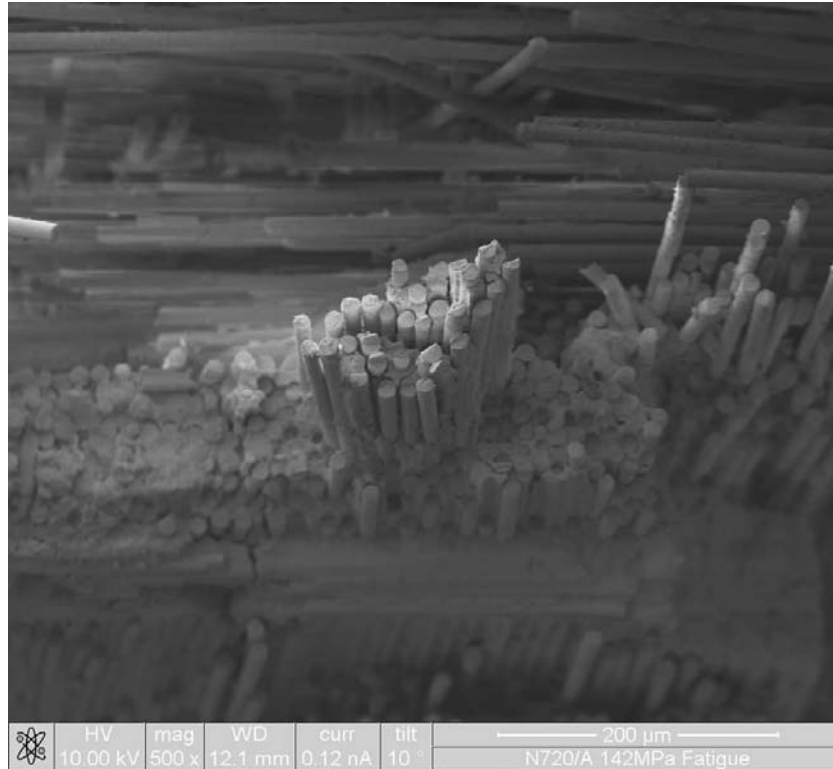


Figure 90. 142 MPa Fracture Surface, Middle Center Fiber Pullout, 500x

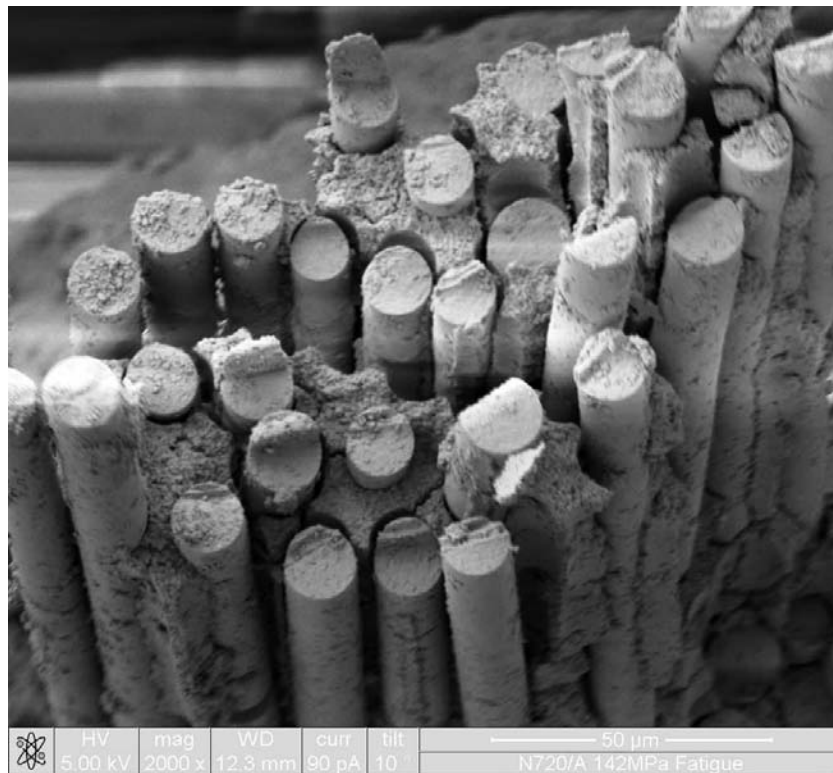


Figure 91. 142 MPa Fracture Surface, Middle Center Fiber Pullout, 2000x

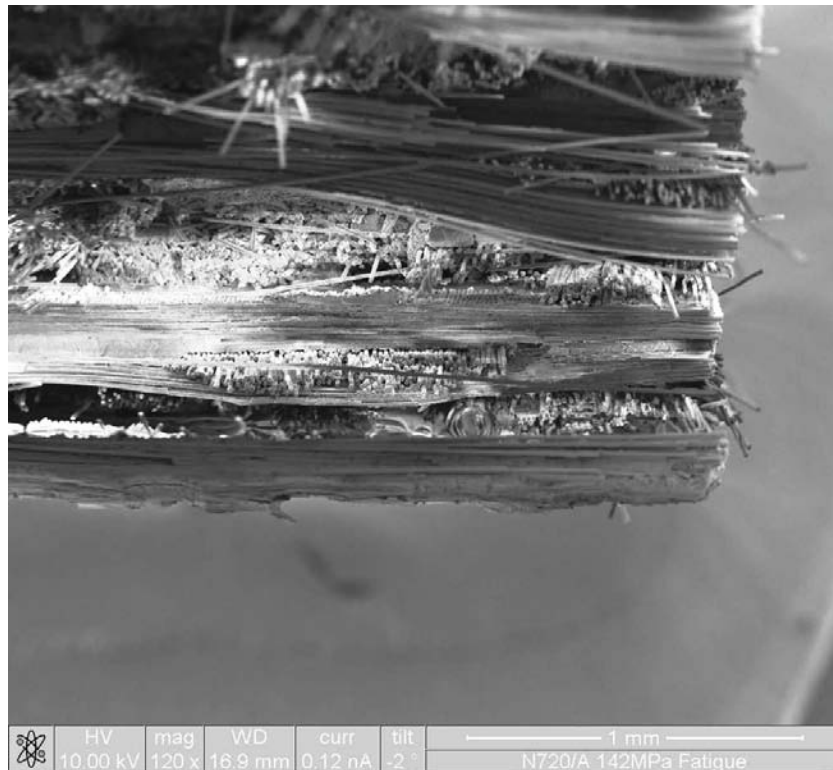


Figure 92. 142 MPa Fracture Surface, Rear Left, 120x

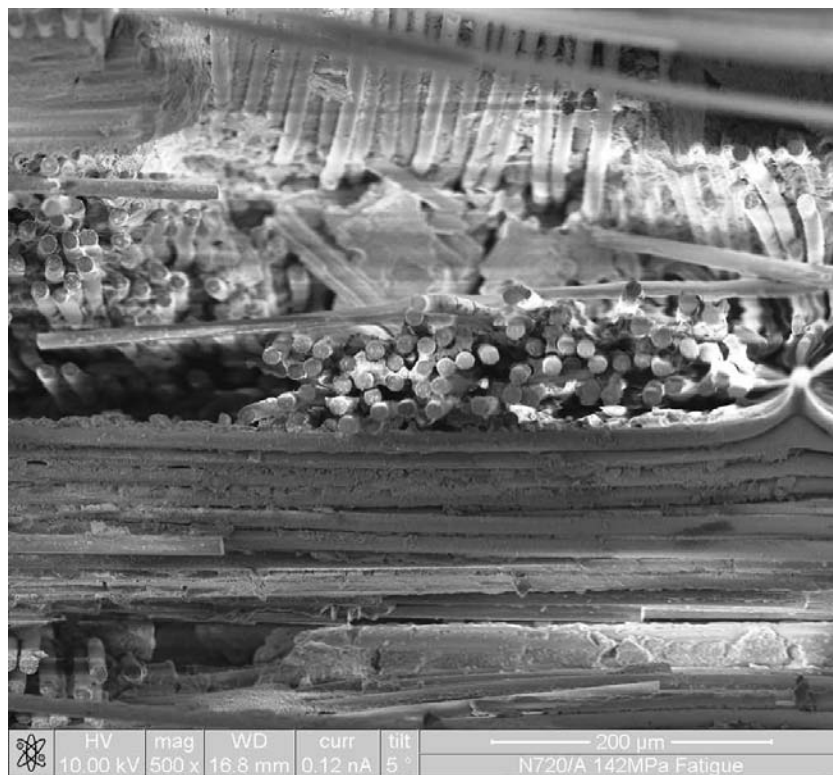


Figure 93. 142 MPa Fracture Surface, Rear Left Fiber Pullout, 500x



Figure 94. 142 MPa Fracture Surface, Rear Left Fiber Pullout, 1007x

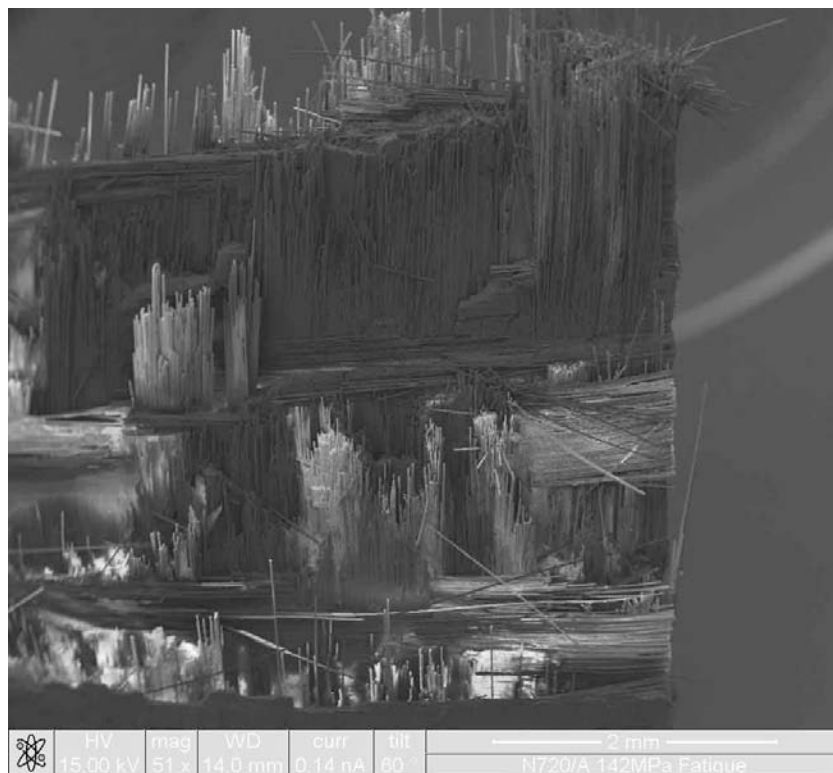


Figure 95. 142 MPa Fracture Surface, Rear Right Aft Looking Forward, 51x

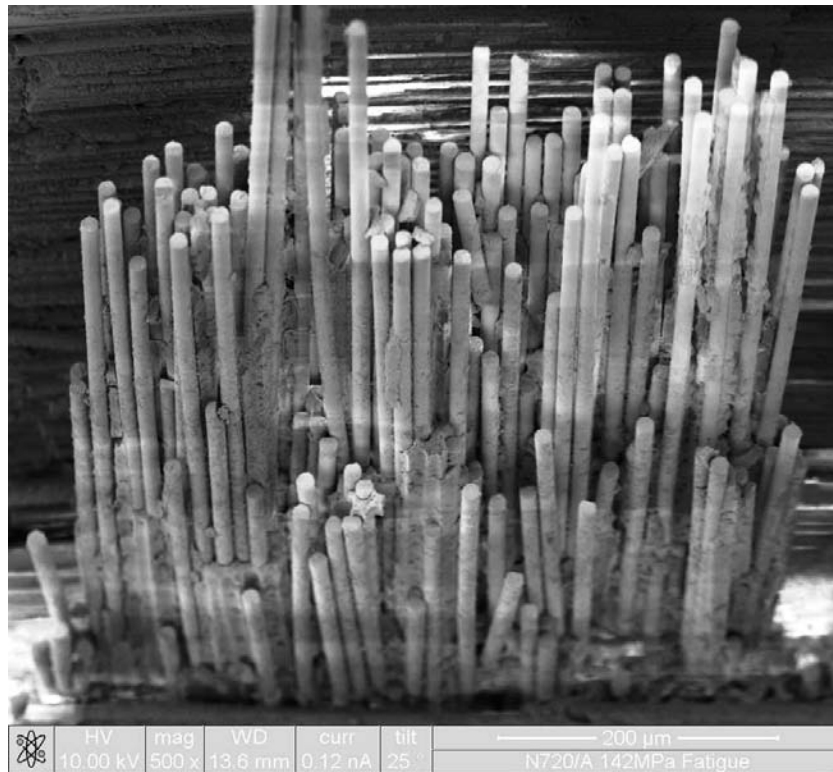


Figure 96. 142 MPa Fracture Surface, Middle Left Fiber Pullout, 500x



Figure 97. 142 MPa Fracture Surface, Rear Left Aft Looking Forward, 60x

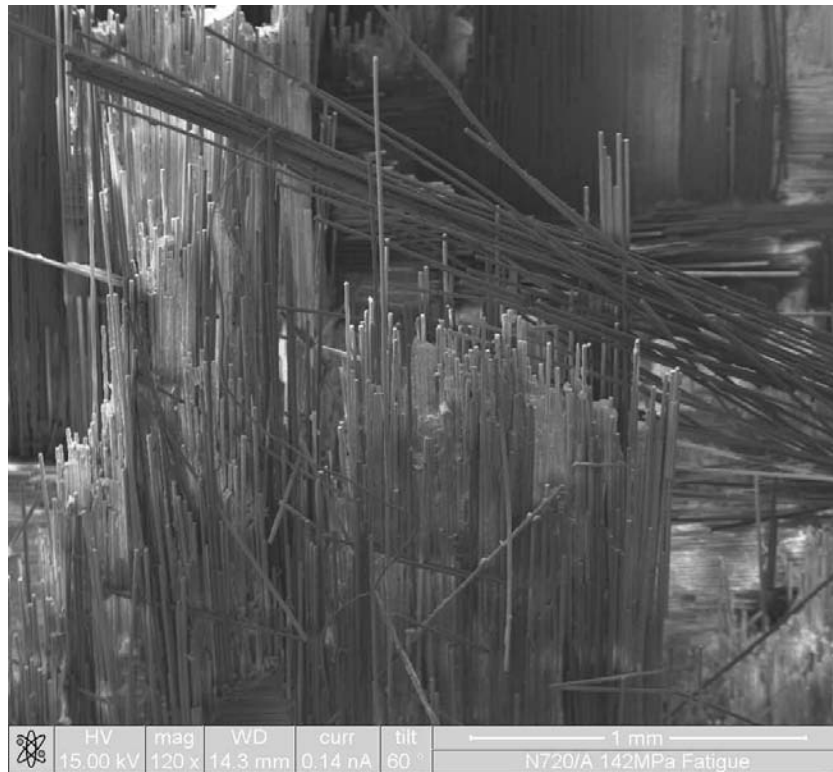


Figure 98. 142 MPa Fracture Surface, Rear Left Fiber Pullout, 120x

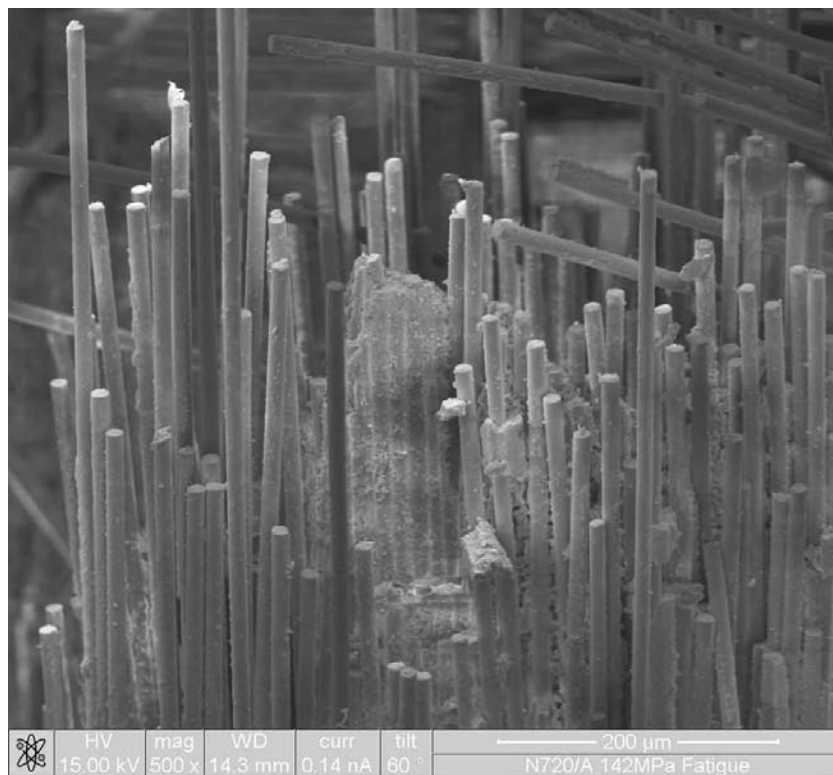


Figure 99. 142 MPa Fracture Surface, Rear Left Fiber Pullout, 500x

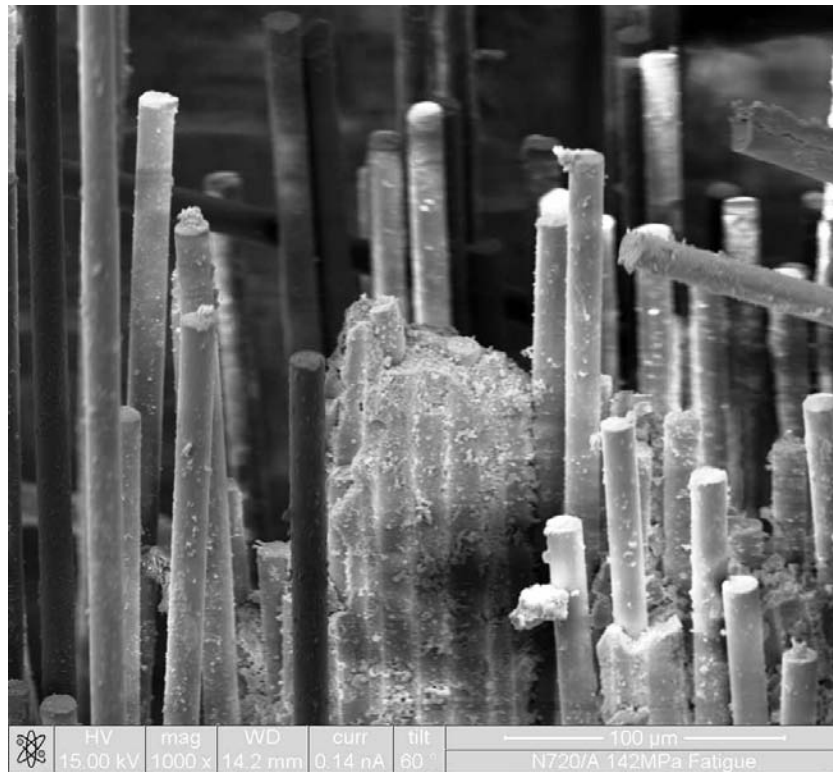


Figure 100. 142 MPa Fracture Surface, Rear Left Fiber Pullout, 1000x

Bibliography

1. *3M Nextel™ Ceramic Textiles*. Technical Notebook. St. Paul, MN: 3M Corporation, 2004.
2. Boyer, Barth H. *Creep-Rupture and Fatigue Behavior of a Notched Oxide/Oxide Ceramic Matrix Composite at Elevated Temperature*. MS Thesis, AFIT/GAE/ENY/08-J01. School of Engineering and Management, Air Force Institute of Technology (AU), Wright-Patterson AFB OH, June 2008.
3. Chawla, K.K. *Ceramic Matrix Composites* (2nd Edition). Boston: Kluwer Academic Publishers, 2003.
4. *Diamond Jet DJ HVOF Spray Gun*. Component Manual 56868, Issue b. Westbury, NY: Sulzer Metco (US) Inc, 2003.
5. Eber, Chalene A. *Effect of Temperature and Steam Environments of Fatigue Behavior of an Oxide-Oxide Continuous Fiber Ceramic Composite*. MS Thesis, AFIT/GA/ENY/05-M09. School of Engineering and Management, Air Force Institute of Technology (AU), Wright-Patterson AFB OH, March 2005.
6. "FLIR P640 Infrared Camera." Datasheet.
http://www.goinfrared.com/media/P640%20Datasheet_I102908PL.pdf. 4 March 2009.
7. Holst, Gerald C. *Common Sense Approach to Thermal Imaging*. Bellingham WA: SPIE Press, 2000.
8. Jurf, Robert A. and Steven C. Butner. "Advances in Oxide-Oxide CMC," *Journal of Engineering for Gas Turbines and Power*, 122: 202-205 (April 2000).
9. Kaplan, Herbert. *Practical Applications of Infrared Thermal Sensing and Imaging Equipment* (3rd Edition). Bellingham WA: SPIE Press, 2007.
10. Mattingly, Jack D. *Elements of Gas Turbine Propulsion*. Reston VA: American Institute of Aeronautics and Astronautics, Inc., 2005.
11. Mattingly, Jack D., William H. Heiser, and David T. Pratt. *Aircraft Engine Design* (2nd Edition). Reston VA: American Institute of Aeronautics and Astronautics, Inc., 2002.

12. Mattoni, Michael A., James Y. Yang, Carlos G. Levi, and Frank W. Zok. "Effects of Matrix Porosity on the Mechanical Properties of a Porous-Matrix, All-Oxide Ceramic Composite," *Journal of the American Ceramic Society*, 84: 2594-2602 (November 2001).
13. Mattoni, Michael A., James Y. Yang, Carlos G. Levi, Frank W. Zok, and Larry P. Zawada. "Effects of Combustor Rig Exposure on a Porous-Matrix Oxide Composite," *International Journal of Applied Ceramic Technology*, 2: 133-140 (March 2005).
14. National Aeronautics and Space Administration. *Radiative Property Measurements on Eight Samples of Varying Materials*. NASA Order Numbers C-77211-N and C-76771-N. Cleveland OH: NASA Glenn Research Center.
15. Parlier, Michel and M.H. Ritti. "State of the Art and Perspectives for Oxide/Oxide Composites," *Aerospace Science and Technology*, 7: 211-221 (April 2003).
16. Parthasarathy, Triplicane A., Larry P. Zawada, Reji John, Michael K. Cinibulk, and Joseph Zelina. "Evaluation of Oxide-Oxide Composites in a Novel Combustor Wall Application," *International Journal of Applied Ceramic Technology*, 2: 122-132 (March 2005).
17. "Properties of A-N720 CMC System." COI Ceramics, Inc. Oxide Ceramic Matrix Composites. <http://www.coiceramics.com/oxidepg.html>. 4 March 2009.
18. "Schematic cross-section of a typical HVOF spray gun." Image from website. n. pag. http://www.sulzermetco.com/en/desktopdefault.aspx/tabid-2008//3390_read-5302/. 4 March 2009
19. Steel, Steven G. *Monotonic and Fatigue Loading Behavior of an Oxide/Oxide Ceramic Matrix Composite*. MS Thesis, AFIT/GMS/ENY/00M-02. School of Engineering and Management, Air Force Institute of Technology (AU), Wright-Patterson AFB, OH, March 2000.
20. Sullivan, Mark A. *Creep-Rupture and Fatigue Behaviors of Notched Oxide/Oxide Ceramic Matrix Composite at Elevated Temperature*. MS Thesis, AFIT/GAE/ENY/06-M30. School of Engineering and Management, Air Force Institute of Technology (AU), Wright-Patterson AFB, OH, March 2006.
21. *ThermaCAM™ PM695 Operator's Manual*. Publ. No. 1 557 454, Revision B. Portland, OR: FLIR Systems AB, 2000.

22. Turns, Stephen R. *An Introduction to Combustion: Concepts and Applications* (2nd Edition). Boston: McGraw-Hill, 2000.
23. *Type DJF Diamond Jet Gas Flowmeter Unit*. Instructions G 41995, Issue b. Westbury, NY: Sulzer Metco (US) Inc, 1995.
24. Zok, Frank W. "Developments in Oxide Fiber Composites," *Journal of the American Ceramic Society*, 89: 3309-3324 (November 2006).

Vita

Captain Andrew R. Nye graduated from Sodus Central High School in Sodus, New York. He entered undergraduate studies at Clarkson University Potsdam, New York, where he graduated with a Bachelor of Science degree in Aeronautical Engineering in May 2004. He was commissioned through the Detachment 536 AFROTC at Clarkson University.

His first assignment was at Wright-Patterson AFB, Ohio; where he was a propulsion development engineer at the Aeronautical Systems Center. In August 2007, he entered the Graduate School of Engineering and Management at the Air Force Institute of Technology. Upon graduation, he will be assigned to the Air Force Research Laboratory, Materials Directorate at Wright-Patterson AFB, Ohio.

REPORT DOCUMENTATION PAGE			<i>Form Approved</i> <i>OMB No. 0704-0188</i>		
<small>The public reporting burden for this collection of information is estimated to average 1 hour per response, including the time for reviewing instructions, searching existing data sources, gathering and maintaining the data needed, and completing and reviewing the collection of information. Send comments regarding this burden estimate or any other aspect of this collection of information, including suggestions for reducing this burden to Department of Defense, Washington Headquarters Services, Directorate for Information Operations and Reports (0704-0188), 1215 Jefferson Davis Highway, Suite 1204, Arlington, VA 22202-4302. Respondents should be aware that notwithstanding any other provision of law, no person shall be subject to any penalty for failing to comply with a collection of information if it does not display a currently valid OMB control number. PLEASE DO NOT RETURN YOUR FORM TO THE ABOVE ADDRESS.</small>					
1. REPORT DATE (DD-MM-YYYY) 26-03-2009		2. REPORT TYPE Master's Thesis		3. DATES COVERED (From — To) September 2007 – March 2009	
4. TITLE AND SUBTITLE Ceramic Matrix Composite Characterization Under A Combustion And Loading Environment			5a. CONTRACT NUMBER		
			5b. GRANT NUMBER		
			5c. PROGRAM ELEMENT NUMBER		
6. AUTHOR(S) Andrew Nye, Capt, USAF			5d. PROJECT NUMBER		
			5e. TASK NUMBER		
			5f. WORK UNIT NUMBER		
7. PERFORMING ORGANIZATION NAME(S) AND ADDRESS(ES) Air Force Institute of Technology Graduate School of Engineering and Management (AFIT/ENY) 2950 Hobson Way WPAFB OH 45433-7765			8. PERFORMING ORGANIZATION REPORT NUMBER AFIT/GMS/ENY/09-M01		
9. SPONSORING / MONITORING AGENCY NAME(S) AND ADDRESS(ES) Intentionally Left Blank			10. SPONSOR/MONITOR'S ACRONYM(S)		
			11. SPONSOR/MONITOR'S REPORT NUMBER(S)		
12. DISTRIBUTION / AVAILABILITY STATEMENT APPROVED FOR PUBLIC RELEASE; DISTRIBUTION UNLIMITED					
13. SUPPLEMENTARY NOTES					
14. ABSTRACT <p>Lightweight materials that can withstand high temperatures and corrosive environments are constantly sought after in the aerospace industry, typically for Gas Turbine Engine (GTE) application. These materials need to retain their strength throughout the long service period they would see in the combustor and turbine components of a GTE. One material that is ideal for these types of applications is an oxide/oxide Ceramic Matrix Composite (CMC).</p> <p>The fatigue behavior of the oxide/oxide CMC Nextel™ 720/Alumina (N720/A) was investigated in a unique high temperature environment. N720/A consisted of an 8-harness satin weave of Nextel™ aluminum oxide/silicon oxide fibers bound together with an alumina matrix. Past studies have encompassed fatigue and creep-rupture resistant at elevated temperatures in laboratory air or other non-combustion environment, such as steam or inert gas. The specimens used in this research were exposed to a combustion environment, which is a much more volatile and realistic environment for what this material would see in a GTE application.</p> <p>The combustion environment was created using a High-Velocity Oxygen Fuel (HVOF) Gun. The flame directly impinged the CMC specimen on one side as it underwent fatigue testing, heating up that surface to approximately 1200°C. Results show that the effects of a combustion environment on the materials fatigue behavior are negligible.</p>					
15. SUBJECT TERMS ceramic composite, fatigue, temperature, combustion					
16. SECURITY CLASSIFICATION OF:			17. LIMITATION OF ABSTRACT	18. NUMBER OF PAGES	19a. NAME OF RESPONSIBLE PERSON
a. REPORT	b. ABSTRACT	c. THIS PAGE			Dr. Shankar Mall, ENY
U	U	U	UU	120	19b. TELEPHONE NUMBER (Include Area Code) (937) 255-6565, ext 4587 (Shankar.mall@afit.edu)